UMBC

DISSERTATION APPROVAL SHEET

Title of Dissertation: Systematic Effects of Compressive Sensing for Time-Series
Photometric Measurements for Space Observatories

Name of Candidate: Asmita A. Korde-Patel

Doctor of Philosophy,   2022

Graduate Program: ENEE

In Process

Dissertation and Abstract Approved:

Dr Tinoosh Mohsenin

Dr Tinoosh Mohsenin

Associate Professor

CSEE Department, Electrical Engineering

5/9/2022 | 10:51:26 AM EDT

Richard K. Barry

Richard K. Barry

Research Astronomer
Laboratory for Exoplanets and Stellar Astrophysics
NASA

5/11/22

NOTE: *The Approval Sheet with the original signature must accompany the thesis or dissertation. No terminal punctuation is to be used.

ASMITA KORDE-PATEL

CURRICULUM VITAE

EDUCATION

2013 MS Electrical Engineering, University of Maryland, Baltimore County

2011 BS Computer Engineering, University of Maryland, Baltimore County

PROFESSIONAL EXPERIENCE

NASA Goddard Space Flight Center, Electronics Engineer   Sept 2013 - Present

- Lead research projects as Principal Investigator
- Implemented hardware algorithms onto Field programmable gate arrays (FPGAs) for space flight instruments
- Developed and performed research on signal processing techniques and algorithms

SELECTED PUBLICATIONS

- Korde-Patel, Asmita, Richard K. Barry, and Tinoosh Mohsenin. "Application of compressive sensing for gravitational microlensing events." *Journal of Astronomical Telescopes, Instruments, and Systems* (2022). https://doi.org/10.1117/1.JATIS.8.1.018002

- Korde-Patel, Asmita, Richard K. Barry, and Tinoosh Mohsenin. "Compressive Sensing Based Data Acquisition Architecture for Transient Stellar Events in Crowded Star Fields." 2020 IEEE International Instrumentation and Measurement Technology Conference (2020).

- Korde-Patel, Asmita, Richard K. Barry, and Tinoosh Mohsenin.``Application of Compressive Sensing to Gravitational Microlensing Experiments." Proceedings of the International Astronomical Union (2016).

- Korde-Patel, Asmita, Richard K. Barry, and Tinoosh Mohsenin. ``Application of Compressive Sensing to Gravitational Microlensing Data and Implications for Miniaturized Space Observatories." Astronomical Data Analysis Software and Systems XXVI (2016).

- Mohammed, P. N., Korde-Patel, A., Gholian, A., Piepmeier, J. R., Schoenwald, A., & Bradley, D. (2017, July). An RFI detection algorithm for microwave radiometers using sparse component analysis. In *2017 IEEE International Geoscience and Remote Sensing Symposium (IGARSS)* (pp. 3452-3454). IEEE.

AWARDS

- NASA Performance Award (2012-2021)
- NASA Team Award: Exceptional Achievement for New Opportunities Captured (2015)
- NASA Group Achievement Award: STP-H4 SpaceCube Engineering Team (2013)

ABSTRACT

Title of Thesis: Systematic Effects of Compressive Sensing for Time-Series

Photometric Measurements for Space Observatories

Name of Candidate: Asmita Korde-Patel

Thesis directed by: Dr. Tinoosh Mohsenin
Department of Computer Science and
Electrical Engineering

- and -

Dr. Richard K. Barry
Laboratory for Exoplanets and
Stellar Astrophysics, NASA

Natural phenomena may be sparse in some physical or temporal domain. If we exploit this sparsity by applying the technique of Compressive Sensing (CS) to obtain information about a phenomenon, what are the specific implications for the science and for the sensing infrastructure?

In this thesis, we directly address this issue by an in-depth study of the generalized systematic effects consequent to the application of CS to time-series photometric measurements. We will assess implications for observability, sparsification, and information loss in the detection, retrieval and reconstruction process. CS is a simultaneous data acquisition and compression technique, which can significantly reduce data samples at the detector front-end itself.

To study time-series photometry, we explore the field of gravitational microlensing. A source star, typically in the galactic bulge, gets microlensed when there is a precise alignment of a lensing star and its planetary system with the source star. The

microlensed source star changes in flux magnification as the lensing system crosses the precise path of alignment, resulting in a microlensing curve in the time domain.

We develop a CS based architecture for acquiring and reconstructing transient astrophysical events. This architecture reconstructs a differenced image, eliminating the need for any sparse domain transforms otherwise required for traditional CS reconstruction. The resulting reconstructed differenced image is of importance as the information required for generating time-series photometric light curves is best obtained from an image differenced with a reference image.

To complete CS analysis for gravitational microlesning data, we simulate crowded stellar fields to obtain photometric light curves from the differenced images. We show through simulation modelling the error sensitivity for detecting microlensing event parameters. Our results conclude that for single and binary microlensing events we can obtain error less than 1% over a 3-pixel radius of the center of the microlensing star by using 25% Nyquist rate measurements. We show that CS accurately reconstructs gravitational microlensing curves within at least 10% statistical bounds of critical microlensing parameters. In addition, we show the effect of noise on such crowded stellar fields, where a star in the field is experiencing a microlensing event. We provide techniques to tune the CS measurement matrix in order to improve CS reconstruction in the presence of noise. We also study the effect of CS on gravitational microlensing parallax measurements for space-based observatories. Microlensing parallax breaks down degeneracy in the gravitational microlensing parameters, hence, providing additional information on the microlensing parameters of interest. Space observatory constellations provide an optimal platform for microlensing parallax measurements. The use of CS technology for small satellites (SmallSat) can be a game changing technology for obtaining valuable science parameters for gravitational microlensing.

Systematic Effects of Compressive Sensing for Time-Series Photometric Measurements for Space Observatories

by

Asmita Korde-Patel

PhD Dissertation, 2022

ACKNOWLEDGMENTS

I would like to thank my advisors Dr. Tinoosh Mohsenin and Dr. Richard K. Barry for their support and guidance throughout my thesis research. I would like to thank Dr. Damon Bradley for introducing me to the field of Compressive Sensing and his support throughout my PhD career. In addition, I would like to thank my NASA branch for their support, in helping me gain research proposals, to continue my PhD research. Finally, I would like to thank my family- my parents, my husband, and daughter, for their continuous support and encouragement.

TABLE OF CONTENTS

LIST OF TABLES

LIST OF FIGURES

xvi

List of Abbreviations

CS	Compressive Sensing
SmallSat	Small Satellite
FOV	Field-of-view
ASTERIA	Arcsecond Space Telescope Enabling Research in Astrophysics
FPGA	Field Progammable Gate Array
DMD	Digital Micro-mirror Device
ADC	Analog-to-Digital Converter
SNR	Signal-to-Noise Ratio

Chapter 1

INTRODUCTION

1.1 Motivation and Problem Statement

1.1.1 Motivation

Remote sensing applications characteristically suffer limitations on the availability of electrical power, data communications bandwidth and processing power. There is at present a significant, sustained trend towards miniaturization of the bus infrastructure that supports many sensing applications - a trend which quite exacerbates these limitations. For example, there is currently a renaissance in the approach to the design and implementation of space-borne observatories to reduce their size and complexity. Indeed, NASA has constructed a new categorization for such observatories; from minisatellites, ranging in mass from 100-180 kilograms, down to femtosatellites as small as 0.001 kilograms - about the mass of a paperclip.

Contemporaneously with these significant bus infrastructure design trends the miniaturization of individual detectors is permitting the manufacture of large, dense detector arrays capable of making measurements requiring enormous data storage, processing and transmission capabilities. We may confidently expect that the confluence of these trends will reach a self-limiting point - the precise bottleneck being, again, availability of electrical power, data communications bandwidth and processing

power.

In light of these conflicting trends, exploitation of sparsity in the observed phenomena presents an obvious opportunity. Reduction in the power and communications bandwidth may be effectuated by the use of post-detection compression - at the expense of increased on-board processing power. The use of Compressive Sensing (CS) technology - reduction of data bandwidth at the point of detection - holds the promise of reducing all three. As with post-detection compression, loss of information will certainly occur and will increase in inverse proportion to data bandwidth and power savings.

Theoretical aspects of post-detection compression have been well-studied in the literature and exhaustively exploited by technologists. In contrast, CS, a relatively new technique, is only now beginning to be explored for detection and measurement of many phenomena. As with post-detection compression, the critical aspect of the technique - its effect on the measurement - must be carefully assessed. Crucially, no comprehensive study of the systematic effects of CS has been conducted to date on this promising and potentially enabling technology.

1.1.2 Statement of Problem and Proposed Research

Natural phenomena may be sparse in some physical or temporal domain. If we exploit this sparsity by applying the technique of Compressive Sensing to obtain information about a phenomenon, how do our measurements change as a function of domain and generalized measurement systematics? What are the specific implications for the science and for the remote sensing bus infrastructure?

With this thesis we propose to directly address this issue through application of CS to remotely sensed time-ordered photometric measurements. Specifically, this thesis will examine the application of CS in the study of the photometric transient

phenomenology associated with gravitational microlensing in the presence of measurement systematics. This thesis will assess implications for observability, sparsification, and information loss in the detection and retrieval processes. These results will be of general applicability to measurement using CS.

1.2   Contributions

This thesis will make the following specific contributions: 1. Develop a CS framework for application of transient photometric measurements. We specifically studied photometric measurements due to gravitational microlensing events. 2. Analyze the impact of CS on the retrieval of gravitational microlensing parameters 3. Perform a study and analysis on CS reconstruction for measuring microlensing parallax from space observatories 4. Analyze the impact of background noise, as well as detector measurement noise on CS reconstruction 5. Developed a framework for a spaceflight constellation architecture for measuring gravitational microlenisng parallax.

The next few sections discuss each contribution in detail.

1.2.1   CS Framework for Transient Photometry

We develop a CS framework as applicable for transient photometry. We show that this architecture implementation increases sparsity of the data set, as required for accurate CS reconstruction. This architecture eliminates the need to transform the data into a sparse domain, thereby significantly reducing computational complexity.

1.2.2   CS Application for Gravitational Microlensing

We show the effect of CS on transient photometric measurements, specifically obtained due to gravitational microlensing events. Our work shows the effectiveness

of CS as a function of magnification factors for microlensing events. Furthermore, we perform an in-depth analysis on the retrieval of gravitational microlensing parameters due to the impact of CS data acquisition and reconstruction for both single and binary lensed events.

1.2.3 CS Analysis for Measuring Gravitational Microlensing Parallax

In order to obtain lens mass in a gravitational microlenisng event, microlensing parallax measurements are critical. We provide a simulation model for obtaining space-based microlensing parallax using CS techniques. We show the effectiveness and the need for implementing CS for space-based SmallSat observatories.

1.2.4 Impact of Noise on CS Reconstruction

We show the impact of noise on CS reconstruction of transient photometric curves. In addition, we provide techniques to tune the CS measurement matrix in order to provide higher accuracy for CS reconstruction in the presence of noise.

1.2.5 CS Detector for a Space-Based Satellite Constellation

Lastly, we show an architecture for space-based satellite constellation for obtaining microlensing parallax using CS detectors. We also show the data volume resource usage comparison for CS-based detectors versus traditional detectors.

1.3 Literature Review

Compressive sensing applied to astronomical observation is a new field. Bobin et al. discuss application of CS to astronomical images in (Bobin, Starck, & Ottensamer 2008). In their work, CS is discussed as a way of sensor design as well a

compression scheme. We will be implementing CS as part of the sensor design in architecture I and II, while as a compression scheme in architecture III. They apply CS to simulated Hershel data, and show that CS has great potential for its application to the Hershel space mission. Their conclusions help foster the effectiveness of using CS on astronomical data sets. In our research, we extend this aspect of preserving accuracy in spatial reconstructed images to preserving accuracy in time-domain photometric data, specifically microlensing events, while sampling in the spatial domain. CS has also been studied in the context of weak gravitational lensing by Leonard et al. (Leonard, Dupé, & Starck 2012). Their results show that CS works better than the currently used linear methods to accurately reproduce clusters.

The advancement of CS technology has been very prominent in the past few years. From the theoretical implications discussed in (Eldar & Kutyniok 2012) and (Candès & Wakin 2008) to recent advances in practical applications. In this research, we mainly focus on CS theory as applicable to astronomical data sets. We explore reconstruction algorithms, measurement matrix, and sparsity. For reconstruction algorithms, we use the latest developments in convex optimization theory (O Donoghue *et al.* 2016) as well as their corresponding Python packages (Diamond & Boyd 2016) as provided by Boyd and group. Our research will consist of finding the optimal algorithms for microlensing application. For better CS reconstruction, sparsity in data sets is necessary. Starck applies various transforms for sparsifying astronomical images (Starck, Murtagh, & Fadili 2010a). In our future work, we will experiment with some of these transforms. However, as dictionary learning has become a new and emerging field of sparsiying data as relevant to our specific training sets, we first explore its effectiveness for our application. Beckouche et al. have studied dictionary learning, but instead for denoising astronomical images (Beckouche, Starck, & Fadili 2013). Duarte-Carvajalino et al. studied optimal methods to obtain a sens-

ing (or measurement) matrix while simultaneously finding a sparse basis dictionary (Duarte-Carvajalino & Sapiro 2009). As we further our research on obtaining good measurement matrices, we will build on their work. Currently, we have separately analyzed random measurement matrices and use of dictionary learning for obtaining a sparse transform domain for use in CS applications.

To our knowledge, there is no published research on the application of CS techniques to detect and analyze astronomical time-domain transient events such as the ones caused by microlensing. This can be generalized to the detection of all time-domain phenomena and would be a novel approach for the science community and an enabling technology for the entire class of microsatellites.

1.4 Organization of Thesis

This thesis combines gravitational microlensing and compressive sensing into one architecture. In Chapter 2, we discuss CS theory and CS related parameters. This is followed by Chapter 3, in which gravitational microlensing related parameters are discussed. In Chapter 4, we provide a CS based architecture for reconstructing transient photometric measurements. In Chapter 5, we perform a detailed analysis on the implication of CS on gravitational microlensing parameters. We follow that with Chapter 6, where we analyze the implications of microlensing parallax observations using CS techniques. In Chapter 7, we analyze effects of noise on CS reconstruction for transient photometric curves. In Chapter 8, we put together a CS detector architecture for implementing a space observatory, in order to detect gravitational microlensing parallax. Finally in Chapter 9, we provide conclusions and our path forward for this research.

COMPRESSIVE SENSING PARAMETERS

Compressive sensing is a mathematical theory for sampling at a rate much lower than the Nyquist rate, and yet, reconstructing the signal back with little or no loss of information. The signal is reconstructed by solving an underdetermined system. This works only when the signal we are solving for is sparse in the domain we are reconstructing. Hence, if it is not sparse in the sampling domain, we can transform it to a sparse domain, perform the reconstruction and then transform it back to the original domain. This theory is applied to gravitational microlensing datasets to extract relevant information about a microlensing event. In this chapter, we begin by providing some background on Compressive Sensing and then discuss gravitational microlenisng application. Then, we incorporate them together to provide architectures for implementation.

2.1   CS Theory

The signal of interest, x, is a sparse signal of length N. Here, Φ_{MxN} is the measurement matrix, which is projected onto x to obtain the y_{Mx1} measurements, where $M << N$, as shown in Figure 2.1. The goal is to solve for x in equation 2.1.

$$y = \Phi x \hspace{4cm} (2.1)$$
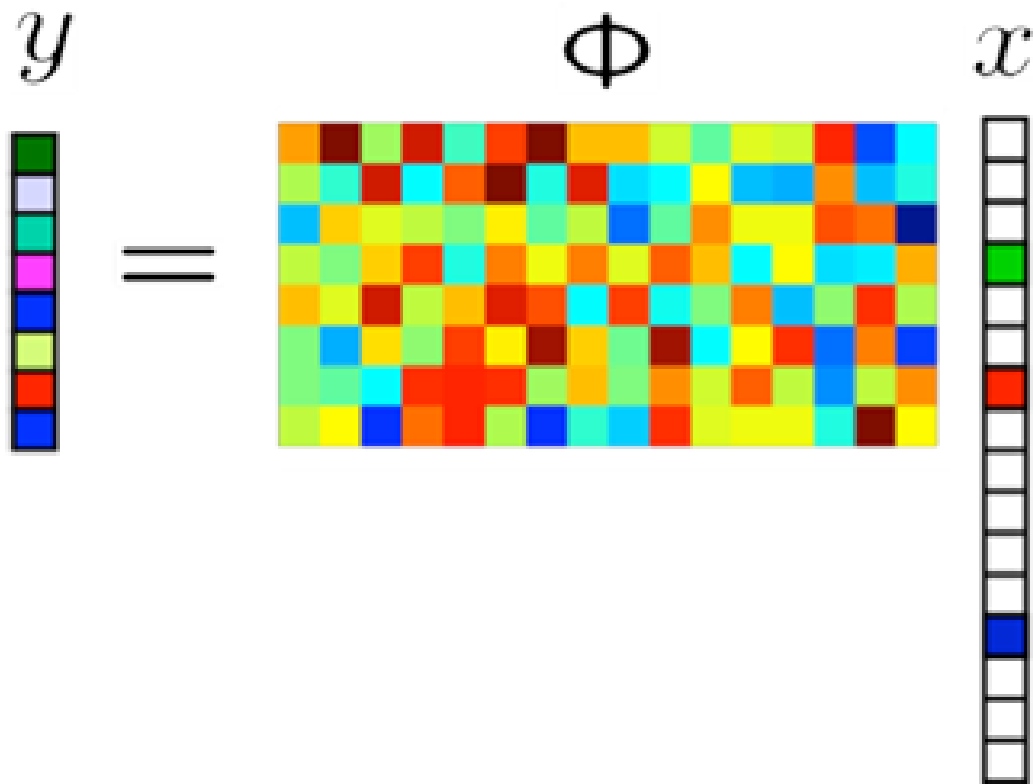
FIG. 2.1: CS Architecture I

If x is not sparse in the sampling domain, then a transform basis, Ψ_{NxN}, can be applied to obtain sparsity. CS requires the signal to be sparse in order for the reconstruction algorithms to reconstruct the signal accurately. This is further described in Chapter 3. A sparse transformed domain signal, s, can be reconstructed during CS reconstruction process and then transformed back to the sampling domain to obtain x. In this section, we describe two ways of implementing sparse domain

transformation as applicable to CS. The first method uses a dictionary basis and an encoded signal to represent the signal, x.

$$y = \Phi\Psi s \tag{2.2}$$

If sampling occurs in the spatial domain, then in this case, Φ is projected onto the spatial image, x, and s is reconstructed, given y, using $\Phi\Psi$. Once s is obtained it can easily be transformed back to the domain of x using $x = \Psi s$

Similarly, if $x = \Psi s$, we can obtain a D such that $Dx = s$. Here, Ψ is the inverse of D. The second method uses that form, to solve the problem show in equation 2.4.

$$y = \Phi D x \tag{2.3}$$
$$= \Phi s \tag{2.4}$$

Here, ΦD is projected onto x to obtain y, and only Φ is used to reconstruct s, which is then transformed back to the domain of x. The second method is briefly discussed in (Candes *et al.* 2011) as part of a discussion on coherence of dictionaries. In their paper, their goal is to reconstruct the sparse signal, s itself rather than the transformed signal.

In this chapter we discuss some of the important parameters required for compressive sensing as applicable to time-domain photometry, specifically, gravitational microlensing. We discuss sparsity, number of measurements, measurement matrix, and reconstruction algorithms.

9

2.2 Sparsity

Compressive sensing exploits sparsity in signal, so that a signal can be recovered using fewer number of measurements, as compared to sampling the total number of pixels in the image. If a signal is sparse, then it can be well approximated by a linear combination of only a few elements of a given basis. A typical sky field can be densely populated especially if we are analyzing microlensing events in the galactic bulge. We will apply a few common transforms such as Fourier and wavelet to analyze the sparsification due to the transforms. Starck discusses other transforms relevant to astronomical images in (Starck, Murtagh, & Fadili 2010a). Rebello-Neira uses redundant discrete B-Spline based dictionaries for astronomical images (Rebollo-Neira & Bowley 2013). In this proposal research, we apply dictionary learning to find a sparse basis given a training data set. A signal, x is k sparse if:

$$x : ||x||_0 <= k \qquad (2.5)$$

As real-world signals are not exactly sparse, compressible signals can be approximated as relatively sparse. A compressible signal has coefficients which decay at a high rate (Eldar & Kutyniok 2012). We study a HST data set image, $iabf01bxq_raw.fits$ (Figure 2.2), to determine the compressibility of the coefficients of that image.
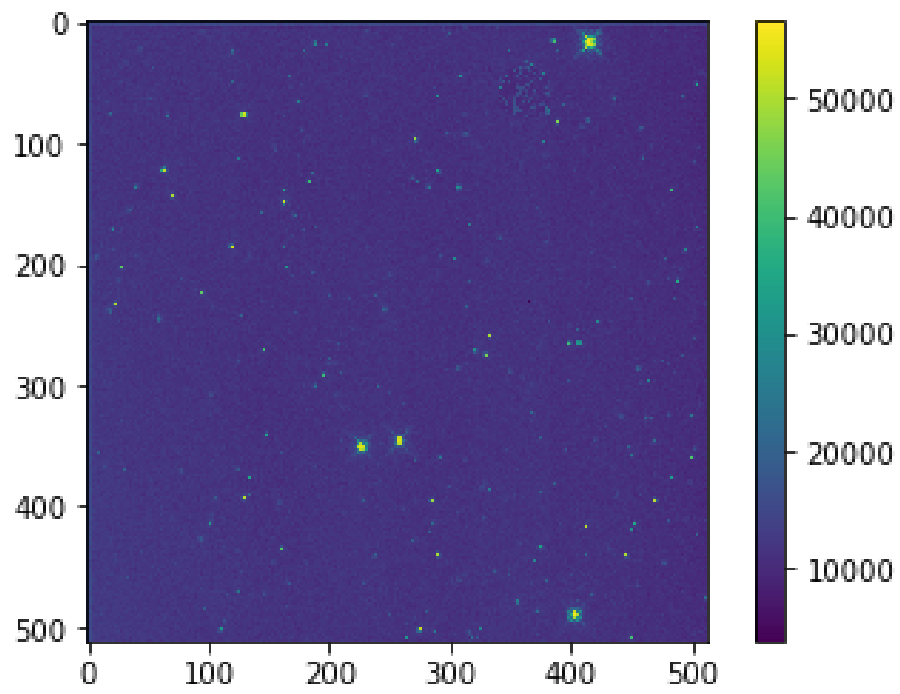
FIG. 2.2: HST Image
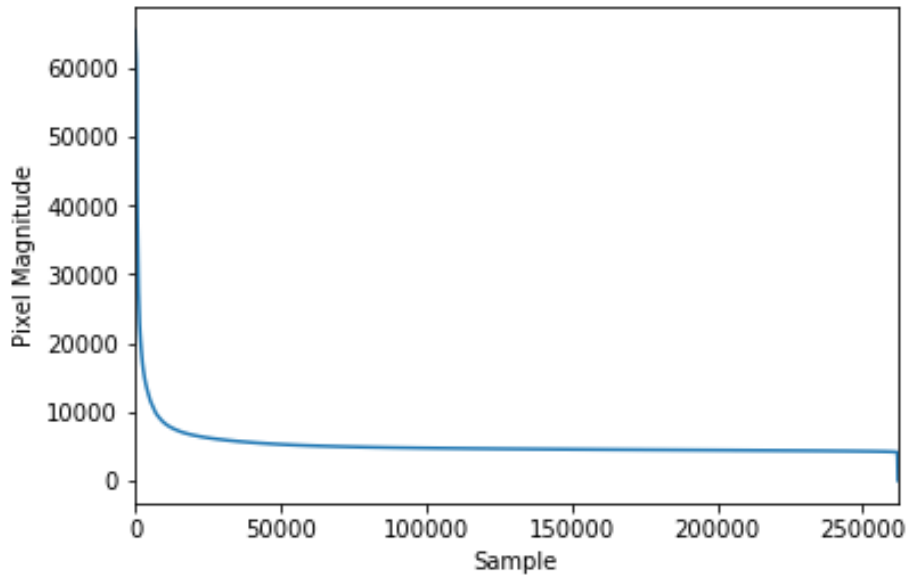
FIG. 2.3: Sorted coefficients

To reach from the maximum to the minimum pixel value, the rate of decay is not very high as it stays constant before dropping off to near 0.

To emphasize the need for sparsity in CS applications, we apply CS using 50% of N measurements to Figure 2.2 and reconstruct it. Here N is the total number of pixels in the image. Figure 2.4 is the reconstructed image using CS techniques without applying any sparsifying basis.
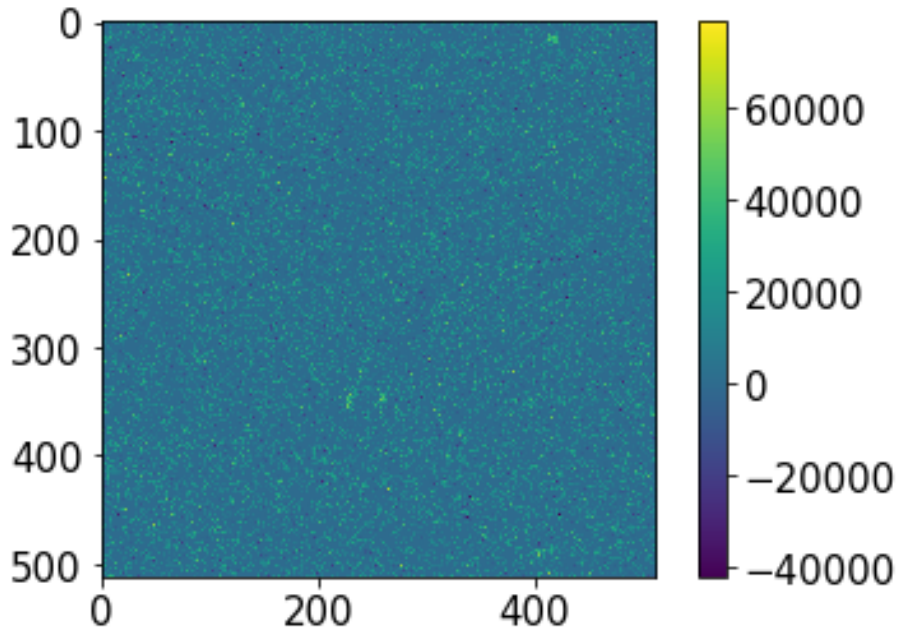
FIG. 2.4: CS Reconstructed image without sparse domain transformation

As seen from Figure 2.4, the germane information from Figure 2.2 is not preserved in figure 2.4. The PSNR of this image is 14.24 dB. In the next experiment, a specific dictionary is generated for each column of the image and CS is applied individually to each column. This will be used as a method of sparsifying data in Figure 2.2. The complete image is stitched together after all the columns of the image are reconstructed.

Dictionary Learning In our simulation, we use Online Dictionary learning as described in (Mairal *et al.* 2009). A python package, (Pedregosa *et al.* 2011), which uses that algorithm is used for our simulations. Online dictionary learning algorithm finds a sparse representation of our image, iteratively. For each column of Figure 2.2, a dictionary and an encoded signal is obtained using Equation 2.6.

$$(s, \Psi) = \min_{s, \Psi} 0.5||x_i - s\psi||_2^2 + ||s||_1 \qquad (2.6)$$

For computational purposes, we assume a 1D signal by slicing the image into n vectors, where each column of Figure 2.2, x_i, represents a vector. Once a dictionary and code is obtained, a sparse representation is shown as in 2.7.

$$x = s\Psi \qquad (2.7)$$

Here x_i, where $i = 1 : n$, is n x 1 image vector, s_{nxp} is the code and Ψ_{px1} is the dictionary.

In order for CS to reconstruct the sparse signal, s, the sensing matrix must be multiplied with Ψ during the reconstruction process. The steps for the rearranging matrix while preserving the matrix properties are shown below.

$$x^T = (s\Psi)^T \qquad (2.8)$$

$$= \Psi^T s^T \qquad (2.9)$$

Figures 2.5 show a sample dictionary and encoded signal for an image vector from Figure 2.2.
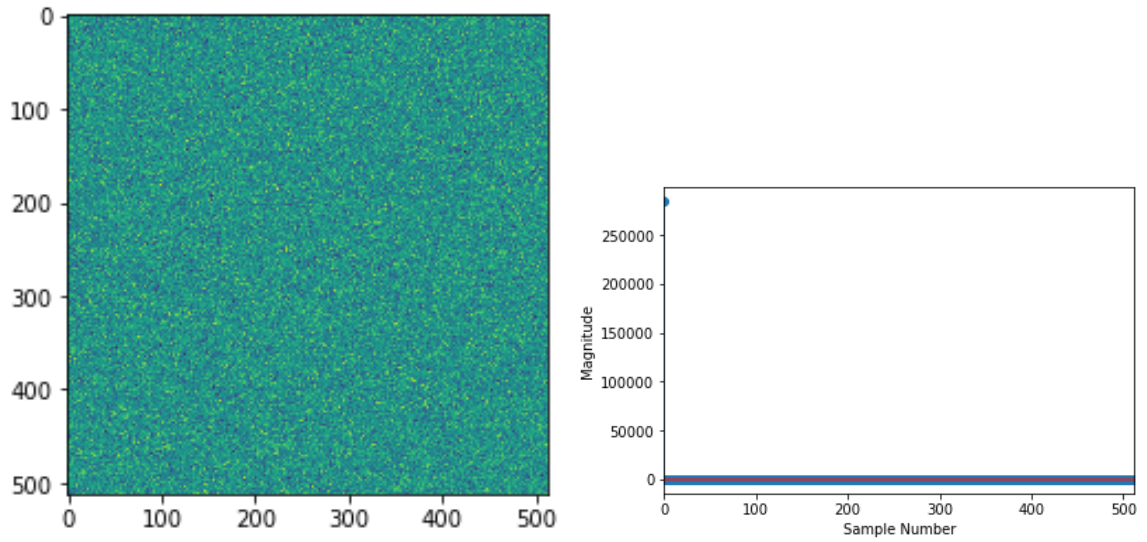
(a) Sample Dictionary, Ψ

(b) Sample sparse coded signal, s
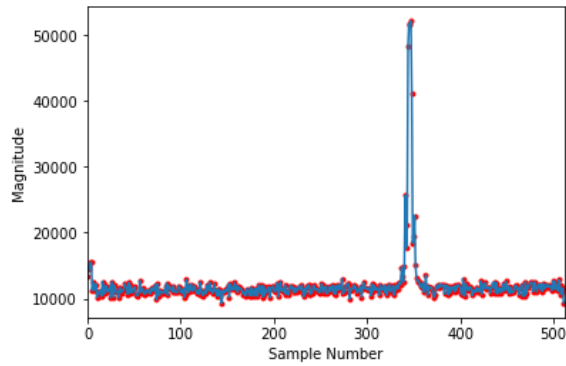
(c) Comparison between original signal, x^T and encoded signal $(\Psi^T s^T)$

FIG. 2.5: Ψ, s, and encoded signal (red dotted line) compared with original signal (blue continuous line)

If each column is provided with its optimal dictionary, a nearly perfect image can be reconstructed even with only 50% of Nyquist rate measurements as seen from Figure 2.6. Figure 2.6 has a PSNR of 90.2 dB.
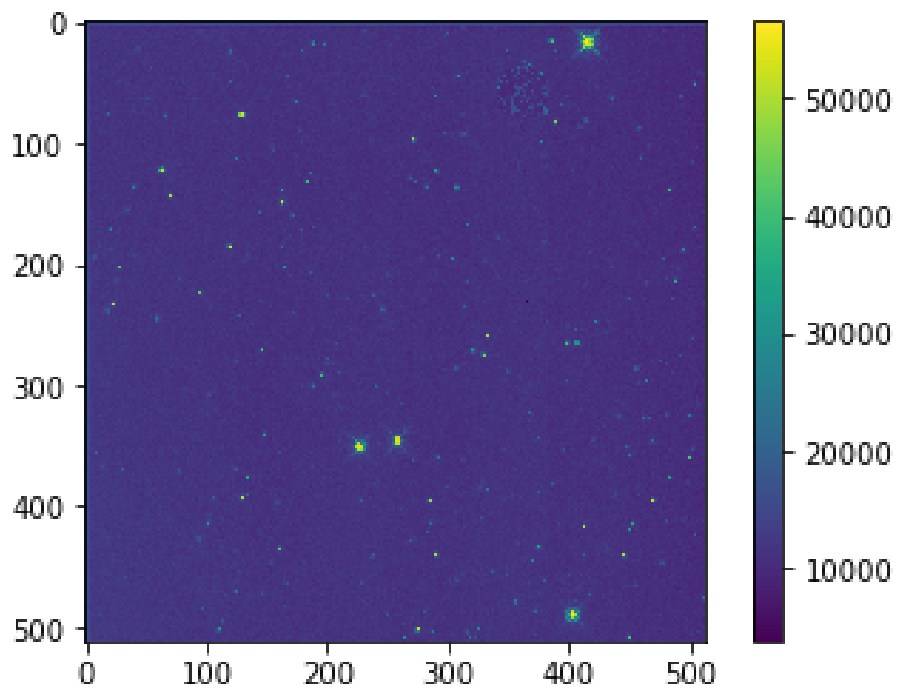
FIG. 2.6: CS Reconstructed Image
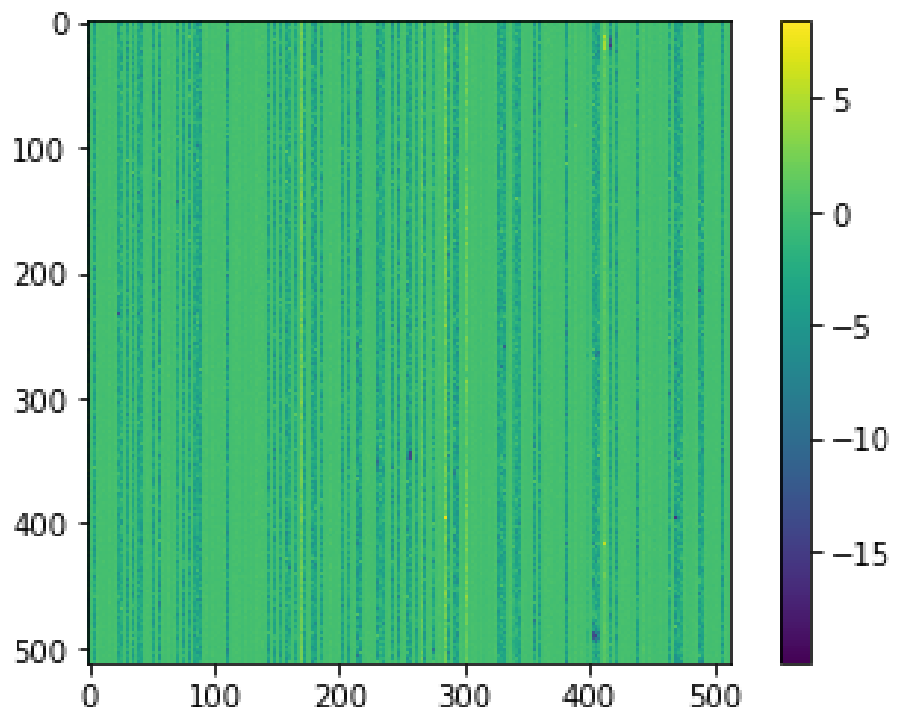
FIG. 2.7: Difference between reconstructed and original image

16

Finding a dictionary specific to each image column may be impractical in a real-world application as the signal itself is unknown. In order to obtain a good dictionary suitable for a wide range of data sets, a good training data set needs to be generated. However, as the sky portion, specifically the galactic bulge, which is usually observed for microlensing events, has been imaged by several missions, finding a good dictionary for each portion of that region of the sky is feasible. There has been a lot of literature on finding sparse matrices using dictionary learning. Recent advances provide methods of simultaneously acquiring a dictionary and sensing matrix (Duarte-Carvajalino & Sapiro 2009). These methods will be further studied to apply them to our astronomical images and to analyze their impact in the time domain. An important criteria is to reconstruct an image to the accuracy such that the pixels containing the flux of the star source is preserved in the time domain to differentiate the amount of change in flux over two consecutive time sampled spatial images. This extended research will be studied in our future work in order to complete the thesis. In previous work related to astronomical images, dictionary learning was used as a method of denoising images (Beckouche, Starck, & Fadili 2013). In this preliminary work, we showed that dictionary learning is a feasible option for sparsifying astronomical images and we have incorporated it into the CS framework.

2.3 Measurement Matrix

Measurement matrix or sensing matrix is the matrix projected onto the signal of interest to acquire the less than Nyquist rate measurement samples. The projection onto the signal, x, is $A = \Phi D$ from equation 2.4. This is the sensing matrix multiplied by the transform basis. From here on, in this thesis, we will refer to A as the measurement matrix, and Φ as the sensing matrix. However, in other literature, the

projection matrix, with or without multiplication with a transform basis is referred to as the sensing matrix.

2.4 Measurement Matrix Theory

For simplicity, in this section, we assume D, the transform basis, to be the identity matrix. We will consider Equation 2.1:

$y = \Phi x$

For CS to reconstruct accurately while being robust to noise as well, the restricted isometric property (RIP) is given:

$$(1 - \delta_k)||x||_2^2 \leq ||Ax|| \leq (1 + \delta_k)||x||_2^2 \tag{2.10}$$

for $\delta_k \in (0, 1)$

This property states that the distance is preserved between any pairs of such x vectors (Eldar & Kutyniok 2012). Further theoretical derivations are also provided in (Pope 2009). For matrix A satisfying this property, it is sufficient for stable recovery of x using various l_1 norm minimization algorithms. However, the RIP property is not easy to compute as it is NP hard. Gaussian and Bernoulli matrices are known to satisfy k-order RIP (Nguyen & Shin 2013) and hence, are good measurement matrices for CS. As RIP is not easily computable, other properties such as incoherence of the measurement matrix can be computed to provide recovery guarantees. This is further analyzed in the next section.

The number of measurements required is related to the sparsity of the signal as well as the length of the signal. In addition, the measurement matrix has to satisfy the RIP of order $2k$ to achieve the measurements bound. Theoretically,

18

$$M \geq Ck \log \frac{n}{k} \tag{2.11}$$

where $C = \dfrac{1}{2 \log(\sqrt{24} + 1)} \approx 0.28$ (Eldar & Kutyniok 2012).

2.4.1   Measurement Matrix Analysis

The measurement matrix is the matrix projected onto to the original signal. This matrix needs to be incoherent with the basis of the original signal. In general, random matrices are universally incoherent. We studied Bernoulli and Gaussian random matrices to understand their incoherence as a function of the number of rows and columns in a matrix. We assume D to be the identity matrix and Φ to be either a Bernoulli or Gaussian random matrix. In order to obtain accurate recovery for compressive sensing reconstruction, various bounds must be met. The bounds relate to the mutual coherence of the measurement matrix (Eldar & Kutyniok 2012).

$$spark(A) \geq 1 + \frac{1}{\mu(A)} \tag{2.12}$$

$$k < \frac{1}{2} spark(A) \tag{2.13}$$

where A is an M x N matrix and $\mu(A)$ is the coherence of A. If this bound is satisfied, we can get a guaranteed k-sparse solution using L_1 minimization techniques. Work from (Elad 2007) shows that the lower the incoherence of the measurement matrix, the better results CS is able to acquire. Sparsity and mutual coherence theoretical implications are also discussed in (Candes & Romberg 2007)
In this thesis, we analyze the behavior of $\mu(A)$ for varying sizes of A.

Results and Analysis We measure coherence of matrix A for M x N sizes with ratio of 1:3 for Gaussian random matrix and Bernoulli random matrix. Here we take

$$A = \frac{A'}{\sqrt{M}} \tag{2.14}$$

A' is a randomly generated independent and identically distributed (i.i.d) Bernoulli or Gaussian matrix. We compute the coherence:

$$\mu(A) = \max_{0 \leq i \neq j \leq N} \frac{|<a_i, a_j>|}{\|\|a_i\|_2 \|\|a_j\|_2} \tag{2.15}$$

Bernoulli Random Matrix We analyze the coherence and behavior of the Bernoulli Random matrix of size $200x600$. Fig. 2.8 shows the average coherence over 50 iterations for matrix size varying from 1x3 to 200x600 by a factor of 1 to 3.
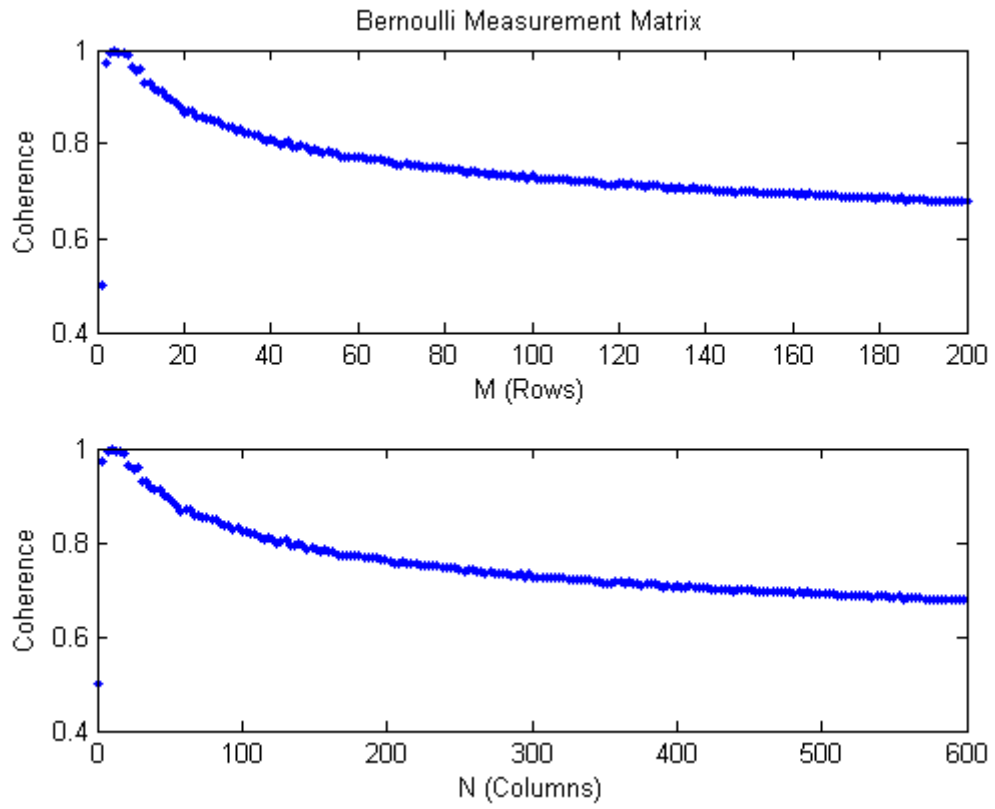
FIG. 2.8: Average Coherence of Bernoulli Random Matrix

Gaussian Random Matrix We analyze the coherence of a Gaussian random matrix of size 200x600, iterating 50 times.
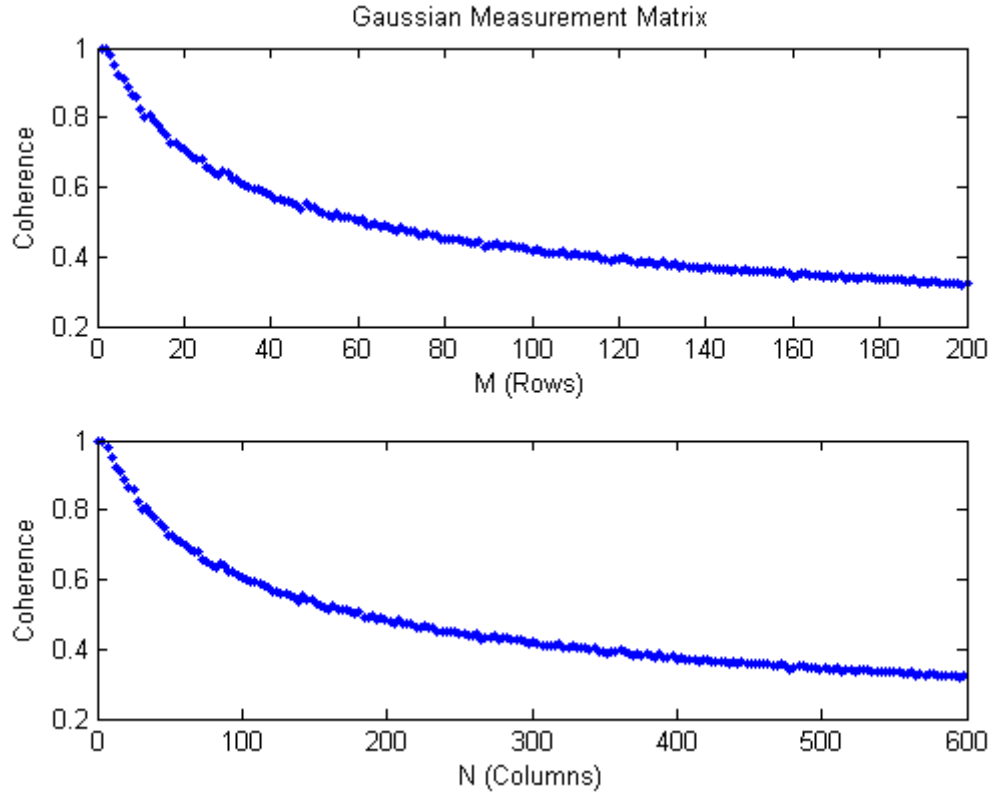
FIG. 2.9: Average Coherence of Gaussian Random Matrix

For the last iteration, at matrix 200x600, Bernoulli random matrix reached about 0.6786, whereas Gaussian random matrix reached about 0.3219. Hence, we can see that Guassian reaches a much lower coherence for the same size matrix. The speed up for Gaussian matrix is almost twice that of Bernoulli. Also, for both measurement matrices, we can see that coherence drops as the size of the matrix increases. In the simulatios performed in this proposal research, we use Bernoulli random matrix because of the ease in implementation at the detector level.

2.5 Reconstruction Algorithms

Once compressive sensing measurements are acquired, reconstruction algorithms need to be applied to obtain the sparse signal from the few measurements. There are two main categories of reconstruction algorithms: optimization techniques and greedy algorithms.

2.5.1 Optimization Techniques

Optimization techniques usually minimize a norm to obtain an optimal global solution. Few commonly used norms are defined below:

1. L_1 norm:

$$|x|_1 = \sum_{i=1}^{n} |x_i| \tag{2.16}$$

2. L_2 norm:

$$|x|_2 = \sum_{i=1}^{n} |x_i|^2 \tag{2.17}$$

Similarly any p- norm can be defined as:

$$|x|_p = \sum_{i=1}^{n} |x_i|^p \tag{2.18}$$

For the simulations in this section, reconstruction for the microlensing event was performed using L1 optimization algorithm. The following optimization problem was solved:

$$\min_{x} ||x||_1 \tag{2.19}$$

$$\text{subject to} |Ax - b| < 0.001 \tag{2.20}$$

23

This problem is solved by using convex optimization techniques. A primal-dual approach is used. Firstly, the problem can be rewritten as equation 2.22. The Lagrangian of this problem can be set as

$$min_x 1^T x \tag{2.21}$$

$$\text{subject to} |Ax - b| < 0.001 \tag{2.22}$$

The Lagrange is given by:

$$L(x, \lambda, \gamma) = 1^T x + \lambda(Ax - b - 0.001) + \gamma(b - Ax - 0.001) \tag{2.23}$$

By obtaining the infimum of the Lagrange over x, a dual problem can be generated. The solution to a dual problem provides a lower bound for the primal problem. Only for certain optimization problems, the duality gap is reduced to 0 (Boyd & Vandenberghe 2004). We use the package (O Donoghue *et al.* 2016) which uses splitting conic solver (SCS) to find the optimal solution to the problem stated in equation 2.20.

Similarly, as the primal problem is modified to suit a specific application, the corresponding dual problem is generated and solved by SCS algorithm. There are a variety of optimization problem solver as described in detail in (Bertsekas & Scientific 2015). However, in this research we use SCS due to its recent developments and comprehensive package, as well as its ability to perform well in our application.

2.5.2 Greedy algorithms

At each iteration, greedy algorithms obtain a local solution, and through consecutive iterations, the goal is to achieve the global solution. In (Needell, Tropp, & Vershynin 2008), a comprehensive review is given. In addition, (Needell & Vershynin 2010), (Tropp & Gilbert 2007), and (Cai & Wang 2011) provide implications of Orthogonal Matching Pursuit (OMP) and its derivants on applications relevant to CS. OMP is one of the commonly used greedy algorithms. OMP works by choosing the column of A which has the highest column correlation with the residual. We use OMP for all of our simulations due to its fast computation time.

GRAVITATIONAL MICROLENSING

PARAMETERS

To analyze time-series photometric measurements, we focus on gravitational microlensing curves, which are an example of time-series measurements. In this chapter we discuss microlensing parameters that could be sensitive to CS measurements. We conduct a preliminary analysis on lens-source separation parameter in this research work, while other parameters are to be researched in our future work. In addition we propose, implement, and analyze new differencing algorithms for Gaussian as well as Airy point spread functions.

3.1 Gravitational Microlensing Theory

Using Netwonian physics and Einstein's theory, the gravitational lensing equation shown in Equation 3.1 can be derived. The derivation is shown in Appendix A.

$$\beta = \theta - \alpha_d(\theta) \tag{3.1}$$

where β is the angular distance from the observer to the source, θ is the angular distance between the observer and the projected image, and α is the deflection

angle. In gravitational lensing, the surface brightness, which is the flux per area, is conserved. The total flux increases or decreases, since the area increases or decreases. In microlensing two images of the source star are created due to the distortion of light. However, these separate images are not observed, but rather, magnification or demagnification of the source is observed; the images are not resolved. Since the Jacobian matrix gives the amount of change in the source in each direction, the transformation of the original source to the "stretched" source, can be mapped by the Jacobian. The absolute value of the inverse of determinant (det) gives the amount of magnification.The magnification is given by

$$A_i = \frac{1}{det J} \tag{3.2}$$

Then, total magnification is

$$A = \sum_i |A_i| \tag{3.3}$$

In the next section, we analyze the image resolution and source magnification for single lens systems followed by binary and multiple lens systems.

3.2 Single lens System

In a single lens system, the lensing system consists only of a lensing star. This is the simplest model we first used for preliminary results. By assuming a point source, the magnification of the source star at each time is given by the source-lens separation, μ_0, peak magnification time, t_0, and Einstein's ring radius crossing time, t_e. We apply compressive sensing to simulated singles lens gravitational microlensing events.

Magnification as a function of time is given by equation 3.2.

$$A(t) = \frac{u_0^2 + \dfrac{(t-t_0)^2}{t_E} + 2}{(u_0^2 + \dfrac{(t-t_0)^2}{t_E})^{1/2}(u_0^2 + \dfrac{(t-t_0)^2}{t_E} + 4)^{1/2}} \tag{3.4}$$

3.2.1 Lens-Source Separation

In this research, we analyze the effects of compressive sensing on low magnification events due to large lens-source separations, normalized in terms of Einstien's ring radius. The lens-source separation parameter, μ_0, influences the magnification of the microlensing curve (Equation 3.2). We determine the uncertainty caused as we vary u_0 from 0.1 units to 0.9 units of Einstein's ring radius. We use 4% of Nyquist rate measurements. In this context, Nyquist rate refers to the total number of pixels in the image, which traditional methods would need to capture.
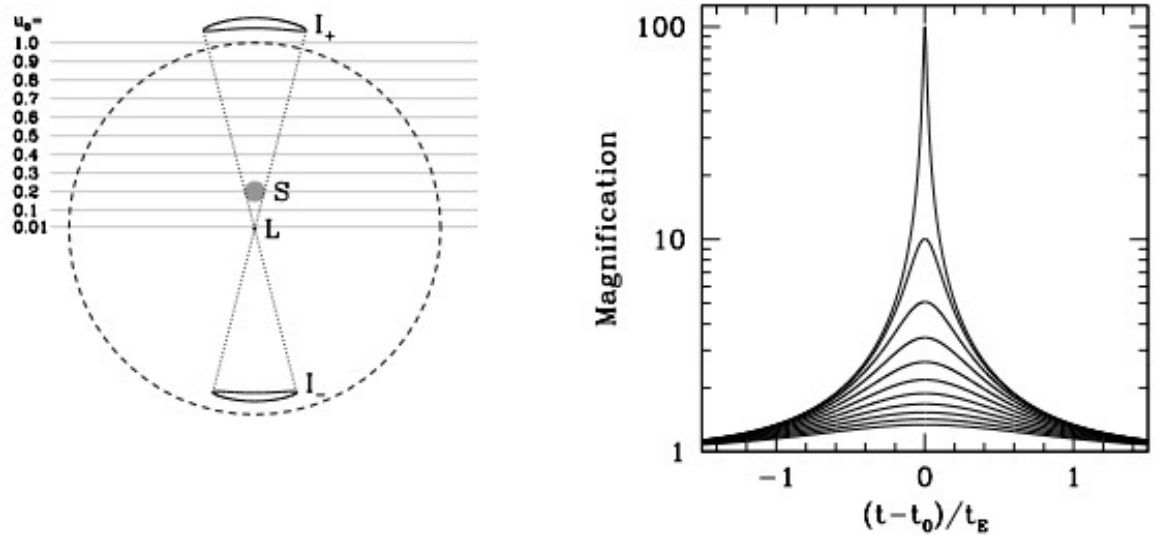
FIG. 3.1: Magnification for varying Lens-Source Separation parameters. Credit: (Seager 2010)

As u_0 increases, the magnification curve decreases in magnification at 0.

3.3   Binary and M-ary Lens Systems

Binary and M-ary lens systems do not have an analylical solution, and, hence, are very difficult to compute. Modelling techniques for generating microlensed event curves due to M-ary lens systems is provided in (Bozza 2010a). Figure 3.2 shows a sample binary lens event due to a lensing star and a planet.

3.3.1   Binary Lensing

Application of CS to single lens microlensing events can be extended to binary lens events. In a binary lens event, the lensing system consists of two bodies, typically a planet and a star.
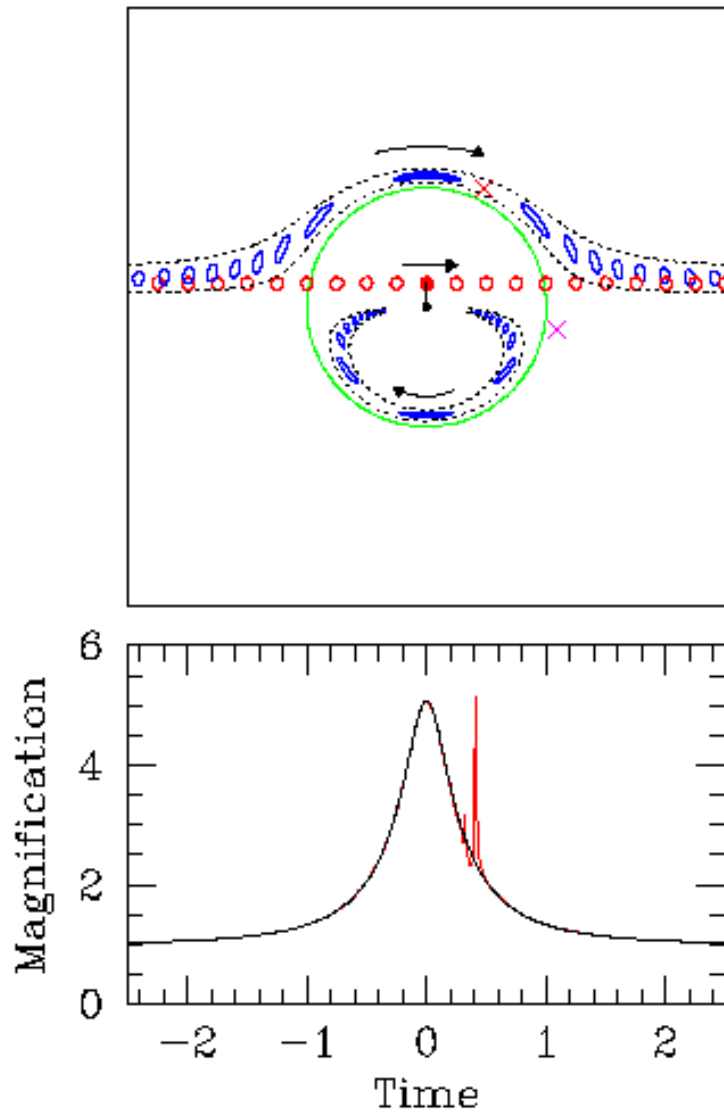
FIG. 3.2: Binary Lens Event

[Top Image]The black dot represents the lensing star and the red filled circle represents the source star. As the lens and source move in relative motion, the blue set of images will be created- one inside the Einstein's ring (green circle) and one outside. The separation between the two set of images is not resolved and hence,

30

will look like magnified flux to the observer. The red X represents a planet orbiting the lensing star. [Bottom Image] The black line is the microlensing curve due to the lensing star. The red spike is due to the distortion caused by a planet orbiting the lensing star. Credit: Astronomy Dept. of Ohio Statue University As seen from Figure 3.2, it is critical to capture short lived transits for binary or M-ary lens systems.

Critical curves and caustics   From application perspective, we can map out a time-series photometric curve using a detector, which takes images at t time samples. Once a light curve is generated using instrument data, it needs to be mapped back to the lensing parameters, which determine the characteristics of the lensing system.

The following flow chart maps the lensing equation values to the magnification curves. Hence, the obtained magnification curve from detector data can be mapped back to the lensing equation parameters.

To obtain the magnification:

- Input image positions using the lensing equation

- Find the Jacobian

- Amplification $= \dfrac{1}{|J|}$
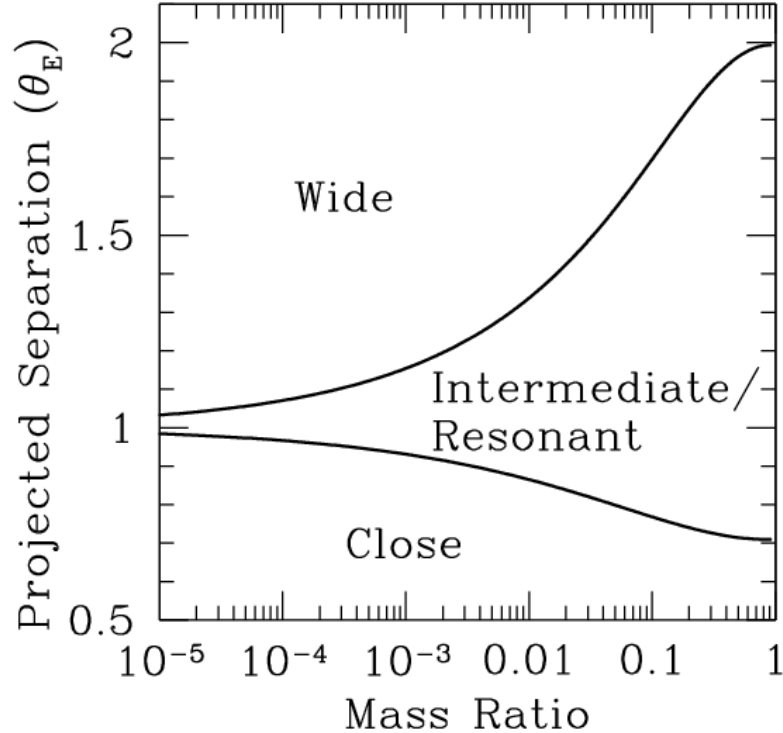
FIG. 3.3: critical curves based on projected separation and mass ratio. (Seager 2010)

Wide caustic topology gives two disjoint caustics, intermediate/resonant topology gives a single caustic, and a close topology gives three disjoint caustics. Depending on the trajectory, the magnification is given as the source passes through the caustic.

3.4   Simulations

For binary lens simulations, parameters are chosen such that the caustics cover all three topographies. In order to understand the effects of magnification due to the crossing of caustics, the trajectory angle is varied to cover a range of caustic curve crossings. We use the three caustic topographies as listed below.

- Wide Topography

- Intermediate/Resonant Topography

- Close Topography

3.5 Differencing Algorithms

To detect a microlensing event, scientists are only interested in star sources whose flux changes over time. In order to capture only the star sources with varying flux, differencing can be performed, where the observed image is differenced with a reference image, eliminating static star sources. Star variations can be caused by cosmic sources, or dimming of star flux due to planetary transits in addition to gravitational microlensing. However, there are very few stars sources experiencing magnification in their fluxes caused by gravitational microlensing. A reference image has a cleaner point spread function (PSF), that is, the spread of the point source is very narrow. This is usually generated by registering good seeing images. An observed image in our context is any image output of a detector system, typically with a worse seeing PSF.

3.5.1 Difference Image Analysis (DIA)

DIA is the current state-of-the-art algorithm for differencing images. Through literature search, we use the differencing algorithm provided by Bramich in (Bramich 2008) and (Albrow *et al.* 2009) as it uses a numerical kernel and is the latest improved version of the standard differencing method (Alard & Lupton 1998). The previous differencing method is based on the defining Gaussian basis function for the kernel. An implementation for OGLE-II based on that method is shown in (Wozniak 2000). However, the correct kernel may not be obtained if the pre-chosen basis functions were

inaccurate to begin with. Hence, this (Bramich 2008) algorithm uses a numerical kernel to match the PSF of the reference image with the observed image. Assuming σ_{ij}, pixel uncertainty, $= 1$, Equation 3.5 can be formulated as a least squares problem as shown in 3.6.

$$\chi^2 = \sum_{ij} (\frac{I_{ij} - M_{ij}}{\sigma_{ij}})^2 \tag{3.5}$$

$$\min_K ||I - M||_2^2 \tag{3.6}$$

where

$$M_{ij} = (R \star K)_{ij} + B_{ij} \tag{3.7}$$

$$= \sum_{lm} K_{lm} R_{(i+l)(j+m)} + B_0 \tag{3.8}$$

R is the referenced image and K is the kernel which registers the reference image with the observed image. We represent convolution as $\star$. B_{ij} is the background. Here background is kept at a constant B_0.

In order to minimize χ^2, we need to set the differential of Equation 3.5 to 0. As we optimizing K and B_0, we take differentials with respect to K and B_0. The implementation in Python is provided by Ian Crossfield.

3.6 Detectors Theory

Optical set up of telescopes can have a major impact on the quality of the image. The point source response of a detector is given by its point spread function (PSF).

In this section we discuss common aperture types and the PSF they generate.

3.6.1   Point Spread Functions

FIG. 3.4: Observed Image from a detector

As the light from a point source travels from the object plane to the lens into the image plane, it gets diffracted due to the lens as it reaches the image plane. Theory of diffraction of light due apertures is given in (Mansuripur 1986). PSF calculation is shown in Appendix B.

Airy Disk   Circular optics aperture give a PSF which has an airy disk pattern due to the diffraction of light through the optics (Tschunko 1974). This Airy disk pattern can be characterized using Bessel function as shown in 3.9, where J_1 is Bessel function of the first kind.

$$I(u) = \frac{1}{(1-\epsilon^2)^2}\left[\frac{2J_1(u)}{u} - \epsilon^2\frac{2J_1(\epsilon u)}{\epsilon u}\right]^2 \tag{3.9}$$

Here u is the distance from the optical axis and ϵ is the fractional radius of the primary aperture, and can be set to 0.

A sample Airy shaped PSF generated due to a circular aperture with 15m radius,

0.01 pixel scale, 3 arcsecond field of view and 2 microns wavelength, is shown in Figure 3.5. This PSF is generated by a Python library.
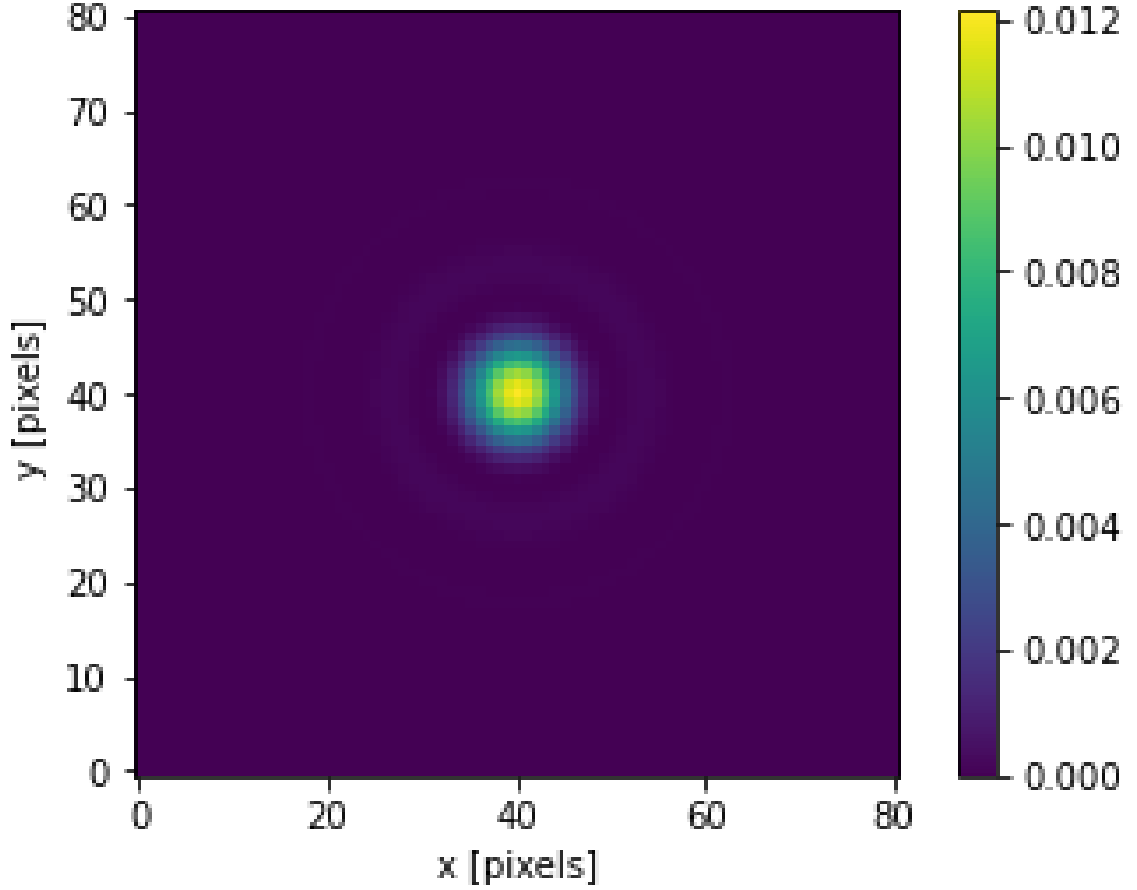
FIG. 3.5: Sample Airy Disk PSF

Gaussian   Gaussian PSFs are good approximate of Airy functions   (Raffel, Willert, & Kompenhans 1998) and can also be used to model detector optics. They are easier to mathematically model. Gaussian function can be modeled as:

$$f(x) = \frac{1}{2\sigma\sqrt{2\pi}}e^{\dfrac{-(x-\mu)^2}{2\sigma^2}} \tag{3.10}$$

36

In our simulations to depict real world applications, we generate star sources created by Airy shaped PSF of detector optics.

<center>**Chapter 4**</center>

COMPRESSIVE SENSING ARCHITECTURE

We show a CS architecture as applicable for transient photometry, specifically generated by gravitational microlensing events.

4.1 Gravitational Microlensing Application

In this section we give an overview of gravitational microlensing and its application in the architecture. Gravitational microlensing is a time-domain photometric application. Although we sample in spatial domain, the light curves are obtained in the time domain.

Analysis of gravitational microlensed events start from differenced images. As part of either the detector sensing or as part of post-processing, sampled spatial images are differenced with a reference image to obtain a differenced image. Figure 4.1 shows a clean reference image, an observed image in which one of the star sources experiences a change in flux, and a differenced image. The differenced image captures the change in flux of any of the star sources at the given time the observed image was taken.

<center>38</center>
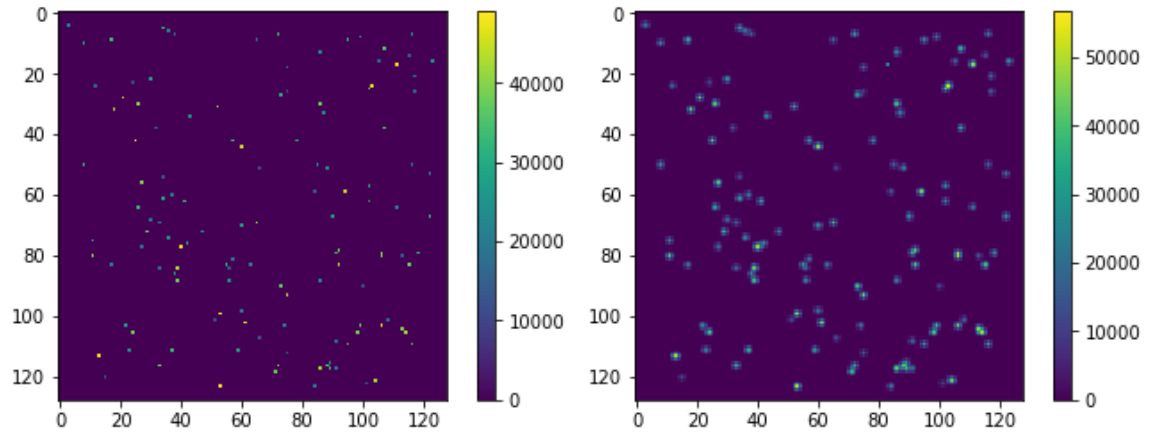
(a) Reference Image

(b) Observed Image
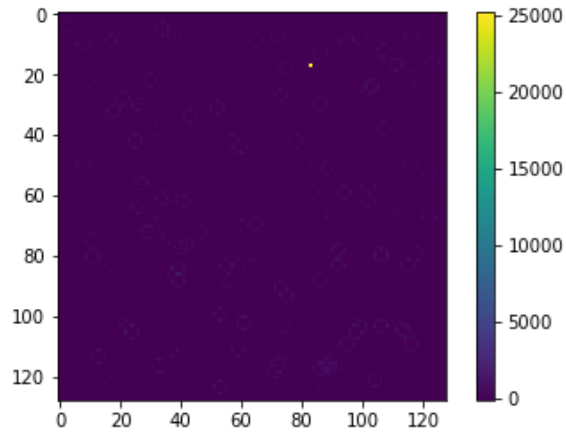
(c) Differenced Image

FIG. 4.1: Image Differencing

All such differenced images are taken and analyzed over time to generate a microlensing curve as shown in Figure 4.2.
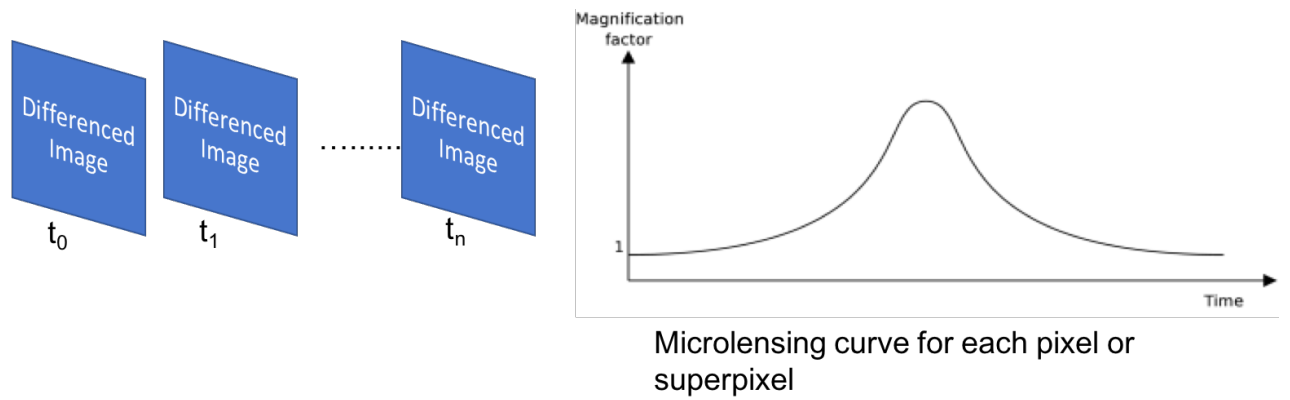
FIG. 4.2: Generating a Microlensing curve from differenced images

Using these mirolensing curves specific characteristics about the stars and planets in the lensing systems can be derived.

4.2 Architectures

CS framework will be applied as shown in Figure 4.3.
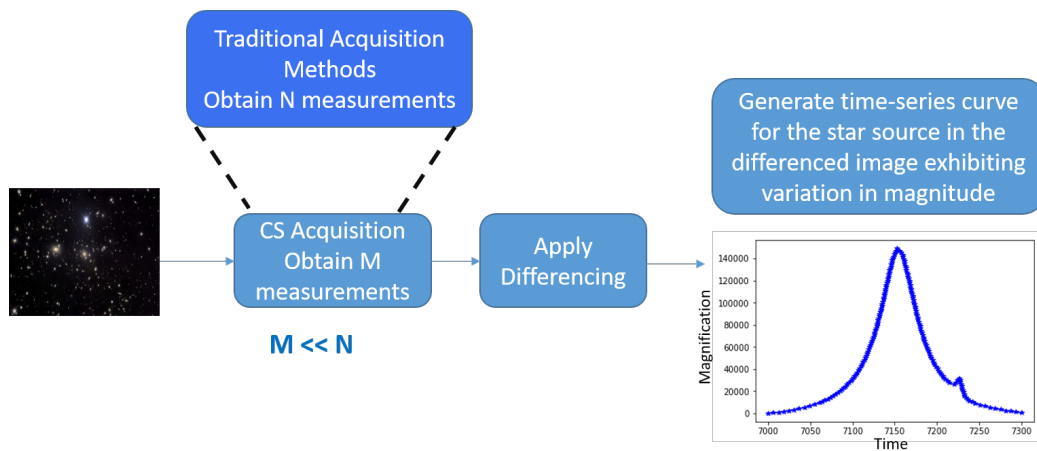
FIG. 4.3: CS Architecture implementation overview

We propose two architectures in this research. All architectures show implementation and processing up to the stage of obtaining a differenced image. The implementation shows a snapshot of sampling an image at one time.

4.2.1 Architecture I

In this architecture traditional CS methods are applied to acquire the spatial sky image.
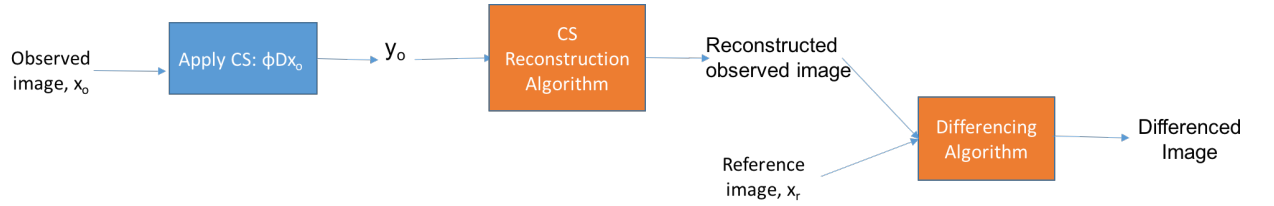
FIG. 4.4: CS Architecture I. Color code, blue: on-board spacecraft, orange: ground processing

The architecture show in Fig 4.4, uses sparse domain transformation as part of the projection process to sparsify the data. Sparse transformation in Figure 4.4 is shown using equation 2.4, but can be substituted by equation 2.2 as well. The projection consists of the measurement matrix and the sparse basis. Differencing in this architecture is performed on the reconstructed spatial domain images. Architecture I can be used as a survey observatory architecture, where the complete spatial sky image is acquired. This thesis focuses on Architecture II as it is more suitable for gravitational microlensing application.

4.2.2 Architecture II

The second architecture, shown in Figure 4.5, implements differencing at the CS measurements level. The output of this architecture is a differenced image. Thus, the original spatial sky image is not preserved. We study limitations and requirements of the measurement matrix for when CS in this architecture is realizable.
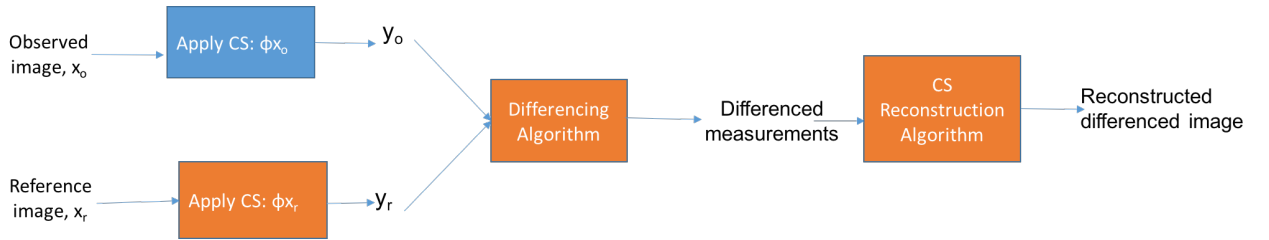
FIG. 4.5: CS Architecture II

Architecture II eliminates the need for sparsifying data as the reconstructed differenced signal would be sparse. This can reduce computational power and memory required for transforming into a sparse domain. A key difference between the two architectures is where differencing takes place - in architecture I, differencing is applied to the reconstructed images, where as in architecture II, differencing is applied to the measurements. As the measurements have a smaller dimension than the reconstructed images, computational power can also be reducded while differencing. We will further study these architectures to quantify the advantages of one over the other.

In general, architecture II, Figure 4.5, is not realizable with any measurement matrix, A, as shown in equations 4.1 - 4.5. Only if equation 5.7 is satisfied, the differencing of measurements, y, can result is a differenced image.

$$y_{diff} = y_o - (y_r \star M) \tag{4.1}$$

$$= Ax_o - ((Ax_r) \star M) \tag{4.2}$$

$$\neq Ax_o - A(x_r \star M)) \tag{4.3}$$

$$\neq A(x_o - (x_r \star M)) \tag{4.4}$$

$$\neq A(x_{diff}) \tag{4.5}$$

where $A = \psi$ and M is the kernel

$$y_{diff} = A(x_o - (x_r \star M)) \tag{4.6}$$

To overcome this limitation, we develop a suitable measurement matrix. Research from (Tropp 2006) shows that random filters using Toeplitz matrices (Gray & others 2006) can be used for compressive sensing as measurement matrices. Using random fiters and convolution, we can create a measurement matrix that will potentially satisfy equation 5.7.

Instead of using a matrix multiplication for projecting the measurement matrix, we can apply convolution (Tropp 2006) as shown in equation 4.7.

$$y_B = B \star x_o - ((B \star x_r) \star M) \tag{4.7}$$

Linear convolution is identical to multiplying the signal, x_o by a Toeplitz matrix. Let A be a quasi-Toeplitz matrix which is equal to the convolution of B with x_o as

shown in equation 4.12. Equation 4.9 is true because of the associative property of convolution.

$$B \star x_o - ((B \star x_r) \star M) \tag{4.8}$$

$$= B \star x_o - (B \star (x_r \star M)) \tag{4.9}$$

$$= Ax_o - (A(x_r \star M)) \tag{4.10}$$

$$= A(x_o - (x_r \star M)) \tag{4.11}$$

$$= y_{diff} \tag{4.12}$$

In the next section, we perform simulations to validate these theoretical results.

4.2.3   Simulation Results

We perform numerical simulations to verify the theoretical results. An nxn image is generated with n star sources at Gaussian randomly distributed locations and flux values. A kernel is generated for the purpose of verification. A Toeplitz matrix, A_{mxn} is created using Gaussian random values as shown in Figure 4.6. In our simulations, we use $n = 75$, $m = 0.5 \times n \times n = 2813$, and kernel, K is set as $[1, 2, 1]$. For simulation purposes, the $n \times n$ image is converted to a 1D vector. Hence, x_o and x_r are $1 \times (n \times n)$ or in this specific case, 1×5625. Here, we prove

$$y_o - (y_r \star K) = A(x_o - (x_r \star K)) \tag{4.13}$$

$$y_{diff} = A(x_{diff}) \tag{4.14}$$

Array length sizes due to convolution, subtraction and/or multiplication for both

44

left and right side of equation 4.14 are shown in Table 4.1 and Table 4.2, respectively. To determine convolution sizes, let $n \times n = p$, which is the size of x_o and x_r. Let k be the length of kernel and let m be the length of y_r and y_o. Due to the subtraction step involved, convolution of the same length as either y_o or x_o, for the right and left side of equation respectively, is performed. A full convolution for the left-hand side would give $m + k - 1 = 2815$, while for the right hand side would give $p + k - 1 = 5627$ multiplied by an $m \times p$ matrix. A valid convolution signal with complete overlap will have $m - k + 1$, where $m > k$, and $p - k + 1$, where $p > k$, for the left and right hand side of equation 4.14, respectively.

Table 4.1: Operation sizes for left hand side of equation 4.14 using same length convolution as y_o

Step	Convolution size
$y_r \star K$	$\max(m, k) = m$
$y_o - y_r \star K$	m length vector - m length vector $= m$

The first step contains end-points which do not completely overlap during convolution giving rise to boundary effects. These boundary effects are carried over in the second step as well.

Table 4.2: Operation sizes for right hand side of equation 4.14 using same length convolution as x_o

Step	Convolution size
$x_r \star K$	$\max(p, k) = p$
$x_o - x_r \star K$	p length vector - p length vector $= p$
$A(x_o - x_r \star K)$	m length vector

Similarly, the boundary effects take place here. This end-point values get carried over during multiplication with A, causing a mismatch with the y_{diff} values at the endpoint as seen in Figure 4.8. The valid portion of the convolution in which both the signals completely overlap are from $2 : m - 1$ for Table 4.1 and $2 : p - 1$ for Table 4.2.
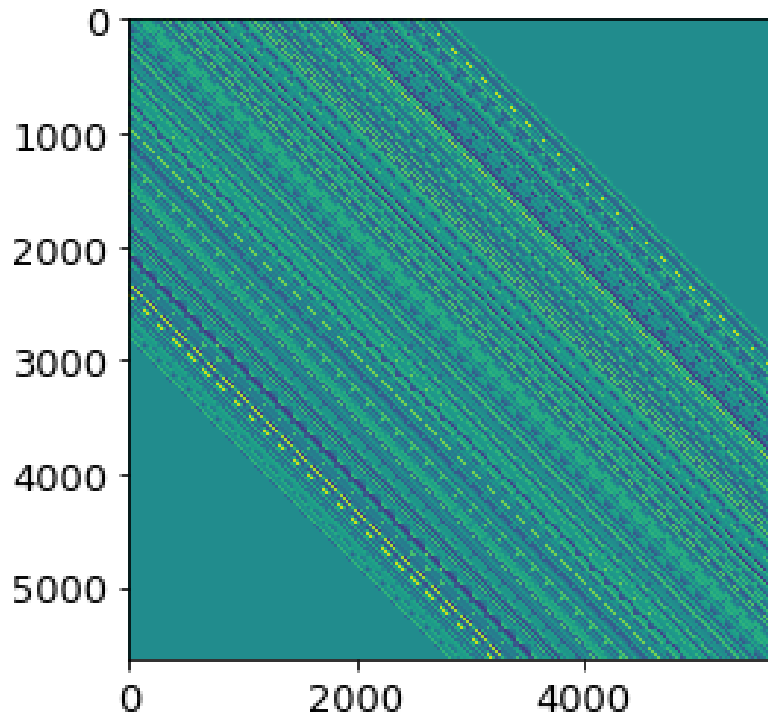
FIG. 4.6: Sample Quasi-Toeplitz matrix

Figure 4.6 is transposed and m rows are taken as shown in Figure 4.7 for the second step in table 4.1 to obtain y measurements and the third step in table 4.2.
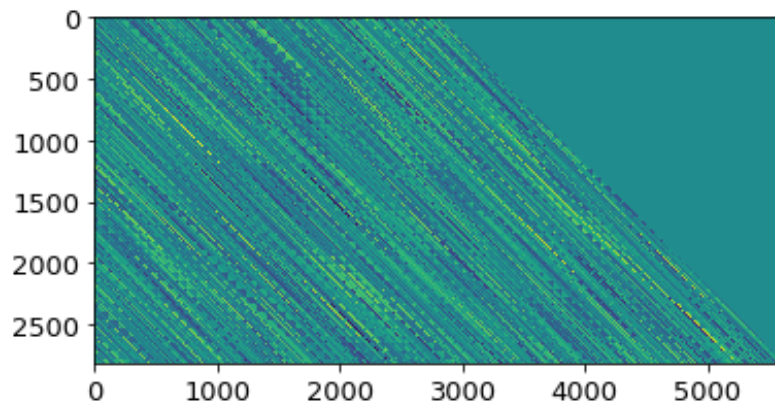
FIG. 4.7: m rows of Quasi-Toeplitz matrix

47
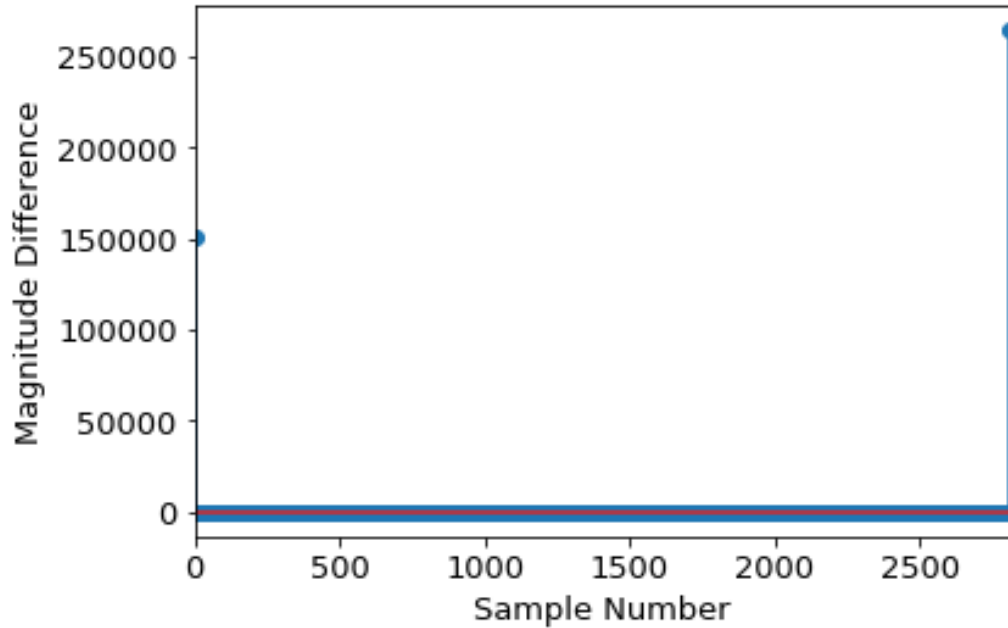
FIG. 4.8: difference between y_{diff} and Ax_{diff}

As seen from Figure 4.8, only the first and last element have a different value. This is because of the boundary conditions during convolution. The rest of the values are zero, hence, we can say that equation 4.14 is true.

Next, a complete CS experiment is performed to validate architecture II. In this experiment, 100 Monte Carlo simulations are performed. In this case, the kernel is found using $L1$ norm optimization technique, which is further discussed in Chapter 4. This experiment depicts Figure 4.5. Reference image has a Gaussian PSF of 0.1 units of pixel magnitude spread in both x and y direction, while the observed image has a Gaussian PSF of 0.5 units spread in both x and y direction. Both reference and observed image are 75×75 pixels. For simulation purposes, the images are converted to 1D signals of length $75 \times 75 = 5625$. The number of measurements is 50% of the total number of pixels, $(75 \text{ x } 75)/2 = 2812$. In this experiment, we compare the

following three methods:

1. Ideal case:

$$x_{diff} = x_o - (x_r \star k) \qquad (4.15)$$

2. Apply a Toeplitz matrix, A, as the measurement matrix and reconstruct x_{diff}. Here, A is the Toeplitz form of B, with B from 4.9.

$$y_{diff} = A(y_o - y_r \star k) \qquad (4.16)$$

Then use CS reconstruction algorithm to solve for x_{diff} using the obtained y_{diff}.

3. Apply a random matrix, C, as the measurement matrix and reconstruct x_{diff}. Theoretically, this method should not work correctly. However, we use this for validation to show that only Toeplitz matrix as in step 2 should provide an accurate solution.

$$y_{diff} = C(y_o - y_r \star k) \qquad (4.17)$$

Then use CS reconstruction algorithm to solve for x_{diff} using the obtained y_{diff}. For all the methods, L_1 minimization technique described in Chapter 4 is used. Both methods 2. and 3. are compared with the ideal result approximation obtained from 1. All three categories use the same differencing algorithm for an accurate comparison. The differenced image value (column two of Table 4.3) should ideally be zero, as we would want to obtain a kernel that perfectly matches the referenced image to the observed image. However, due to the limitations of the differencing algorithm, the possible minimum we can attain is obtained from method 1. A differenced image output from each of the methods from one simulation is shown in 4.9.
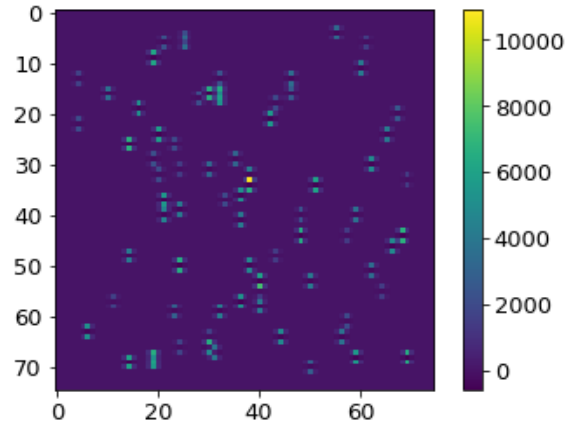
(a) Differenced Image, Method 1
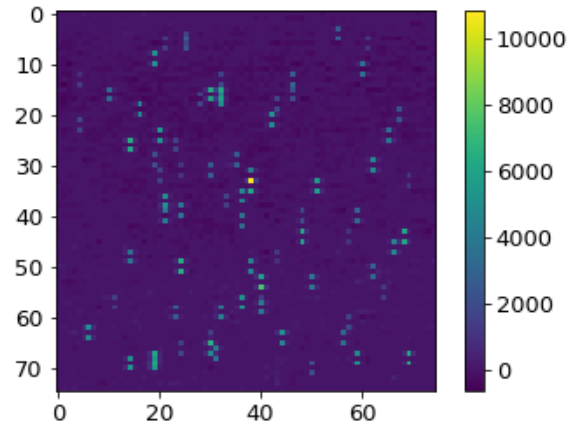
(b) Differenced Image, Method 2
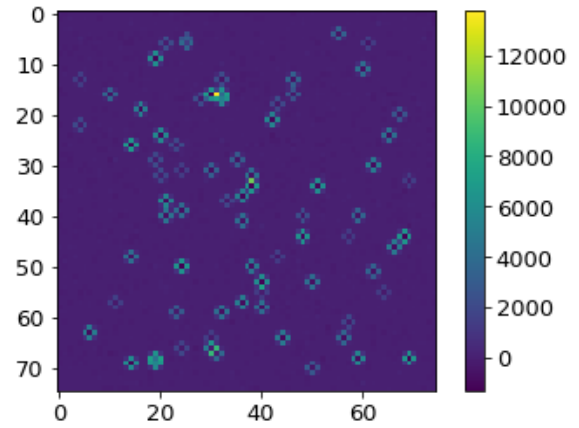
(c) Differenced Image, Method 3

FIG. 4.9: Image Differencing using the three methods

This shows that method 2 gives the same differenced image The average values over 100 simulations are shown in Table 4.3.

Table 4.3: Average value of the differenced image using the 3 different methods (described above)

Method number	Avg. of differenced image	std. deviation
1	147.21	7.87
2	142.24	14.84
3	250.88	11.95

As shown from equations 4.14, the kernels should be almost the same for method 2 as method 1. The table below shows the average difference between the kernel values over 100 Monte Carlo simulations for method 2 and method 3 as compared to method 1. As seen from table 4.4, average of the differenced image in method 2 is very close to that of method 1. The slight difference could be either due to the end-point variations because of incomplete overlap in convolution as discussed in the previous experiment or could be due to the limitations of CS reconstruction using 50% measurements. As expected method 3, has a much higher average value.

Table 4.4: Average difference between obtained kernel values

Method number	Avg. difference between kernels	std. deviation
2	0.0066	0.0046
3	0.061	0.0667

However, from the later chapters, we will know that 1D differencing algorithms do not work as well on 2D images, hence, the greater residual. To verify this method

with a microlensed event and 2D algorithms, we use a 128 by 128 image with 128 star sources. Out of those star sources, 1 star source experiences magnification of 5%. The reference image has a standard deviation PSF of 0.1, while the observed image has standard deviation of 0.5. We then reconstruct the images using the three methods. A sample reconstruction is shown in figure 4.10
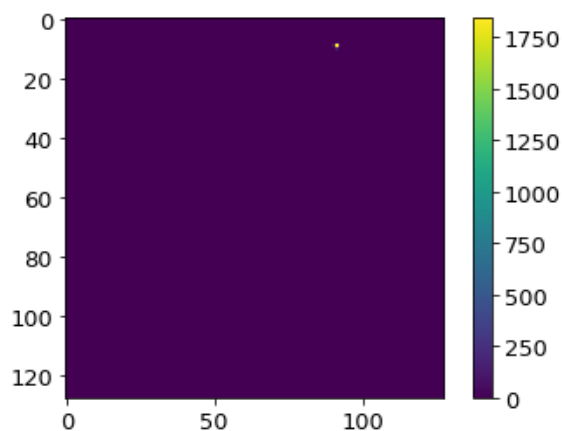
(a) Differenced Image, Method 1
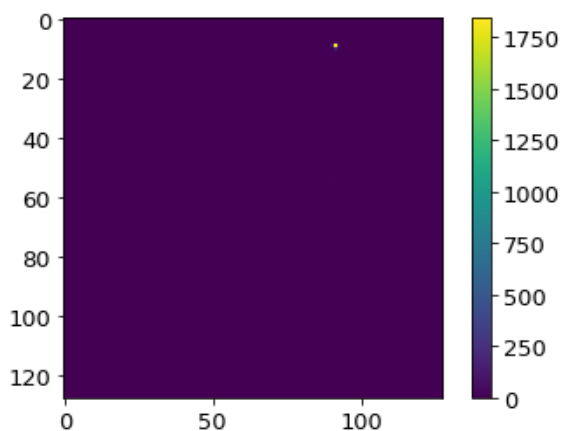
(b) Differenced Image, Method 2
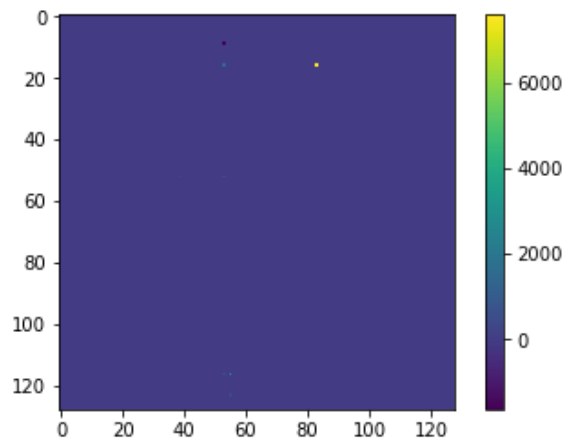
(c) Differenced Image, Method 3

FIG. 4.10: Image Differencing using the three methods

From Figure 4.10, we can see that Method 1 and 2 correctly identify the microlensed star source. As method 1 gives the ideal method comparison for our experiments, method 2 and method 3 are compared with method 1. From the results, method 2 resembles method 1 with an error between them of only 3.36%, while method 3 has an error of 100%.

For simplicity in our simulations moving forward, we can make the assumption that the PSF of the reference image and the observed image is the same. This can especially be valid for observations performed on space flight. However, in cases where this assumption is not true, we show a method to implement our CS techniques using a Toeplitz matrix.

COMPRESSIVE SENSING APPLICATION FOR GRAVITATIONAL MICROLENSING EVENTS

In gravitational lensing, the surface brightness, which is the flux per area, is conserved. The total flux increases or decreases, since the area increases or decreases. In microlensing, distinct images, due to the gravitational effects of the lensing system, are not seen, but rather, magnification or demagnification of the source star is observed; the images are not resolved. Since the Jacobian matrix gives the amount of change in the source star flux in each direction, the transformation of the original source to the stretched source, can be mapped by the Jacobian. The absolute value of the inverse of determinant gives the amount of magnification.

Einstein's ring forms when there is an exact alignment of the source, lens and observer and is an important parameter for the basis of gravitational microlensing equations. Einstein's ring radius, θ_E can be defined by equation 9.34.

$$\theta_E = \sqrt{\frac{4GMD_{LS}}{c^2 D_L D_S}} \tag{5.1}$$

where M is the the mass of the lensing system, D_{LS} is the distance from the lens to the source, D_L is the distance from the observer to the lensing system, and D_S is

the distance from the observer to the source (Seager 2010), (Tsapras 2018).

5.1 Single Lens Gravitationally Microlensed events

Here we describe the amplification value for each time as the source star moves in relation to the lensing system. Let **u** represent source position, and **y** represent image position, normalized by θ_E. Then, the lensing equation for a single lens microlensing event can be given as equation 5.2 (Seager 2010).

$$y_\pm = \pm\frac{\sqrt{u^2 + 4} \pm u}{2} \tag{5.2}$$

Total amplification of the two images formed is given by

$$A(u) = \frac{u^2 + 2}{u\sqrt{u^2 + 4}} \tag{5.3}$$

Due to the relative motion between the lens and source, amplification is dependent on the position of the source image at each time, t. Equation 6.13 shows the position of the source at each time given the trajectory the source takes (Seager 2010).

$$u(t) = \left[u_0^2 + \left(\frac{t - t_0}{t_E}\right)^2\right]^{1/2} \tag{5.4}$$

The trajectory is defined by the impact parameter, u_0, which is the minimum apparent separation between the lens and source in units of θ_E. Einstein ring radius crossing time is given by t_E and the time of peak magnification is given by t_0 (Seager 2010). The amplification with time dependency is shown in equation 7.24

$$A(t) = \frac{u_0^2 + \left(\dfrac{t - t_0}{t_E}\right)^2 + 2}{\left[u_0^2 + \left(\dfrac{t - t_0}{t_E}^2\right)\right]^{1/2} \left[u_0^2 + \left(\dfrac{t - t_0}{t_E}\right)^2 + 4)\right]^{1/2}} \tag{5.5}$$

5.2 Preliminary Results

In this section, we apply apply CS techniques to very simple microlensing data to identify the number of measurements needed for the recovery of a microlensing curve. This also establishes preliminary research on applying CS to time-domain photometric curves. In our setup, we show a sparse image with only a star source present.

5.2.1 Experiment I setup

We generate a microlensing curve for one source star with base flux value of one. Only star source is used in this simplified case. We use Gaussian PSF with a standard deviation of 0.2 in both x and y coordinates to depict the spread of the point source star. The event time scale, t_e, is 30 days, while the peak magnification time, t_0, is at the 15th day. Lens-source separation parameter, u_0, is 0.1 units of Einstein's ring radius. The sample star source is shown in Figure 5.1 and its corresponding microlensing curve ranging from $t = 1$ to $t = t_e$ is shown in 5.6. This image has N×N pixels, where N = 25. For CS we convert the image into a 1D vector of length 25×25 = 625. We use the toolbox provided by (Diamond & Boyd 2016) to reconstruct the signal using CS reconstruction algorithms.
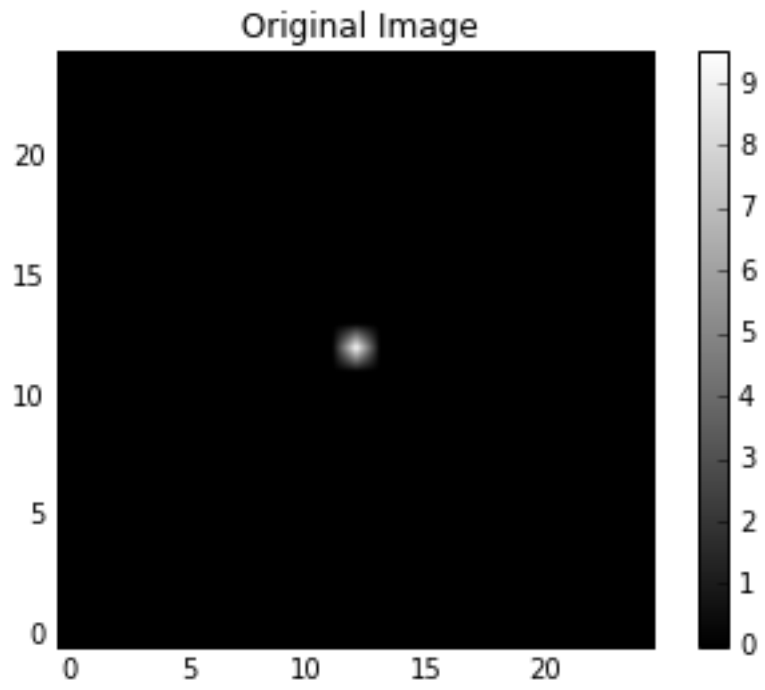
Fɪɢ. 5.1: Star source at peak magnification time
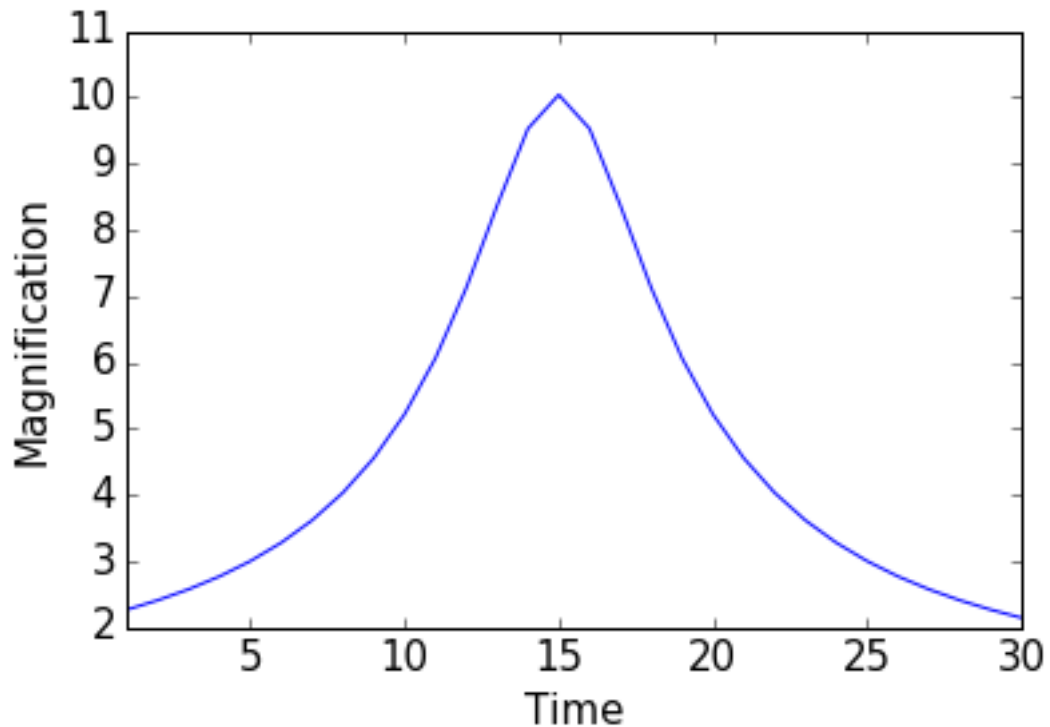
FIG. 5.2: Microlensing curve

At each time, t, the star source in the spatial domain image consisting changes its flux according to the microlening event curve. In this experiment we reconstruct the spatial domain image at each time, t, to generate a microlensing curve of that one star source.

5.2.2   Experiment I Results

In this preliminary research, we study the number of measurements required to reconstruct a single lens microlensing event with minimal error. We use a Bernoulli random measurement matrix, as it is know to be universally incoherent. In the first experiment, an L_1 minimization algorithm, SCS, is used.
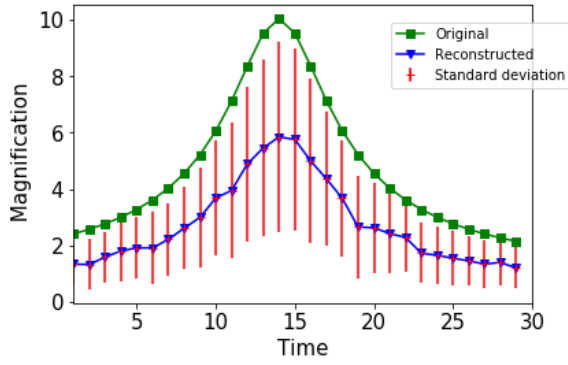
(a) Error bars using 2% measurements
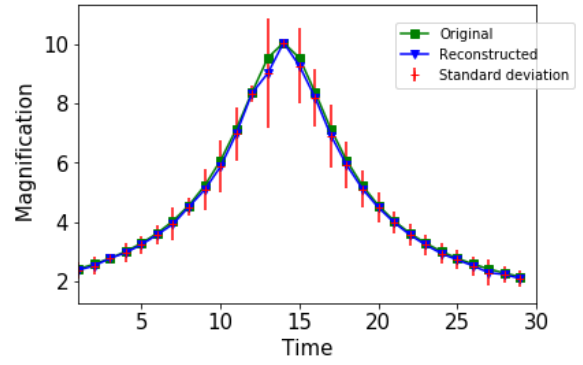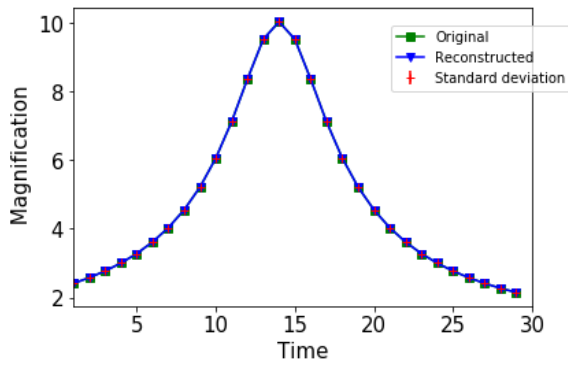
(b) Error bars using 3% measurements

(c) Error bars using 4% measurements
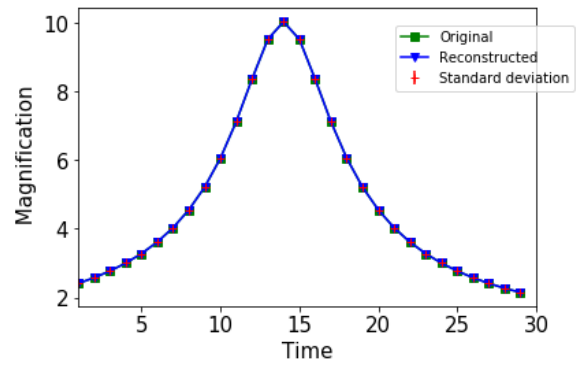
(d) Error bars using 5% measurements
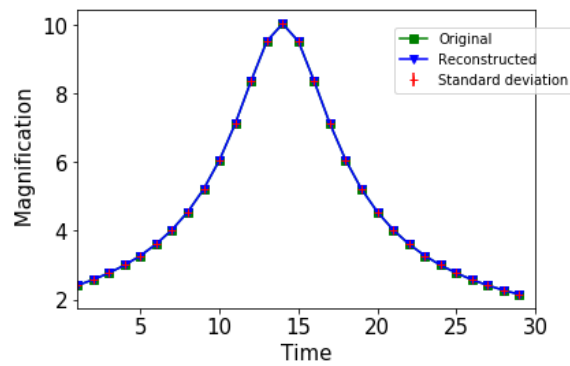
(e) Error bars using 6% measurements

FIG. 5.3: Error bars for varying % measurements using L_1 minimization technique for CS reconstruction

If we assume only the center pixel has a significant value, applying equation 2.11, we would need less than 1 measurement to accurately reconstruct the spatial domain image. However, in the time-domain event, it is evident from the simulations that in practical applications, the theoretical bounds are not very accurate and it depends on various other factors such as the data signal and measurement matrix. Table 5.1 shows error at specific time values for a varying number of measurements.

Error at t = 15	Error at t = 30	Avg. sdev over all t
4.07	0.86	1.60
0.52	0.044	0.52
4.15×10^{-5}	5.77×10^{-5}	9.64×10^{-4}
1.81×10^{-4}	2.58×10^{-4}	7.76×10^{-4}
4.19×10^{-5}	5.36×10^{-6}	7.32×10^{-4}

Table 5.1: Reconstruction Error (magnitude difference) and average standard deviation for 2% to 6% measurements, accordingly (top to bottom)
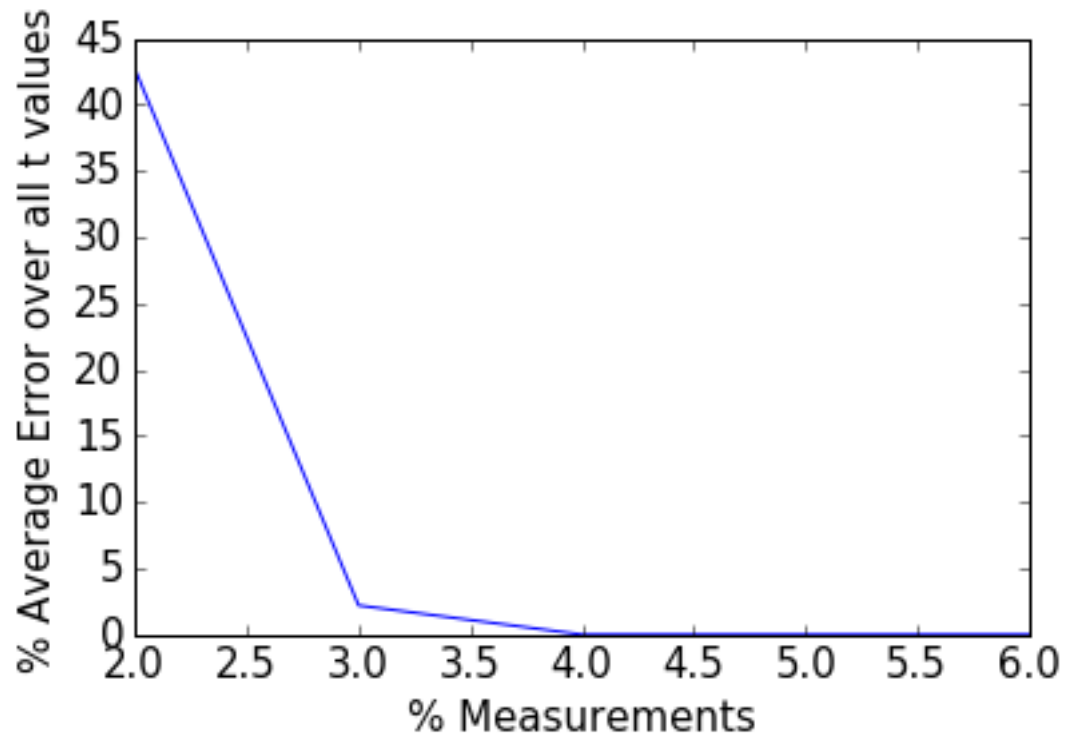
FIG. 5.4: Average Error over all t for center pixel with a 3-pixel radius for varying %Measurements $\left(\dfrac{M}{N} \text{ x } 100 \right)$ from 2% of N to 6% of N.

We repeat the same experiment, but instead use OMP as a reconstruction algorithm.
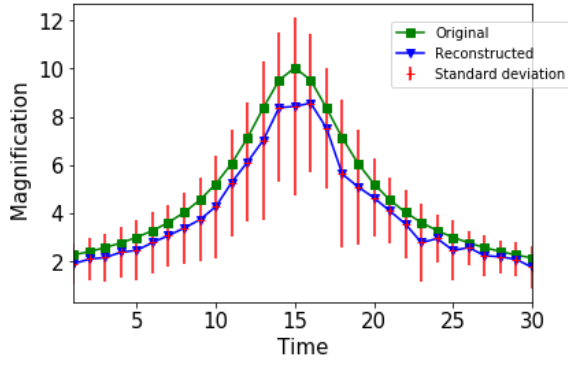
(a) Error bars using 2% measurements
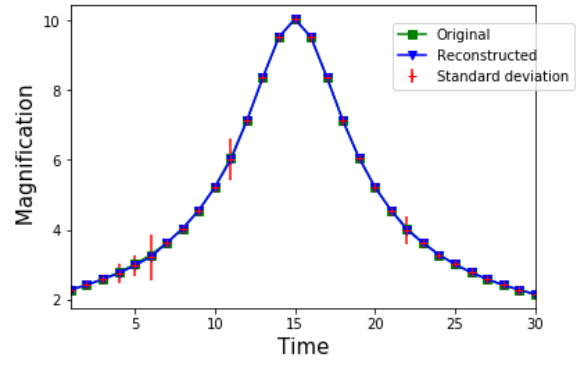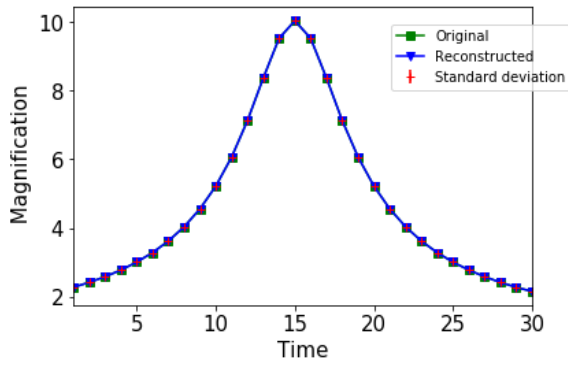
(b) Error bars using 3% measurements

(c) Error bars using 4% measurements
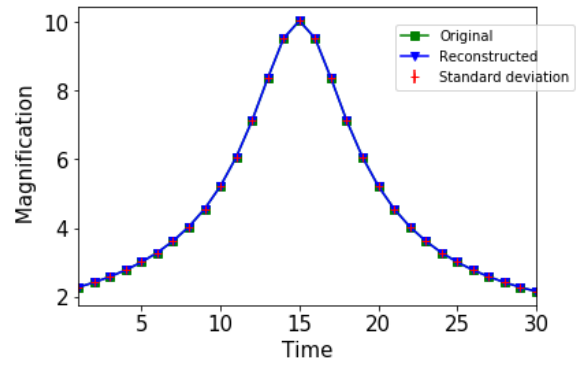
(d) Error bars using 5% measurements
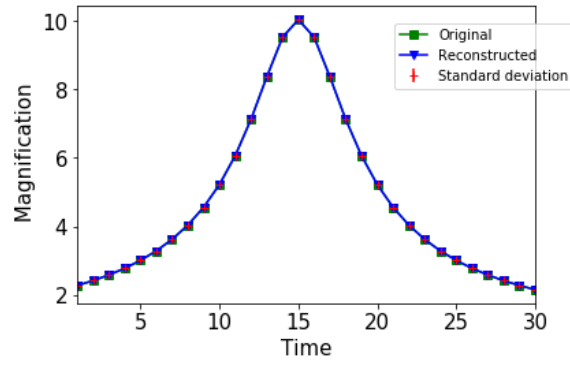
(e) Error bars using 6% measurements

FIG. 5.5: Error bars for varying % measurements using OMP algorithm for CS reconstruction
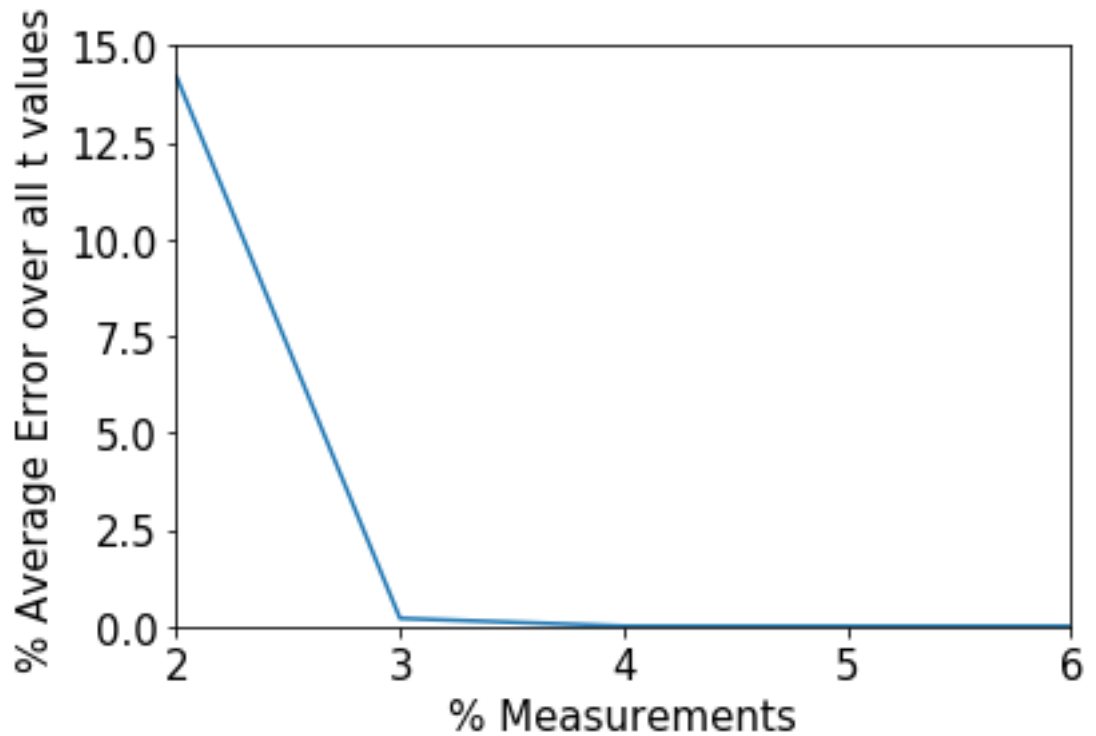
FIG. 5.6: Percent measurement

In this case, a greedy algorithm, OMP, worked slightly better than the L_1 minimization algorithm. We will further study and compare them to detect microlensing events in noisy detector images or crowded star fields.

In the next section, we study the effect of the impact parameter, u_0, on CS reconstruction.

5.2.3 Experiment II Setup

We use a 25x25 pixel image, with a source star at the center of the image. The measurement matrix consists of Bernoulli random values of 0's and 1's. For each time value, 100 Monte Carlo simulations are performed by varying the measurement

matrix. The center pixel in each image is portrayed as the source star with Gaussian distribution of flux in its surrounding pixels. Hence, while analyzing reconstruction of the microlensing curve, total flux or magnification is calculated using the center pixel with a 3 pixel radius. For all simulations, number of measurements, M, is 4% of N, where N is the total number of pixels in the image. Reconstruction is performed using an optimization algorithm provided in a software package by O'Donoghue *et. al* (2016).

5.2.4   Experiment II Results

Reconstructed microlensed curves for varying impact parameters are shown in Figure 5.7.
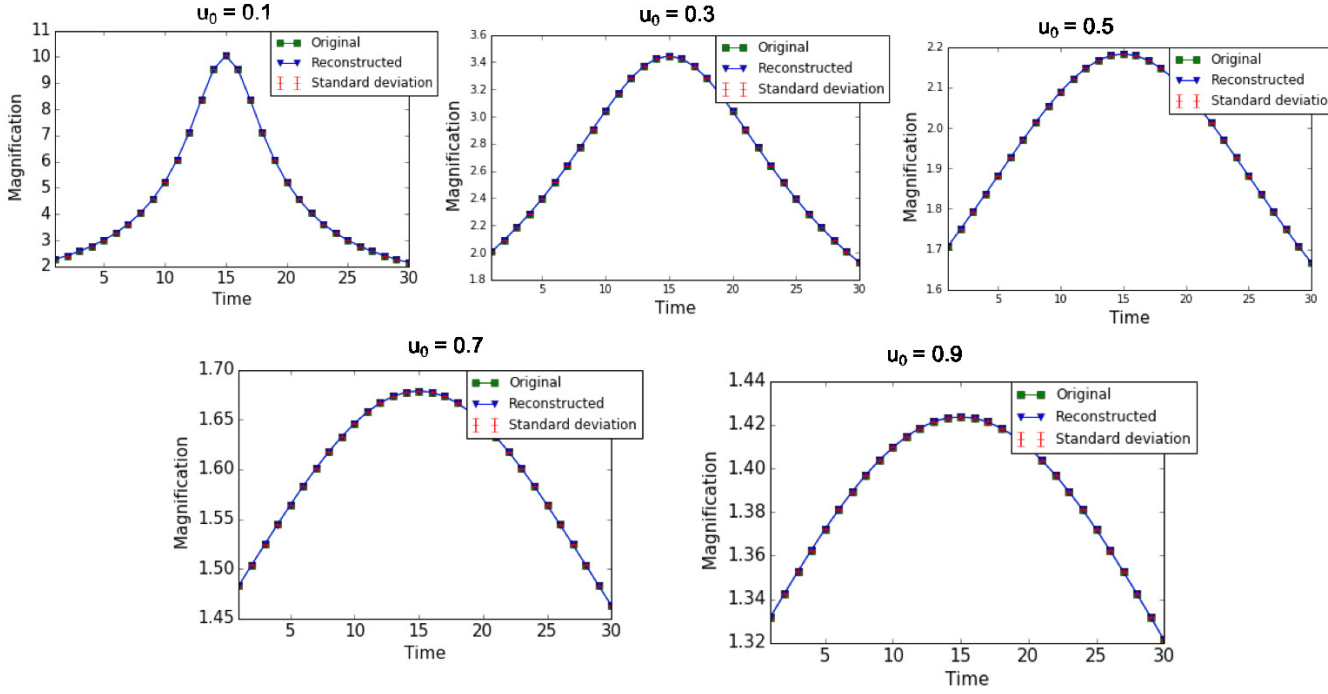
FIG. 5.7: Original and reconstructed microlensing curves with error bars for lens-source separation parameter u_0 ranging from 0.1 to 0.9.

Table 5.2: Ratio of uncertainty at t_0 to the difference in magnification at t_0 and $t_0 + / - 1$. This is to ensure that uncertainty is within limits to acquire a good resolution at peak time using 4% measurements

u_0	uncertainty at t_0: difference in magnitude between t_0 and $t_0 + / - 1$
0.1	0.0012
0.3	0.0268
0.5	0.192
0.7	0.334
0.9	1.046

Table 5.3: Average % error over all time values for each μ_0 using 4% of N measurements

u_0	Average % error
0.1	0.00160
0.3	0.00258
0.5	0.00272
0.7	0.00301
0.9	0.00334

Compressive sensing works well for low magnification events as seen from Figure 5.7. However, as the magnification decreases, uncertainty increases. In order to ensure key characteristics in the microlensing curve are captured, the uncertainty at peak magnification time, t_0, needs to be less than the difference in magnitude at the time before (or after) t_0. The ratio of uncertainty at t_0 to the difference in magnification between t_0 and $t_0 + /- 1$ is shown in Table 5.2. As μ_0 reaches 0.9 units of Einstein's ring radius, the ratio reaches slightly above 1, indicating the limits of CS reconstruction resolution. One way to overcome such a limitation is to increase the number of measurements. When we increase % of measurements for $\mu_0 = 0.9$ from 4% to 5%, the ratio decreases to 0.84. As the % of measurements increase, the error decreases, as expected. Table 5.3 shows average % error over 100 Monte Carlo simulations over all time values. Error is calculated using the difference in magnitude between the original and reconstructed image at the center pixel with a 3 pixel radius. From table 5.3, all μ_0 values give average reconstruction % error to be within 0.0000334 units of flux. Although % error is relatively low, uncertainty can reach a limiting factor as the lens-source characteristic distance increases. This leads to a trade-off between optimal number of measurements and resolution uncertainty.

5.3   CS Architecture with Implications on CS Reconstruction

In this section, we describe the implications of using Architecture II as the optimal architecture for CS data acquisition of transient photometric events.

We discuss a novel CS-based architecture for acquiring differenced crowded stellar images. Our research is targeted towards microlensing events, however, it can be extended to any astronomical events which require differenced images for observing transient events. Our previous work (Korde-Patel, Barry, & Mohsenin 2016a), (Korde-Patel, Barry, & Mohsenin 2016b) shows optimistic preliminary results for applying CS to very sparse spatial images consisting of a star source experiencing single lens microlensing event. This research extends to differenced images by applying a novel CS architecture. Figure 4.3 shows how CS is used as a data acquisition technique to obtain a photometric light curve.

A traditional CS based architecture will use a sparse domain transform, ϕ, to sparsify the crowded stellar field (Starck, Murtagh, & Fadili 2010b) (Rebollo-Neira & Bowley 2013), which would then be reconstructed using optimization techniques. The architecture overview is shown in Figure 4.4.

In this work, we demonstrate a CS based architecture for efficiently obtaining only the transient star sources in crowded stellar fields. Applying this technique to differenced images over time can help generate the light curve shown in Figure 4.3. This architecture, shown in Figure 4.5, implements differencing at the CS measurement level. The output of this architecture is a differenced image. Thus, the original spatial sky image is not preserved. We study limitations and requirements of this architecture.

The architecture is implemented in the following manner:

1. Obtain CS based measurements, y_o for a spatial image.

    CS can be applied by projecting a matrix, A, onto the region of interest, x_o.

This can be done on a column-by-column basis for a $n \times n$ spatial region, x_o. Thus, for 2D images, y_0 and A are of size $m \times n$, where $m << n$.

2. Given A and a clean reference image, x_r, construct measurements matrix y_r, where $y_r = A x_r$

3. Apply a 2D differencing algorithm on y_o and y_r to obtain a differenced image, y_{diff}, and the corresponding convolution kernel, M, which is used to match the observed and reference CS measurement vectors, y_o and y_r .

4. Reconstruct the differenced image, x'_{diff} using CS algorithms, given A and y_{diff}.

This architecture eliminates the need for sparsifying data as needed by traditional CS architectures since the reconstructed differenced signal would be sparse. This can reduce computational power and memory required for transforming into a sparse domain. As the measurements have a smaller dimension than the reconstructed images, computational power can also be reduced while differencing.

In this architecture, we create the differenced measurements matrix, y_{diff} by

$$y_{diff} = y_o - (y_r \star M) \tag{5.6}$$

$$= A x_o - (A x_r \star M) \tag{5.7}$$

Here x_o and x_r are the observed and reference images, respectively, and M is the obtained convolution kernel using differencing algorithm. The known parameters are A, y_o and x_r. Using differencing algorithms, we solve for M, to obtain y_{diff}.

For 2D images, if differencing gives optimal results, y_{diff} will have non-zero values in only the columns corresponding to the non-zero elements in x_{diff}. Hence, reconstructing y_{diff} using CS reconstruction techniques will give a sparse signal back, cor-

responding to x'_{diff}. To obtain the best results using CS techniques, x'diff has to be very sparse. Sparsity of x'diff in this case is dependent on two factors:

1. PSF: Images with fairly narrow PSFs, and reference and observed images which have a similar distribution PSF, give optimal results using differencing algorithms. This, in turn, produces sparser differenced images. If the PSFs are able to be matched perfectly using a differencing algorithm, the differenced image will only contain center pixels with magnitude difference between the two.

2. Magnification: Sparsity in CS can also be viewed as the rate at which the coefficients decay (Eldar & Kutyniok 2012). The higher the rate of decay of the coefficients, the sparser the image. Hence, higher magnification events give a sparser image compared to lower magnification events. When magnification factor is 1, ideal differencing should result in zero magnitude over all pixels. In the case of all zero magnitude pixels, the sparsity is zero. This can lead to erroneous results as the CS reconstruction algorithm searches for k non-zero pixel values.

We want to solve for x'_{diff} as this is the differenced image, which contains pertinent information for generating a microlensing light curve. In our simplified case study, we study the effects of magnification of a source star, depicting a time sample of the microlensing light curve. Magnification at the source star with position $[p_1, p_2]$ is defined as

$$x_o[p_1, p_2] = mf(x_s[p_1, p_2]) \star P_O \tag{5.8}$$

69

where mf is the magnification factor, ranging from 1 to 1.8 in our experiments.

$$y_{\text{diff}} = A(x_{\text{diff}}) \tag{5.9}$$

In equation (5.9), $x_{diff} = x_o - (x_r \star K)$.

where $\delta - \epsilon \leq K \leq \delta + \epsilon$, and δ is defined by equation (5.10). For equation (5.11) to hold true, ϵ must be 0. For small quantities of ϵ, the results are discussed in section 5.3.1.

$$\int_{t_0 a}^{t_0 b} \int_{t_1 a}^{t_1 b} \delta(t_0, t_1) dt = \begin{cases} 1, & \text{if } t_0 = p_1, t_1 = p_2 \\ 0, & \text{otherwise} \end{cases} \tag{5.10}$$

where $t_0 a < t_0 < t_0 b$ and $t_1 a < t_1 < t_1 b$

If $\epsilon = 0$, then

$$Ax_o - (Ax_r \star M) = A(x_o - (x_r \star K)) \tag{5.11}$$

In practical cases, differencing algorithms like Difference Image Analysis (DIA) are used to find this kernel given two images. Although a differenced image with no microlensing events will give sub-optimal results, an image with a microlensing event should increase image sparsity leading to better CS reconstruction results. We use a conic optimization algorithm as described in (Diamond & Boyd 2016) (O Donoghue *et al.* 2016) to solve the optimization problem shown in equation 5.12.

$$\text{minimize } ||x'_{diff}||_1 \text{ s.t.}$$
$$(Ax'_{\text{diff}} - y_{\text{diff}}) \leq 0.001 \tag{5.12}$$

5.3.1 Simulation Results

Using the proposed CS based architecture for 2D images, we apply CS on a column-by-column basis for a 2D spatial crowded stellar field. We use a 128x128 size image with 128 star sources spread across spatially in a random uniform manner. The flux of these star sources are also generated uniform randomly within the range of $[10000, 50000]$ units of pixel magnitude. Figure 5.8 and Figure 5.9 show a clean reference image and an observed image with a worse seeing PSF, respectively. For CS, a Gaussian normal random measurement matrix is applied. We analyze the average % error and standard deviation of the error over 100 Monte Carlo simulations, where the random Gaussian measurement matrix is varied. Given the CS architecture described in section 4, we reconstruct a differenced image, and then analyze the accuracy in reconstruction of the microlensing photometric curve over time. The reconstructed result (sample image shown in Figure 5.11) is compared to that of the differenced image resulting from applying DIA on the spatial domain images, x_o and x_r (sample image shown in Figure 5.10). Statistical error analysis using varying parameters is shown in tables 5.4, 5.5, 5.6, and 5.7. As DIA is the current state-of-art differencing algorithm, we use that as our basis for comparison. The % error is calculated by

$$\frac{|x'[s_0, s_1] - x[s_0, s_1]|}{x[s_0, s_1]} \times 100\% \tag{5.13}$$

Here, s_0 and s_1 are pixel indices corresponding to the center pixel of the star experiencing a change in flux. $x[s_0, s_1]$ is the DIA output value at position $[s_0, s_1]$. Similarly $x'[s_0, s_1]$ is the reconstructed differenced image value at position $[s_0, s_1]$.
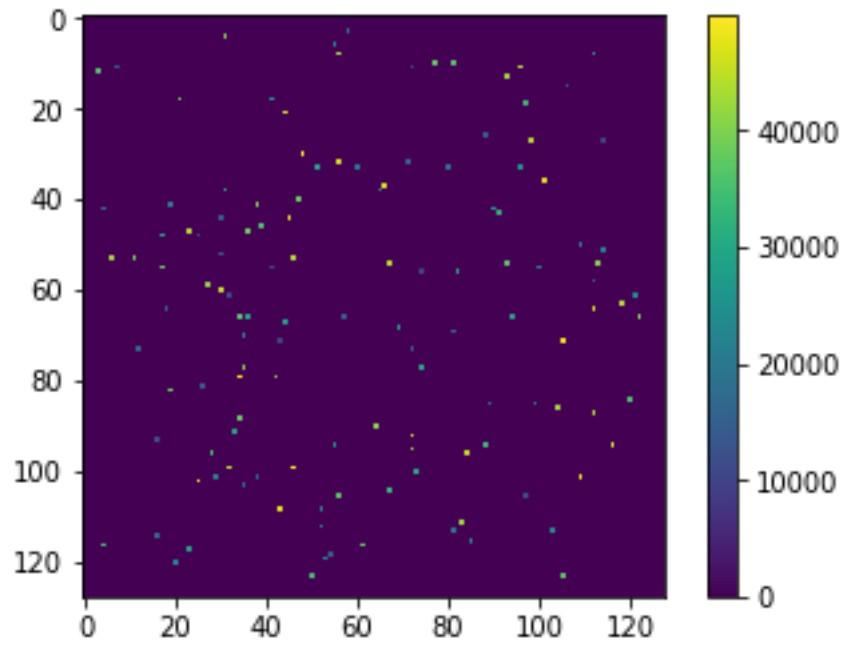
FIG. 5.8: Reference Image with 0.1 pixel units standard deviation PSF
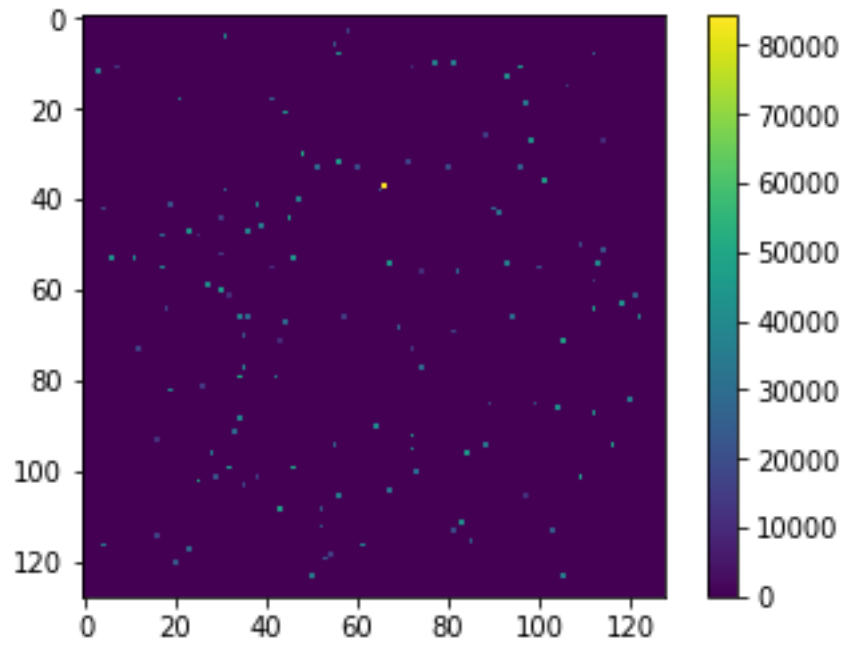
FIG. 5.9: Observed Image with 0.3 pixel units standard deviation PSF
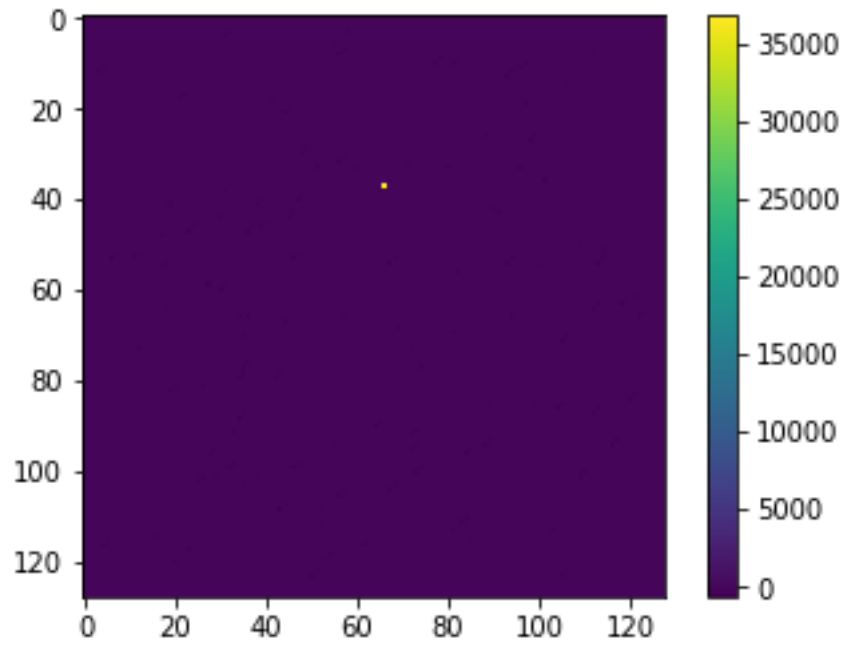
Fig. 5.10: Residual after differencing using DIA
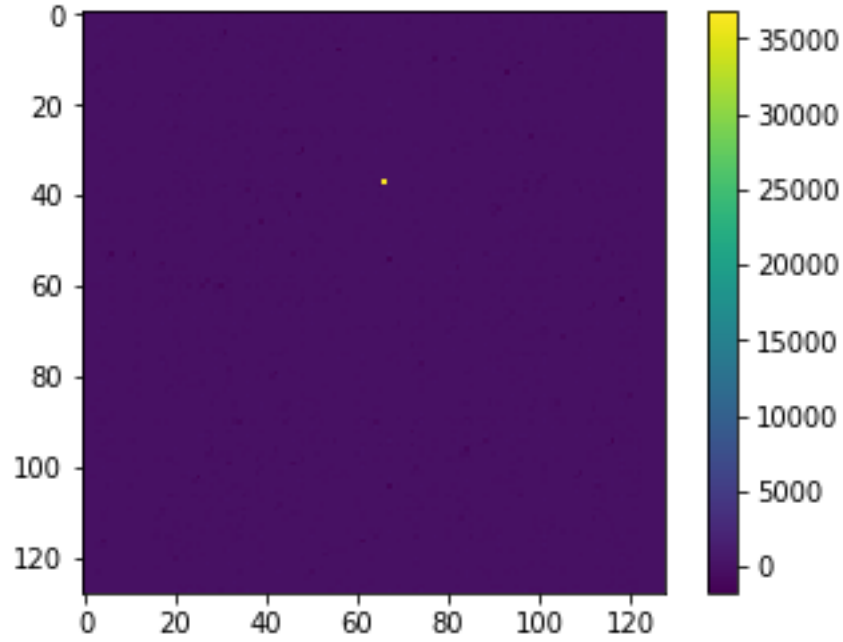
FIG. 5.11: Reconstructed residual using CS techniques with 10% of Nyquist rate measurements

Simulations are performed for a reference image with a PSF of 0.1 pixel units of standard deviation for a Gaussian spread PSF in both x and y direction. Similarly, the observed image has a PSF with standard deviation of 0.1, 0.3 or 0.5 pixel units. In table 5.4, the PSF of the reference image is 0.1 pixel units and PSF of observed image is 0.3 pixel units. In this case, the kernel is known *a priori*. Hence, in equation 7.5, M is known. Magnification factor is used to calculate the amplification value of the source star at position $[s_0, s_1]$:

Amplification Value = Source star value $\times$ magnification factor

Table 5.4: Average % error in magnitude of the source star and standard deviation of error over 100 Monte Carlo simulations.

Convolution kernel, M is known.

Observed image PSF $= 0.3$

Reference image PSF $= 0.1$

Magnification Factor	Average % error	standard deviation of error
1	100	0.093
1.2	0.73	0.0073
1.4	1.87	0.099
1.6	0.75	0.0077
1.8	0.73	0.0072

Table 5.5: Average % error in magnitude of the source star and standard deviation of error over 100 Monte Carlo simulations.

Observed image PSF = 0.1

Reference image PSF = 0.1.

Magnification Factor	Average % error	standard deviation of error
1	100+	1244
1.2	1.75	0.0090
1.4	1.70	0.0097
1.6	1.64	0.0090
1.8	1.71	0.0090

Table 5.6: Average % error in magnitude of the source star and standard deviation of error over 100 Monte Carlo simulations.

Observed image PSF = 0.3

reference image PSF = 0.1.

Magnification Factor	Average % error (m = 0.1×n, m = 0.3×n)	standard deviation of error (m = 0.1×n, m = 0.3×n)
1	100+, 100+	$2.6\times10^8, 4.86\times10^8$
1.2	7.2, 1.76	0.037, 0.0041
1.4	6.2, 0.78	0.099, 0.0017
1.6	4.1, 0.49	0.018, 0.0013
1.8	4.0, 0.28	0.0197, 0.0012

Table 5.7: Average % error in magnitude of the source star and standard deviation of error over 100 Monte Carlo simulations.

Number of measurements is 10% of n and 50% of n, where n = 128

Observed image PSF = 0.5

reference image PSF = 0.1

Magnification Factor	Average % error (m = 0.1×n, m = 0.5×n)	standard deviation of error (m = 0.1×n, m = 0.5×n)
1	100+, 100+	14751, 3416
1.2	87.06, 75.13	0.26, 0.38
1.4	47.59, 28.23	0.36, 0.30
1.6	32.13, 15.17	0.22, 0.19
1.8	33.34, 8.96	0.17, 0.13

Table 5.8: Legend descriptions for plots in Figure 5.12

Marker Name	Table Reference	Description
r1	Table I	Convolution Kernel is known
		10% of Nyquist rate measurements used
		Observed image PSF = 0.3
		Reference image PSF = 0.1
r2	Table II	Convolution Kernel is unknown
		10% of Nyquist rate measurements used
		Observed image PSF = 0.1
		Reference image PSF = 0.1
r3a	Table III	Convolution Kernel is unknown
		10% of Nyquist rate measurements used
		Observed image PSF = 0.3
		Reference image PSF = 0.1
r3b	Table III	Convolution Kernel is unknown
		30% of Nyquist rate measurements used
		Observed image PSF = 0.3
		Reference image PSF = 0.1

Table 5.9: Continuation of legend descriptions for plots in Figure 5.12

Marker Name	Table Reference	Description
r4a	Table IV	Convolution Kernel is unknown
		10% of Nyquist rate measurements used
		Observed image PSF = 0.5
		Reference image PSF = 0.1
r4b	Table IV	Convolution Kernel is unknown
		50% of Nyquist rate measurements used
		Observed image PSF = 0.5
		Reference image PSF = 0.1

When the magnification factor is 1, there is no change in the magnification of the source star. Hence, the resulting differenced image should have ideally all zero value pixels if the differencing works perfectly. However, for CS to give optimal results, the differenced image must be sparse, that is, the coefficients in the differenced image must decay at a high rate, which is not the case if all of the pixel values are close to zero. This results in the higher % error when there is no change in magnification (magnification factor = 1).

We show that for when the observed image PSF is similar in characteristics as the reference image PSF, the error in CS reconstruction is significantly lower. A summary plot is shown in Figure 5.12. The legends are described in table 5.9.
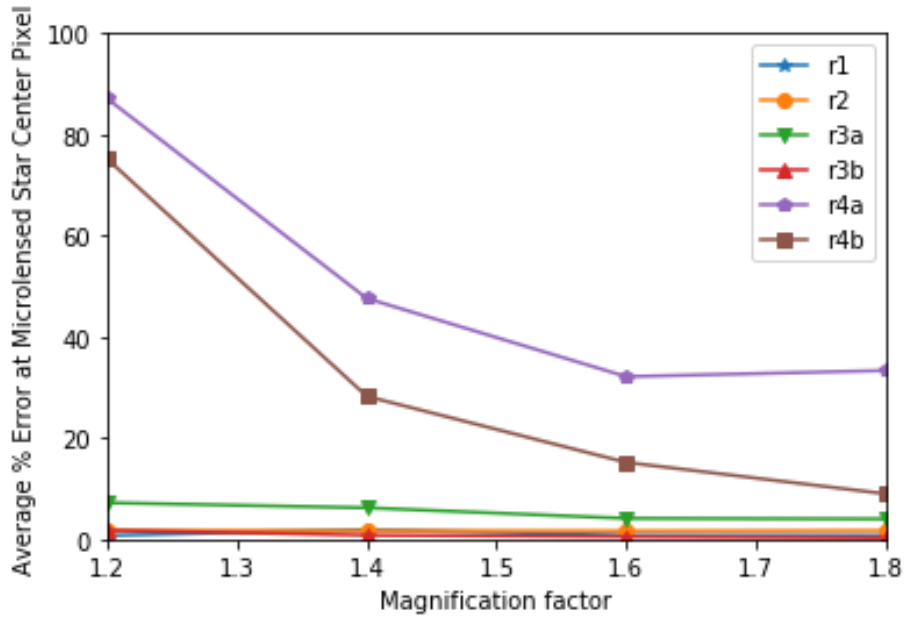
FIG. 5.12: Average % Errors for the configureations shown in table 5.9

From the results it is evident that when no magnification takes place, the differenced image is not sparse, hence, CS does not work well. A 100% error indicates a false positive, that is, the differenced image value of the pixels indicating the presence of the source star is zero, but a non-zero value is detected. However, as magnification factor increases, CS results give minimal error. This architecture gives optimal results in either of three circumstances, given a transient event is taking place:

1. Convolution kernel for differencing is known *a priori*

2. PSF of an observed image has similar characteristics as the reference image PSF

3. There is a significant change in magnification of a star source experiencing a transient event

If these requirements are not met, the number of measurements can be increased to reduce the error. Table 5.7, shows how the error can be drastically reduced by increasing the number of measurements from 10% of n to 50% of n. In cases where the ratio of PSF of the reference image to observed image is 1 : 5 for a magnification factor of 1.8, the error is reduced to less than 10% with 50% measurements.

Furthermore, it is evident that CS techniques can work within 10% accuracy using only 10% of the required samples for crowded stellar fields when both the reference and observed image have fairly narrow PSF widths and there is a transient star source present. The error can significantly reduce, to less than 2% by increasing the number of measurements to 30% of the Nyquist sampling rate. For detector read-outs with a very clean PSF, we can reconstruct the images within 2% accuracy using only 10% measurements. We also show that CS techniques fail when the differenced image of interest is not sparse. As we can see when none of the stars experience any variation in magnitude, the resulting differenced image should all have pixel values close to zero. This results in a non-sparse image. Furthermore, we show that this novel CS based architecture eliminates the need to find a sparse transformation domain, while reconstructing only the needed information to do transient photometric science.

5.3.2   Results Summary

To summarize, this study shows promising results for applying CS on crowded star fields to detect and characterize transient events, such as the ones produced through gravitational microlensing. This could be a game-changing technology in the way we acquire data to efficiently capture and reconstruct samples which are of importance to science, while discarding wasteful samples. This process significantly reduces the on-board storage, power, and transmission requirements. The results of this study show that for a crowded star field with clean seeing, we need to acquire

only 10% of the Nyquist rate samples to correctly capture a change in star magnitude over time. There is a trade-off with the % of measurements required and the accuracy in reconstruction, which can be studied as applicable to each science need. Further study in differencing algorithms for measurement vectors obtained through CS will produce even better results in CS reconstruction of the differenced images.

5.4   Error sensitivity of CS techniques on microlensing parameters

In this section, we show the error sensitivity for a realistic crowded stellar field (Korde-Patel, Barry, & Mohsenin 2022). We apply CS using architecture from Figure 4.5. In these set of simulations, we take into consideration both reference and observed images, in order to generate a photometric curve. We show the relation of error to the sensitivity of the parameter θ_E. For an error of $\epsilon(t)$ in the change in amplification at any given time, the amplification at each time changes by $A(t) + \epsilon(t)$. This change in $\epsilon(t)$ at each time, t, changes the amplification equation derived due to two images resulting from a single lens microlensing event. Using equation 6.13, equation 7.24 can be written as 5.14.

$$A(t) = \frac{u^2(t) + 2}{u(t)\sqrt{[u^2(t) + 4]}} \tag{5.14}$$

Incorporating error, we get equation 5.15.

$$A(t) + \epsilon(t) = \frac{u^2(t) + 2 + \epsilon(t)\left[u(t)\sqrt{u^2(t) + 4}\right]}{u(t)\sqrt{u^2(t) + 4}} \tag{5.15}$$

From equation 5.15, it is evident that a change in the light curve due to an error, $\epsilon(t)$, will not merely result in a change in u_0, but rather a change in the lensing system itself. That is, the light curve produced would not be accurately mapped to a lensing system.

In order to better understand analytical effects of error on science parameters, here, we show the effect of the change in science parameter and its implication on the amplification value. For a change of γ in the value of θ_E, which depends on the properties of the lensing system, as noted in equation 9.34, we can define, $\tilde{\theta_E}$ as

$$\tilde{\theta}_E = \gamma\theta_E \tag{5.16}$$

Using this $\tilde{\theta_E}$ in the lensing system, we derive the new amplification curve shown in equation 5.18. In our model, for $\tilde{A}(t)$, we scale u_0 by θ_E and not by $\tilde{\theta}_E$ to keep the same u_0 scale for comparison to $A(t)$.

$$A(u) = \frac{u^2 + 2\gamma^2}{u\sqrt{u^2 + 4\gamma^2}} \tag{5.17}$$

Expanding to include the definition of $u(t)$, we get equation 5.18.

$$\tilde{A}(t) = \frac{u_0^2 + \left(\dfrac{t - t_0}{t_E}\right)^2 + 2\gamma^2}{\left[u_0^2 + \left(\dfrac{t - t_0}{t_E}\right)^2\right]^{1/2}\left[u_0^2 + \left(\dfrac{t - t_0}{t_E}\right)^2 + 4\gamma^2)\right]^{1/2}} \tag{5.18}$$

To analyze the effect of compressive sensing errors, for single microlensing events, we consider the effect of θ_E on the amplification value. In equation 7.24, u_0 is in units of θ_E. Hence, a change of γ in θ_E, will directly affect the mass and distance parameters, M, D_LS, D_L and D_S of the lensing system. Our CS based modelling incorporates γ to determine the effect of errors due to CS application on the value of θ_E.

For astronomical measurements, the detector measures the flux of the source star. Hence, for microlensing, total flux received from the source star is given by equation 5.19.

$$F(t) = F_s A(t) + F_b \tag{5.19}$$

where F_s is the flux from the source, A is the amplification amount and F_b is the blended flux. In our simulation modelling, we use $F_b = 0$ for simplicity.

5.4.1 Binary Lensed Gravitational Microlensed Events

A binary microlensed system consists of two lensing bodies, which act as a lens, deflecting the light from the observed source star. Here, we have two lensing bodies with mass, m_1 and m_2, where $m_1 + m_2 = M$. The source position is given by $\bar{\Psi}$. The image positions are given by equation 5.20 (Seager 2010).

$$\bar{z} = \bar{\Psi} + \frac{m_1}{z - z_1} + \frac{m_2}{z - z_2} \tag{5.20}$$

The amplification due to this lensing system is given by the ratio of the total area of the images to the total area of the source. Finding the amplification at each time is given by the following process (Bozza 2010a):

1. Find the roots of the polynomial given by the lensing equation 5.20.

2. Determine the boundaries of the images given the critical curves. The Jacobian of the lensing equation is used to determine the boundaries.

3. Find the area of all the images bounded by the critical curves.

4. Total amplification is given by equation 5.21.

$$A = \frac{A_I}{A_S} \tag{5.21}$$

where A is the amplification value, A_I is the total area of all the images produced due the lensing, and A_S is the area of source star.

For an error, ϵ, in the amplification, that is, $\tilde{A} = A \pm \epsilon$ we can say either $\tilde{A}_I = A_I \pm \delta_1$ or $\tilde{A}_S = A_S \pm \delta_2$. The area of the source star is determined by the source star radius, ρ, mass ratio, q, and the separation between the two lenses, s. Amplification as a function of time is dependent on the trajectory angle, α. The solution to this polynomial of 5th order contains either 3 or 5 images formed. To determine the total area of the 3 or 5 images, Green's theorem is used (Bozza 2010a). The magnification is given by the relative motion of the source star and lensing system.

In this work we examine single and binary lens caustics. A single lens event will have a caustic as a point. Hence the observed light curve should have a single peak as it approaches the caustic. Binary lens caustics are more complicated and can be characterized by three different categories- Close, Intermediate, and Wide. The three categories are divided based on the combination of the mass ratio and the separation between the two lensing masses(Seager 2010). Binary sources as well as binary lenses could cause two peaks as depicted in our simulated light curves (Section 5.5). However, when generating light curves, we focus on the magnification due to binary lensing. Thus, a generalization of our CS results would be applicable for binary sources as well. Caustic curves represent closed loci where the magnification of a point source goes to infinity. Change in magnification as a function of time, depends on

1. ρ: source star radius

2. α: trajectory angle

3. q: ratio of the mass of the two lensing bodies

4. s: distance between the two lensing bodies

For a given q value, the topography changes to one, two, or three caustic curves based on the value of s. In terms of the magnification curve, the change in the number of caustics can result in different light curve signatures as the source crosses the caustic.

Mass ratio, q, and separation parameter, s, have a direct effect on the caustic topography generated. In this work, we focus on the error caused due to small changes, δ and ϵ, in q and s, respectively.

We show the error sensitivity for $\delta = 0.1q$ and $\epsilon = 0.1s$. In order to study error sensitivity, we choose points on the topography map in (Tsapras 2018) well within each region, so that the change in the parameter does not result in a change in caustic topography. The architecture is implemented in the following manner:

1. Obtain CS based measurements, y_o, for a spatial image.

   CS can be applied by projecting a matrix, A, onto the region of interest, x_o. This can be done on a column-by-column basis for a $n \times n$ spatial region, x_o. Thus, for 2D images, y_0 and A are of size $m \times n$, where $m << n$.

2. Given A and a clean reference image, x_r, construct measurements matrix y_r, where $y_r = Ax_r$.

3. Apply a 2D differencing algorithm on y_o and y_r to obtain a differenced image, y_{diff}, and the corresponding convolution kernel, M, which is used to match the observed and reference CS measurement vectors, y_o and y_r (Bramich 2008). In our modelling, we use $y_{\text{diff}} = y_o - y_r$, by using the assumption that the PSF of the reference and observed image is the same as discussed in Section 5.4.2.

4. Reconstruct the differenced image, x'_{diff} using CS reconstruction algorithms, given A and y_{diff}.

5.4.2 Assumptions in our Model

To understand merely the effects of Compressive Sensing on photometric measurements, we eliminate the following variables in our simulations. In future work, we will incorporate each of these factors in one at a time to thoroughly understand the effect of each one in our CS based framework. The two assumptions we make are:

1.) The PSF of the reference image and the observed image is the same. This would typically be the case for space-borne observatories in which the PSF changes very slowly, if at all. The two images differ in any magnification of a star source due to a transient event.

In applications where the PSF of the reference and observed images are different, equation 5.23 is used.

$$y_{\text{diff}} = Ax_o - (Ax_r \star M) \tag{5.22}$$

$$= y_o - (y_r \star M) \tag{5.23}$$

However, in our models, for simplicity, we assume the same PSF for a reference and observed image, thus resulting in equation 5.26.

$$y_{\text{diff}} = A(x_{\text{diff}}) \tag{5.24}$$

$$= A(x_o) - A(x_r) \tag{5.25}$$

$$= y_o - y_r \tag{5.26}$$

Hence, in Figure 4.5, image differencing consists of subtracting the reference measurements from the observed measurements. In non-ideal cases, when the PSF of the reference image is different as compared to the observed image, image differencing algorithms can be added. However, that adds another layer of uncertainty and error, which we needed to eliminate for our purpose of understanding purely the effects of compressive sensing acquisition and reconstruction.

2.) There is no noise present.

To eliminate added complexity in this preliminary study, we do not incorporate any noise. In future studies, we will add in detector noise, measurement noise, as well as any background noise.

For a practical approach, we can assume the effects of noise to be minimal if the SNR during a magnification event for the specific group of pixels representing the microlensing star is sufficiently high, such that, the sparsity content of the image is preserved. In section 5.5, we briefly show the basic effect of CS reconstruction for degrading SNR for an image with Gaussian added noise.

5.4.3 Simulation Setup Parameters

In our simulations, we use a 128×128 size image. In order to depict a crowded stellar field, we generate the number of star sources to be 75% of the total number

of pixels. To simulate realistic fields, we use Airy shaped PSFs with varying radius and flux of the star sources. The radius ranges from $[0, 5]$ pixel units and flux ranges from $[50, 5000]$ pixel counts. We perform 100 Monte Carlo simulations for each set of parameter values discussed later in this section. For each of the 100 Monte Carlo simulations, the crowded stellar field is changed, including the PSF radius and flux values of each star source generated. In addition, for each of the simulation, the Bernoulli random values in A are changed. We use Orthogonal Matching Pursuit algorithm, as provided by Python libraries, for reconstruction.

Compressive Sensing Parameters

For a $n{\times}n$ size spatial image, we use a measurement matrix, A, of size $m{\times}n$ to obtain the measurements, y, of size $m{\times}n$. Hence, our compression factor is $\dfrac{m}{n}$.

For both single lens and binary lens event simulations, we use the following CS parameters.

- Number of measurements, $m = 25\%$ of n

- Measurement matrix, A, consists of Bernoulli random variables of values 1 and 0. These values were chosen such that the matrix can be relevant for practical application.

Gravitational Microlensing Parameters

We simulate microlensing events for single lens and binary lens systems.

1. Single Microlensing events

   For single lens systems we use the following parameters and for each of the simulation cases, u_0 and t_0 are varied in the simulation setup. The other parameters from equation 7.24 are shown in Table 5.10.

Parameter	Value
u_0	0.01, 0.1, 0.5
t_0	13, 15, 17
t_e	30

Table 5.10: Single microlensing event equation parameters used for CS simulation modelling

2. Binary Microlensing events

   For binary microlensing events, we perform simulations for each of the three topographies with the parameter list shown below.

Parameter	Close	Intermediate	Wide
s	0.6	1	1.7
q	1	0.1	0.01
ρ	0.01	0.01	0.01
α	0.03	0.93	0.03
t_E	100.3	100.3	100.3
t_0	7154	7154	7154
u_0	0.1	0.2	0.3

Table 5.11: Binary microlensing event equation parameters used for CS simulation modelling

The description of parameters show in Table 5.11 is given below:

1) s: separation between the two masses in the lensing system in units of total angular Einstein radii

2) q: Mass ratio of the two lenses

3) ρ: Source radius in units of Einstein's ring raidus

4) α Trajectory angle between lens axis and source

5) t_E: Einstein ring radius crossing time

6) t_0: Time of peak magnification

7) u_0: Impact parameter in units of Einstein's ring radius

Error Calculations

We calculate % error based on total flux of the microlensing star in a 3 pixel unit radius from the center pixel of the star. Error is calculated using

$$\frac{|f'_{\text{diff}} - f_{\text{diff}}|}{f_{\text{diff}}} \times 100\% \tag{5.27}$$

where f'_{diff} and f_{diff} are the total fluxes within the 3-pixel radius of the source positions of the reconstructed and original differenced images, respectively.

5.5 Simulation Results

5.5.1 Single Lens Events

In these first set of simulations, we vary u_0, while keeping $t_0 = 15$ and $t_e = 30$ constant.

Amplification for single lens microlensing events are generated using equation 7.24. We compare the CS reconstruction with error due to a γ change in θ_E as described in equation 5.18, where $\gamma = 1 \pm 0.1$. Hence $\theta_E = 0.9\theta_E$ and $\theta_E = 1.1\theta_E$.
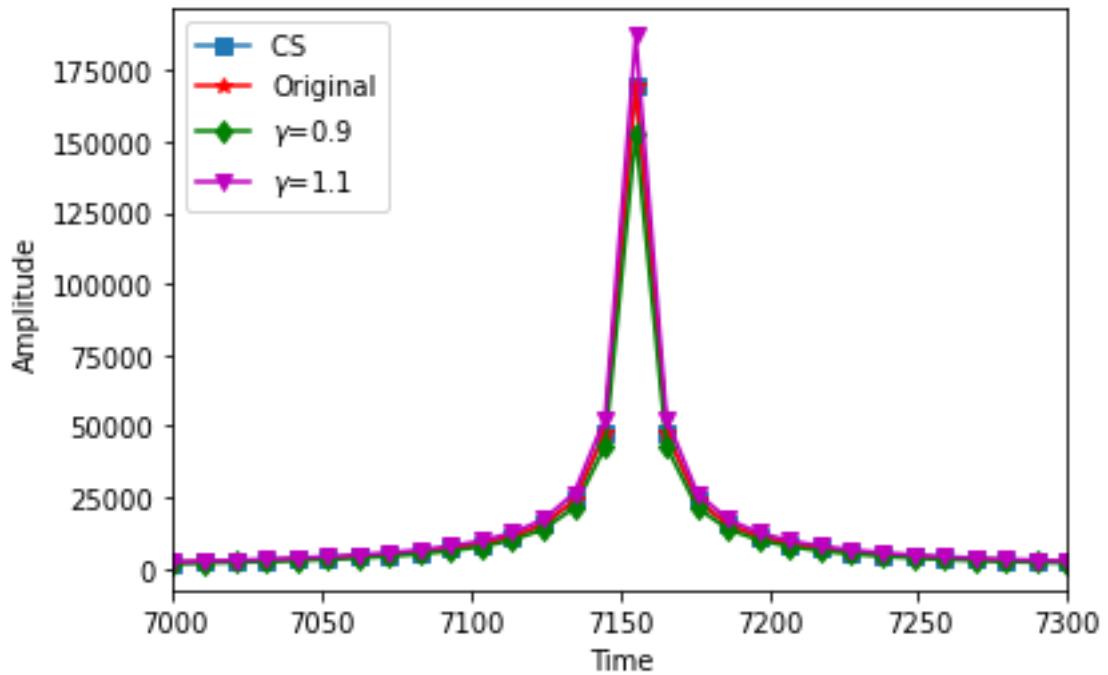
FIG. 5.13: Single Lens microlensing event, $u_0 = 0.01$.

The original simulated microlensing curve along with the CS reconstruction, and the microlensing curve generated due to a change γ in θ_E is shown
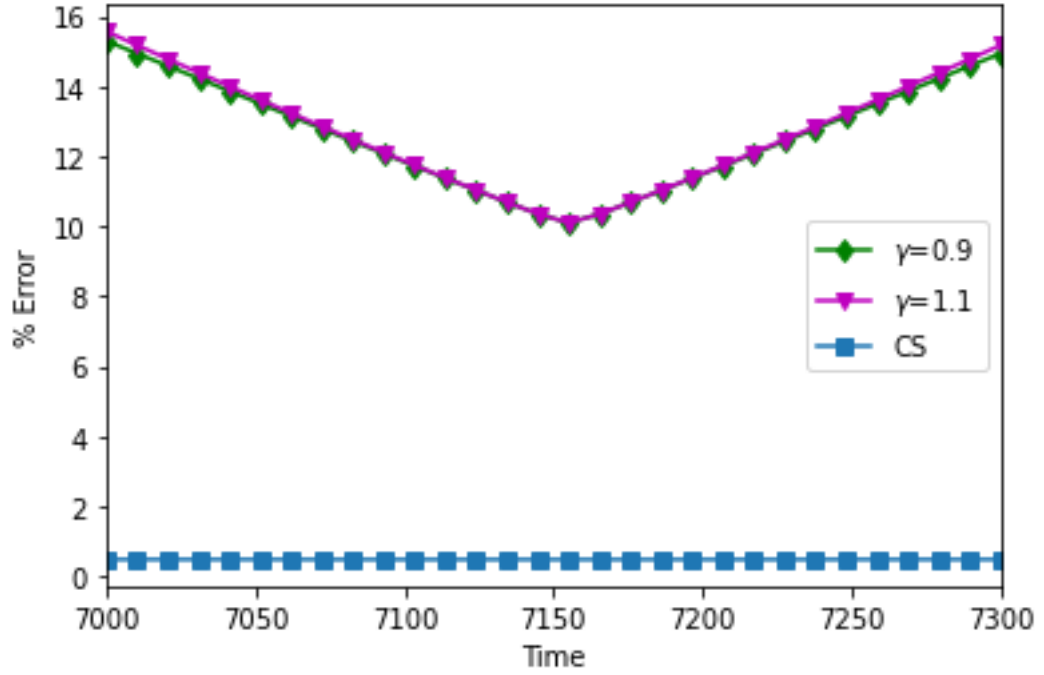
FIG. 5.14: % Errors for Single Lens event, $u_0 = 0.01$ for CS reconstruction and the change in microlensing light curve generated due to γ changes in θ_E as compared to the original simulated microlensing curve for the light curves in Figure 5.13

Single lens event with $u_0 = 0.01$	Average % error	Average standard deviation
CS	0.49	0.00
$\gamma = 0.9$	12.62	1.53
$\gamma = 1.1$	12.71	1.61

Table 5.12: Errors for single microlensing light curve with $u_0 = 0.01$
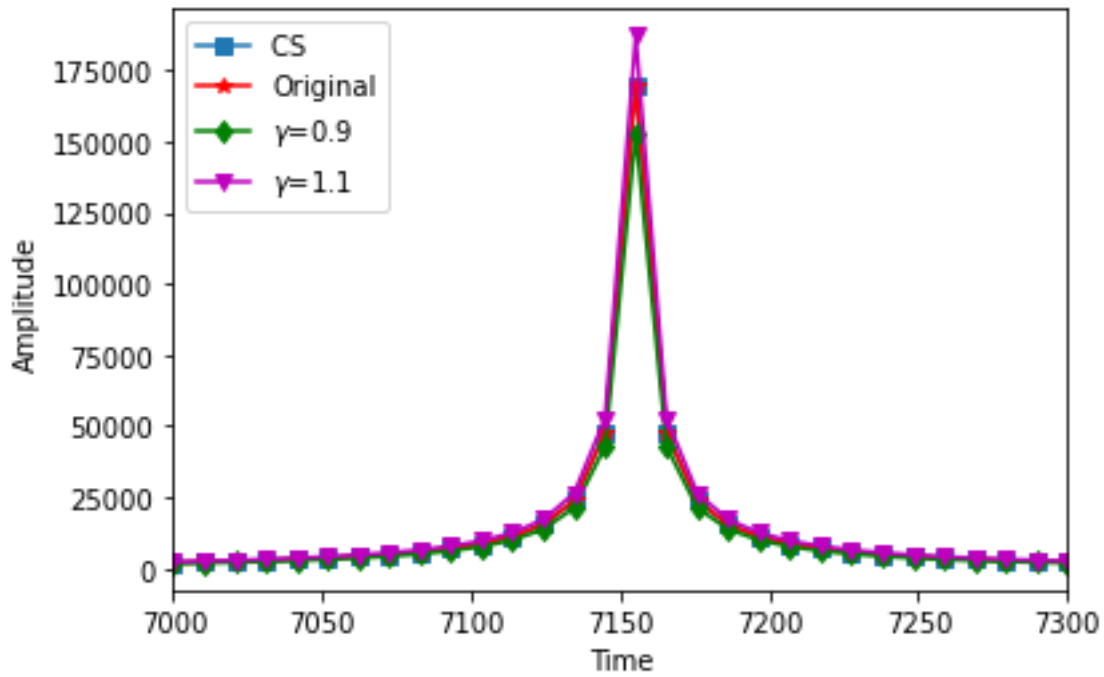
FIG. 5.15: Single Lens microlensing event, $u_0 = 0.1$.

The original simulated microlensing curve along with the CS reconstruction, and the microlensing curve generated due to a change in γ in θ_E is shown
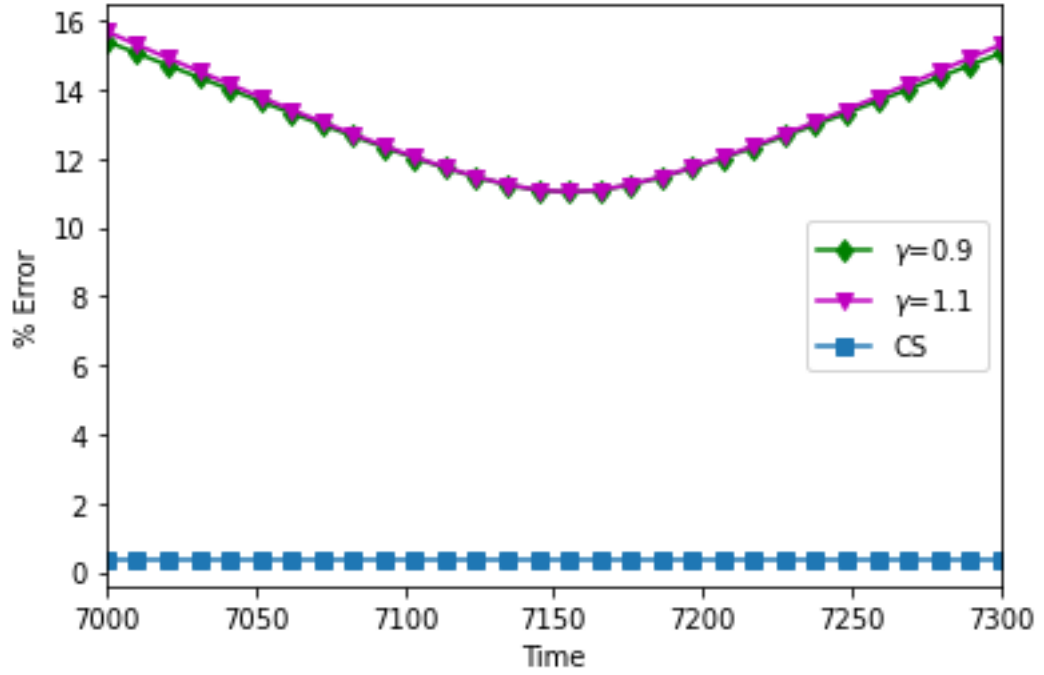
FIG. 5.16: % Errors for Single Lens event, $u_0 = 0.1$ for CS reconstruction and the change in microlensing light curve generated due to γ changes in θ_E as compared to the original simulated microlensing curve for the light curves in Figure 5.15

Single lens event with $u_0 = 0.1$	Average % error	Average standard deviation
CS	0.36	0.00
$\gamma = 0.9$	12.91	1.36
$\gamma = 1.1$	13.01	1.43

Table 5.13: Errors for single microlensing light curve with $u_0 = 0.1$
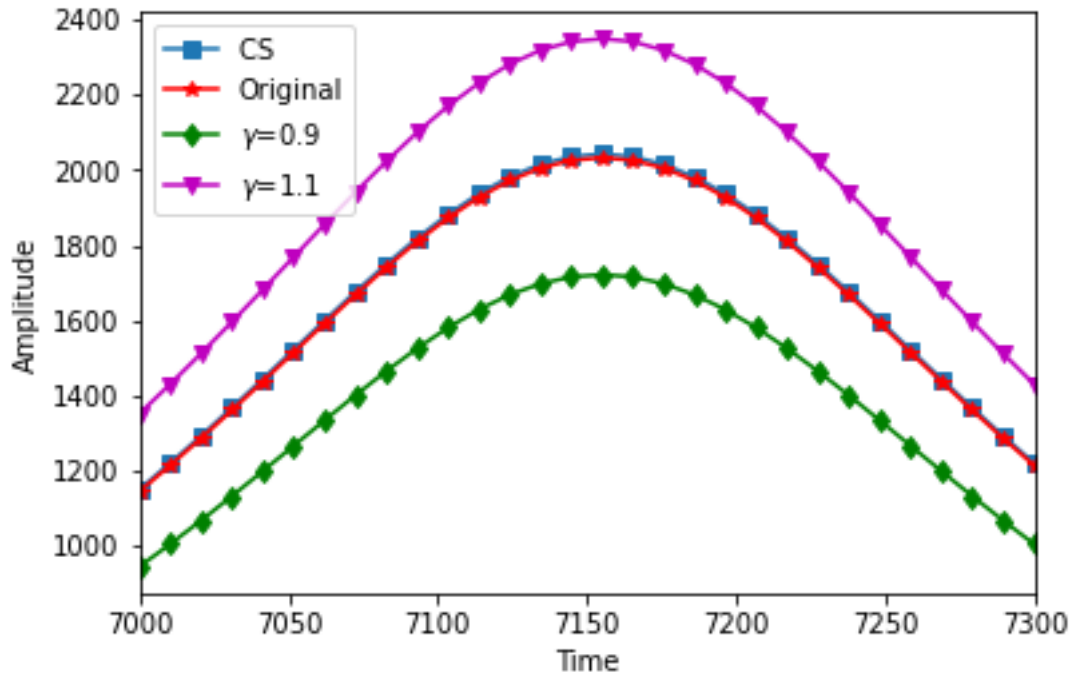
FIG. 5.17: Single Lens microlensing event, $u_0 = 0.5$.

The original simulated microlensing curve along with the CS reconstruction, and the microlensing curve generated due to a change in γ in θ_E is shown
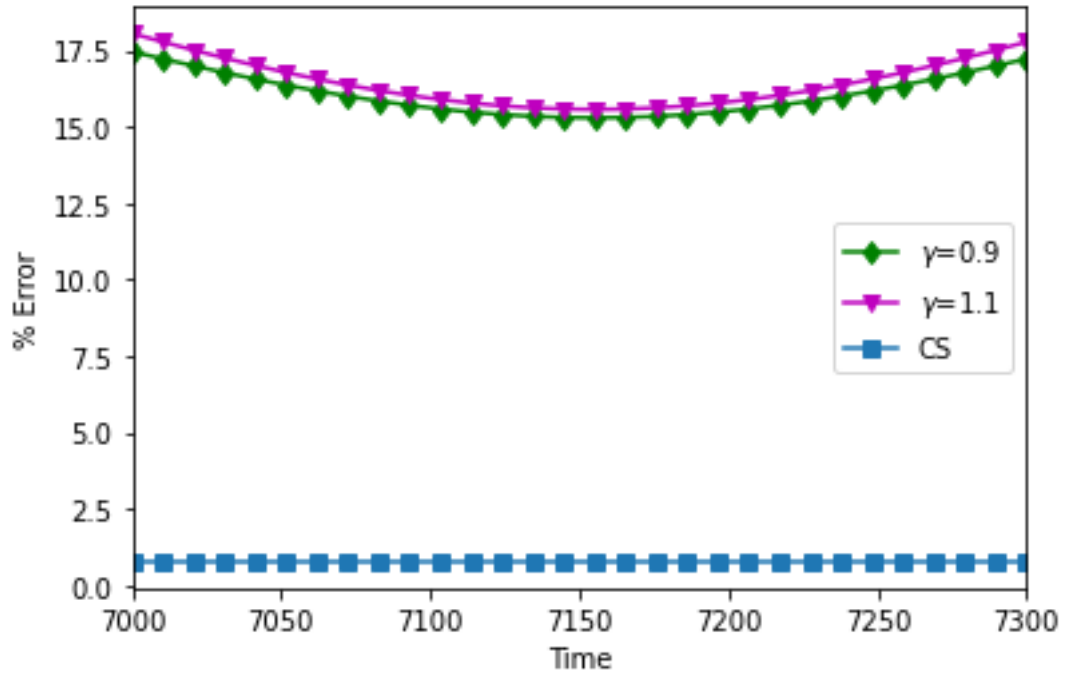
FIG. 5.18: % Errors for Single Lens event, $u_0 = 0.5$ for CS reconstruction and the change in microlensing light curve generated due to γ changes in θ_E as compared to the original simulated microlensing curve for the light curves in Figure 5.17

Single lens event with $u_0 = 0.5$	Average % error	Average standard deviation
CS	0.77	0.00
$\gamma = 0.9$	16.07	0.66
$\gamma = 1.1$	16.45	0.76

Table 5.14: Errors for single microlensing light curve with $u_0 = 0.5$

In the next set of simulations, we use $u_0 = 0.1$ and vary t_0 with $t_0 = 13$ and $t_0 = 17$.
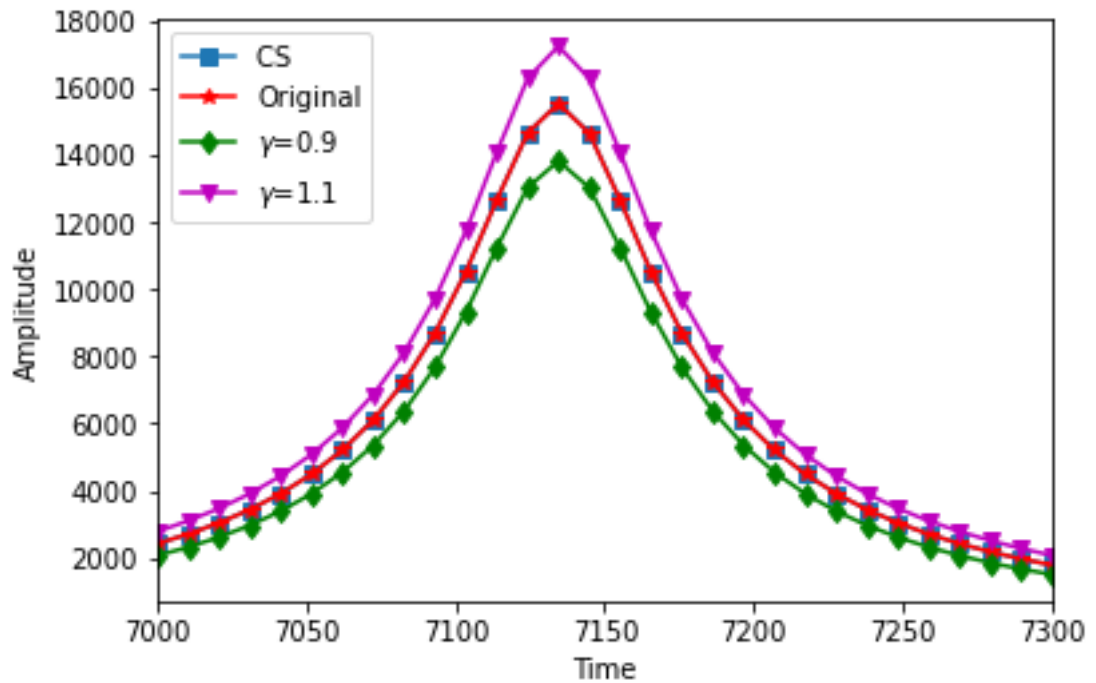
FIG. 5.19: Single Lens microlensing event, $t_0 = 13$.

The original simulated microlensing curve along with the CS reconstruction, and the microlensing curve generated due to a change in γ in θ_E is shown
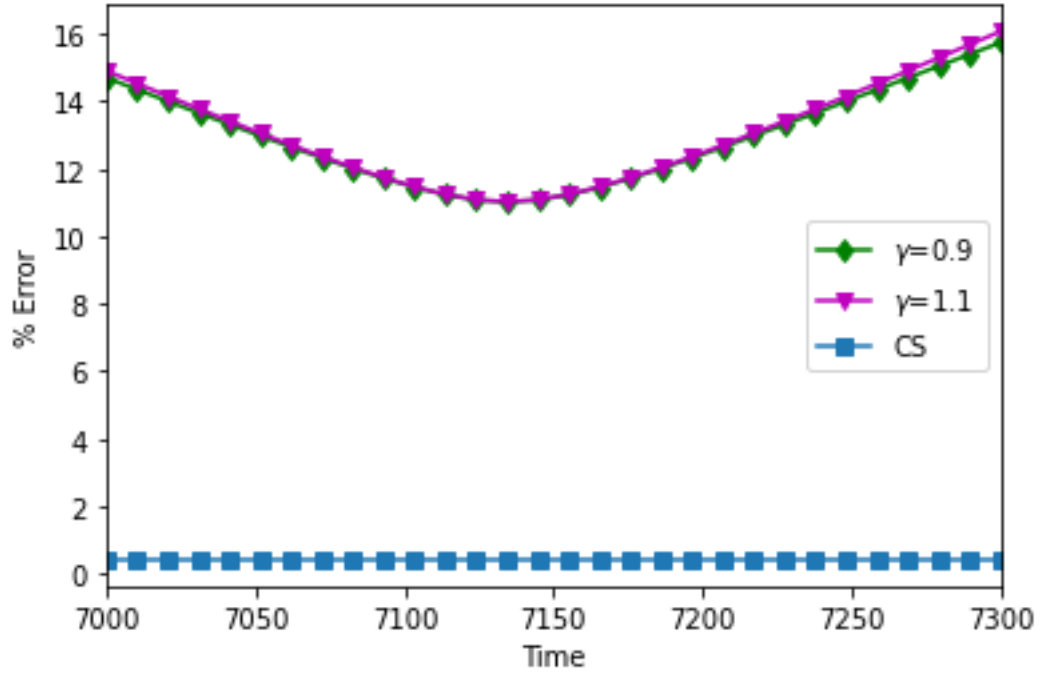
FIG. 5.20: % Errors for Single Lens event, $t_0 = 13$ for CS reconstruction and the change in microlensing light curve generated due to γ changes in θ_E as compared to the original simulated microlensing curve for the light curves in Figure 5.19

Single lens event with $t_0 = 13$	Average % error	Average standard deviation
CS	0.42	0.00
$\gamma = 0.9$	12.94	1.40
$\gamma = 1.1$	13.03	1.48

Table 5.15: Errors for single microlensing light curve with $t_0 = 13$
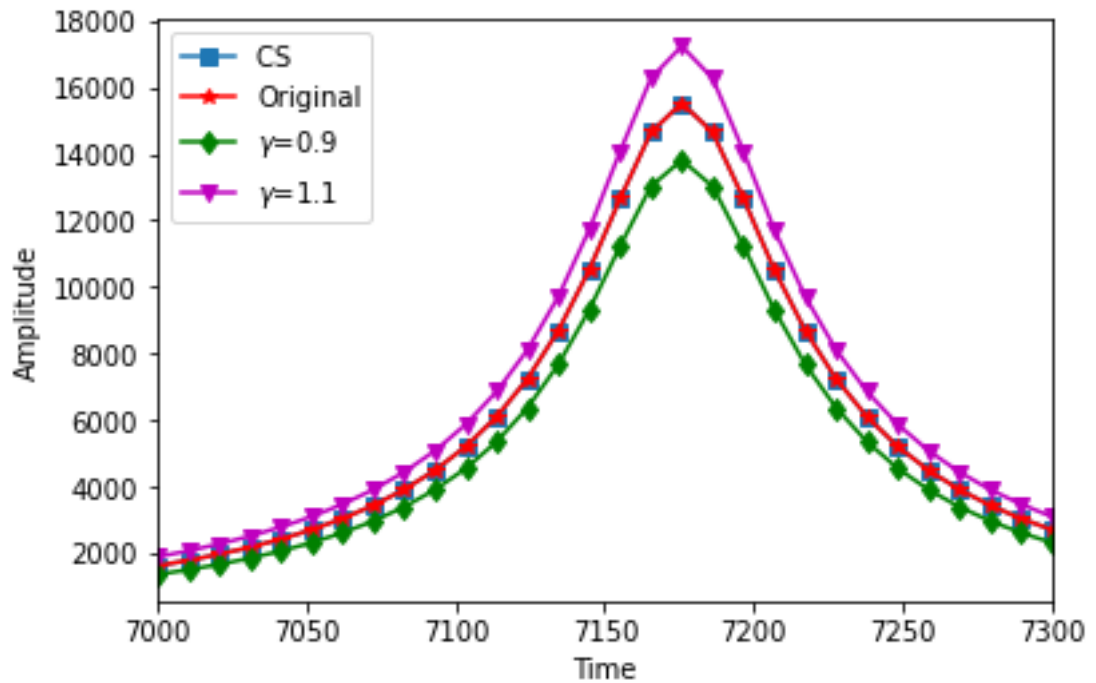
FIG. 5.21: Single Lens microlensing event, $t_0 = 17$.

The original simulated microlensing curve along with the CS reconstruction, and the microlensing curve generated due to a change in γ in θ_E is shown
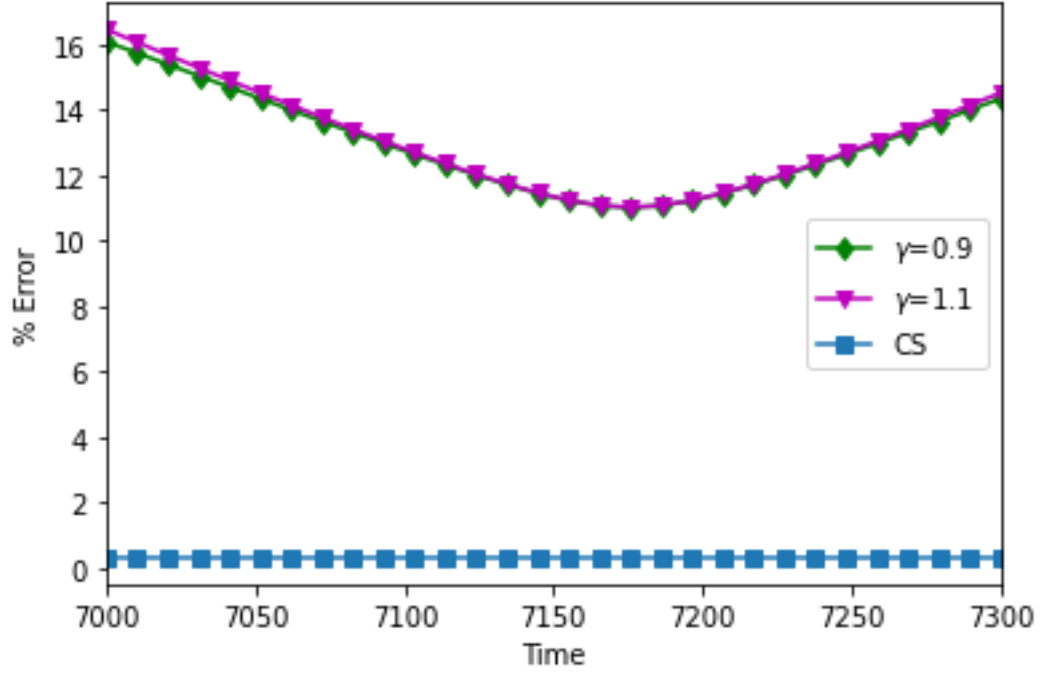
FIG. 5.22: % Errors for Single Lens event, $t_0 = 17$ for CS reconstruction and the change in microlensing light curve generated due to γ changes in θ_E as compared to the original simulated microlensing curve for the light curves in Figure 5.21

Single lens event with $t_0 = 17$	Average % error	Average standard deviation
CS	0.32	0.00
$\gamma = 0.9$	12.98	1.48
$\gamma = 1.1$	13.09	1.57

Table 5.16: Errors for single microlensing light curve with $t_0 = 17$

Our simulations show that CS reconstruction is affected by the magnification value of the source star in each differenced image. For low magnification events, such as the one caused by $u_0 = 0.5$, the error in CS reconstruction is higher. The results in

(Korde-Patel, Barry, & Mohsenin 2020) also indicate that CS reconstruction accuracy is dependent on the magnification of the event, which in turn affects the sparsity of the data set. For low magnification star in a differenced image, the rate of decay of the coefficients in the differenced images also decreases, hence, causing a higher error in CS reconstruction. The small fluctuations in the average error are due to the variation in Bernoulli random measurement matrix. From the error plots (5.16, 5.18, 5.14), we see that CS error is fairly constant, with little variability, over the microlensing curves for all u_0 and t_0 values.

Error Sensitivity of Microlensing Parameters In this section, we fit the differenced magnification curve and the CS reconstructed curve to obtain the microlensing parameters: F_s, F_b, t_0, t_E, u_0. The differenced magnification curve is obtained from x_{diff} at the microlnesing star source center pixel, $[p_x, p_y]$ and CS reconstructed magnification curve is obtained from $x'_{diff}[p_x, p_y]$. We use the same setup as in Section 5.4.3. We obtain the parameters for each CS reconstructed data set over the 100 Monte Carlo simulations and present the average derived value in Table 5.18. We used Mulens Model software for obtaining the parameters(Poleski & Yee 2019). When we generated our magnification light curves, we used $F_b = 0$. However, due to the observed and reference image differencing, and the Mulens Model software modelling factors, we obtain a non-zero F_b during parameter fitting. Thus, in order to accurately understand the effect of CS reconstruction on the derivation of the parameters, we compare the Mulens Model software derived parameters for $x_{diff}[p_x, p_y]$ with $x'_{diff}[p_x, p_y]$. The obtained results of the parameters depend on the initial guess provided. Hence, in our analysis, we vary the initial guess to determine the effects of CS, despite of the initial guess values. Our true values are listed below:

- $t_0 = 15$

- $t_E = 30$

- $u_0 = 0.5$

We use the initial values as shown in Table 5.17.

Trial Number	t_0	t_E	u_0
1	15	30	0.5
2	15	30	0.4
3	13	30	0.5
4	15	32	0.5

Table 5.17: Microlensing Parameters used as initial guess for Mulens Model Software

For each trial, we show the % error in the parameters derived from Mulens Model software between $x_{diff}[p_x, p_y]$ and $x'_{diff}[p_x, p_y]$ in Table 5.18

Trial Number	F_s	F_b	t_0	t_E	u_0
1	0.585	0.585	0.00	0.025	0.029
2	0.585	0.585	0.00	0.025	0.029
3	0.586	0.586	0.00	0.025	0.029
4	0.585	0.585	0.00	0.025	0.029

Table 5.18: Derived Parameter % Errors

In all the different initialization parameters, there was a very insignificant difference in the % error for all of the parameters. The largest % error was in F_s and

104

F_b. Hence, through this setup, we can say that F_s and F_b are most affected by CS reconstruction. In order to visually understand the effect of CS reconstruction on F_s, we simulate a star field and run CS reconstruction for 100 Monte Carlo simulation by varying the Bernoulli random matrix each time. Figure 5.23 shows the flux variation caused due to the CS measurement matrix, for a given star field with a source star experiencing a single lens microlensing event with $\mu_0 = 0.5$. Similar to our other simulations, 25% CS measurements were used.
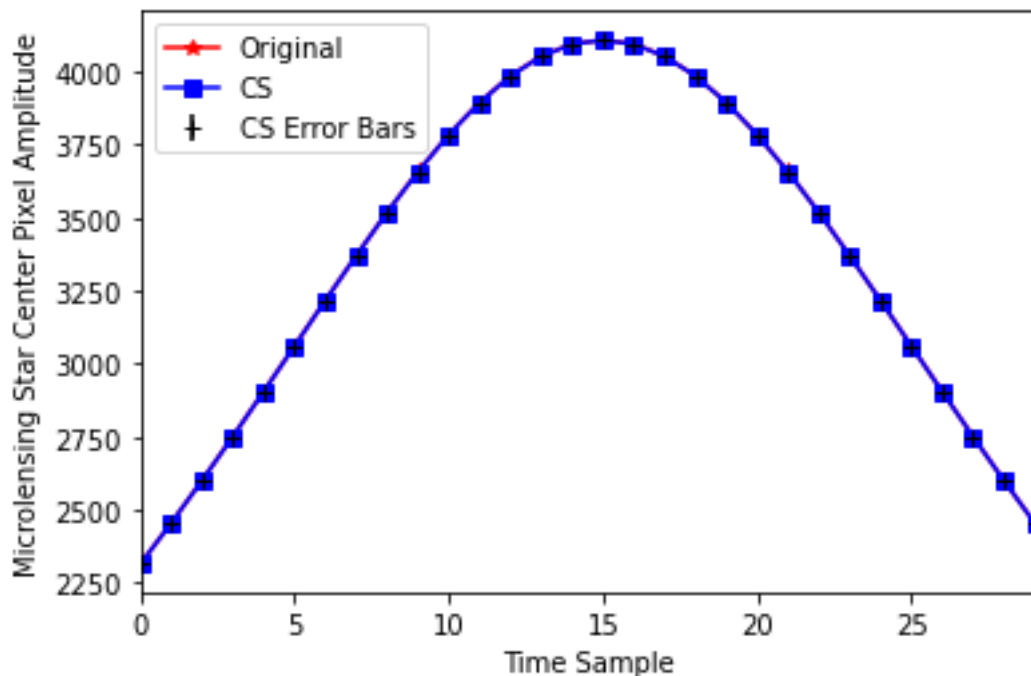
FIG. 5.23: Single lens microlensing event CS reconstruction with error bars

Figure 5.24 and 5.25 show detailed plots for some of the statistics for the data in Figure 5.23.
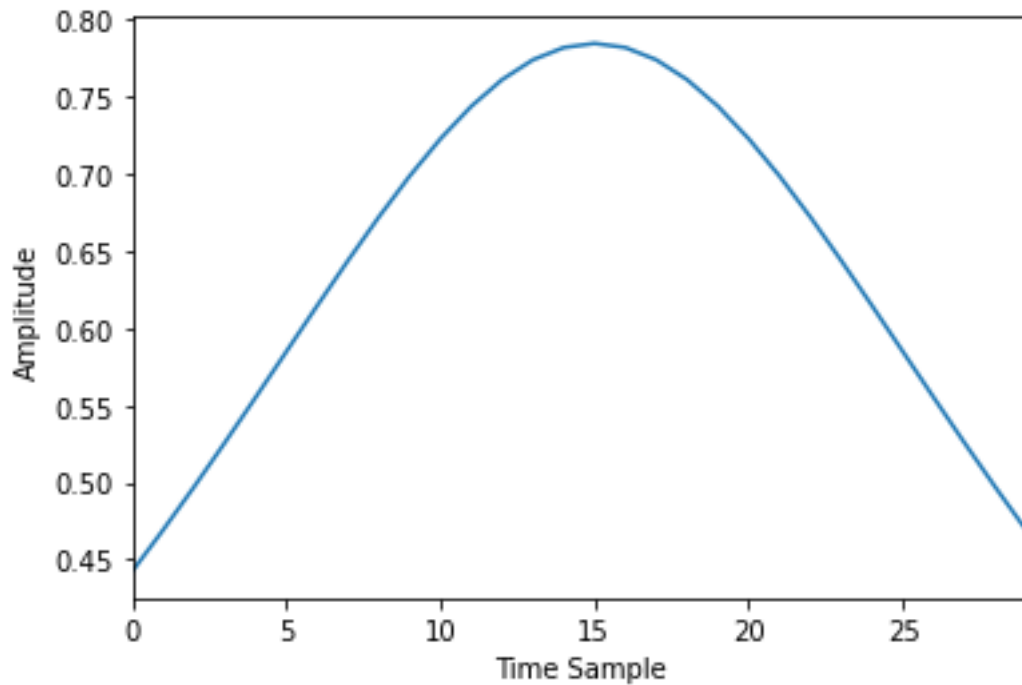
FIG. 5.24: Difference in amplitude between the original microlensing curve and average CS reconstruction microlensing curve for the data in Figure 5.23

For the data in Figure 5.23, we explicitly show the standard deviation of the CS reconstruction curve over 100 Monte Carlo simulations for each time sample in Figure 5.25.
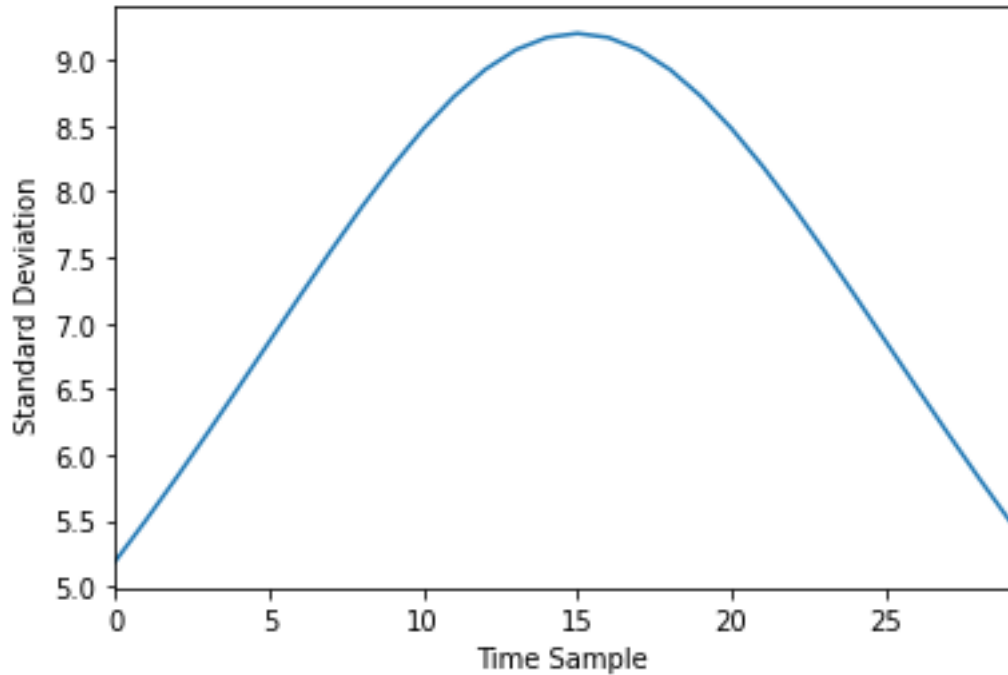
Fig. 5.25: Standard deviation of the CS reconstruction pixel values over 100 Monte Carlo simulations for each time sample for the data in Figure 5.23

As noted in Figure 5.24 and 5.25, the variation in CS reconstruction, as calculated by the difference in pixel amplitude and the standard deviation, changes as a function of the pixel value of the original source star. That is, a smaller standard deviation is seen for time samples where the magnification is lower as compared to the time samples where the pixel magnification is higher.

Noise effects on a Single Lens Microlensing Event Curve   In this section, we briefly show the effect of Gaussian noise on the reconstruction of the microlensing event curves. From CS theory, it is known that the signal of interest is accurately reconstructed for sparse signals. Hence, adding noise to the spatial images can degrade the sparsity of the images. In our simulations, we add random Gaussian noise with

107

mean = 0, and varying standard deviation to obtain images with different SNRs. CS architecture shown in Figure 4.5 is applied, with the noise application on the observed image, x_o. In the noise simulation, 25% CS measurements were used.
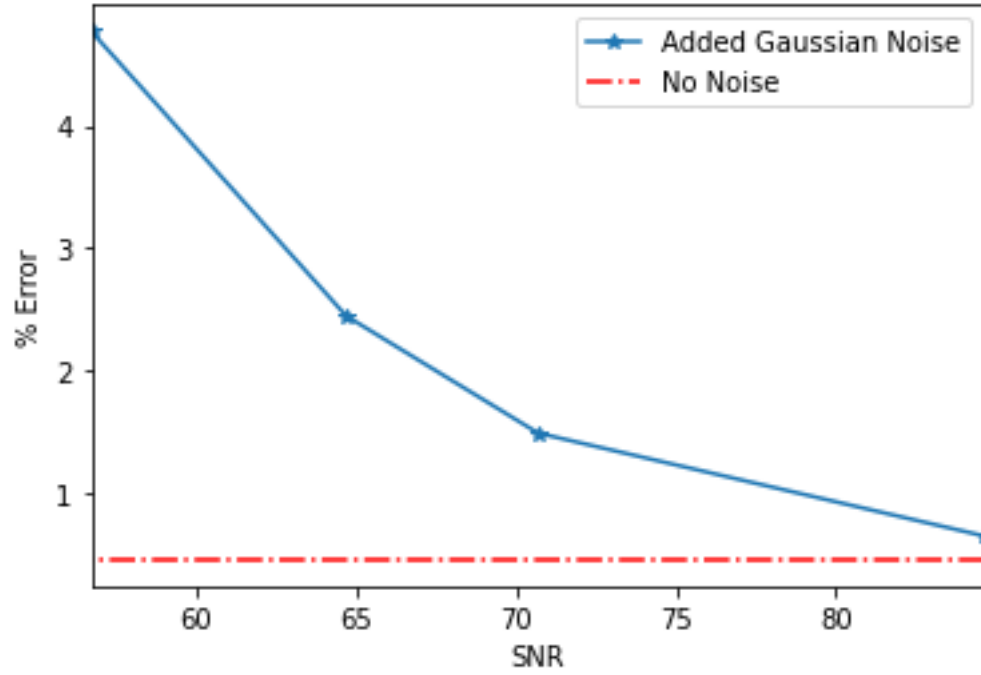
FIG. 5.26: % error as a function of image SNR. Images are generated by varying added Gaussian noise. The dashed red line represents % error without any addition of noise

From Figure 5.26, it is evident that as the SNR decreases, the % of error increases at a higher rate. The rate of increase is 0.06 % error per SNR unit towards the higher SNR values and 0.29 % error per SNR unit towards the lower SNR range.

5.5.2 Binary Lens Microlensing Events

The amplification for the photometric curves is derived using gravitational microlensing equations, generated by the software provided in (Bozza 2010b).

We perform simulations on the three categories described in Section 5.4.1 - close, intermediate, and wide. To determine error sensitivity in terms of impact on the separation parameter, s, and mass ratio, q, we compare the CS reconstruction with the following values of s and q, thereby providing CS reconstruction accuracy bounds of 10% for the value of s and q.

Caustic	Original s	$\pm 0.1s$	Original q	$\pm 0.1q$
Close	0.6	0.54, 0.66	1	0.9, 1.1
Intermediate	1	0.9, 1.1	0.1	0.09, 0.11
Wide	1.7	1.53, 1.87	0.01	0.009, 0.011

Table 5.19: Values of s and q chosen for calculating error sensitivity, such that it is within 10% of the value chosen for the original caustic
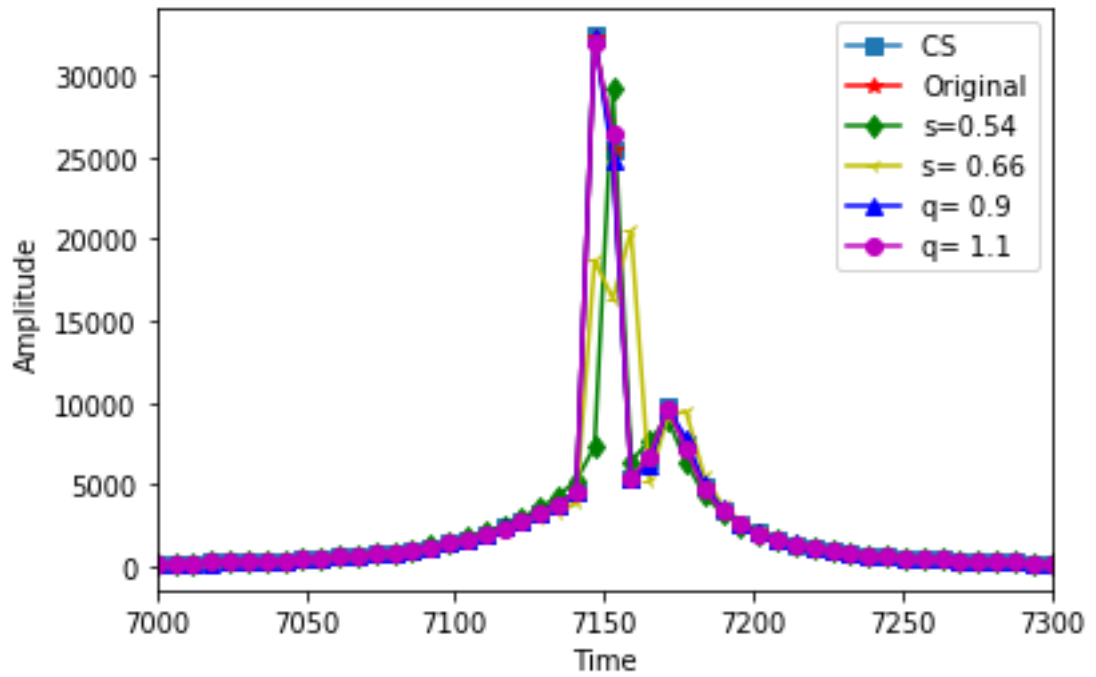
FIG. 5.27: Closed caustic microlensing curve with s = 0.6 and q = 1, shown along with the CS reconstruction, as well as the microlensing curve generated using s= 0.54, 0.66 and q = 0.9, 1.1
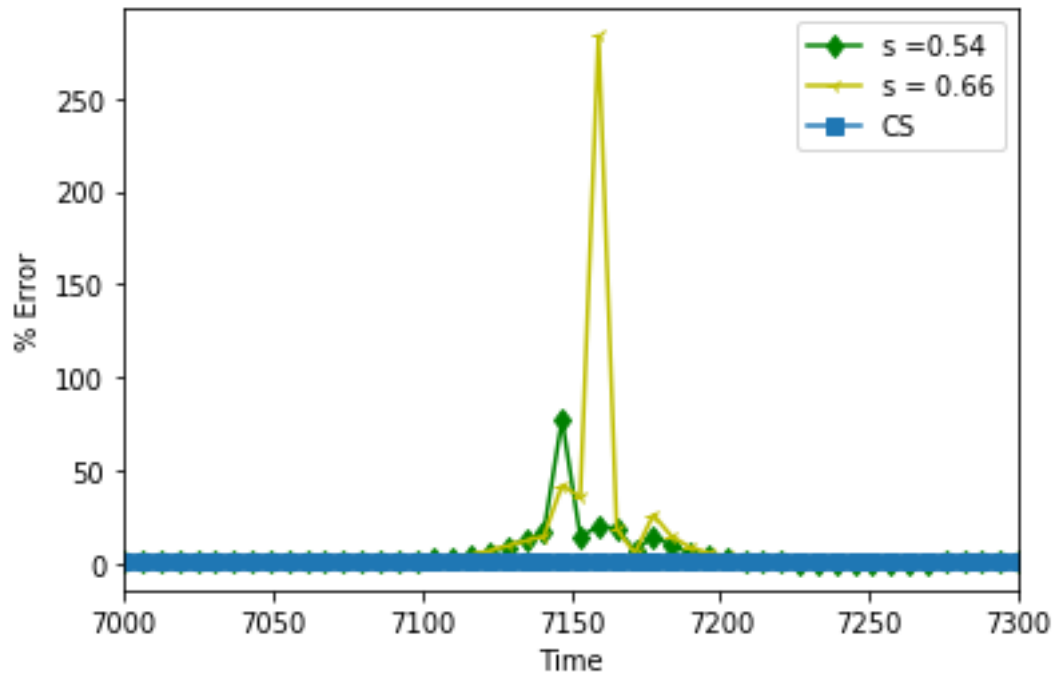
FIG. 5.28: % error of CS reconstruction as compared to % error due to 10% deviation in the value of s.
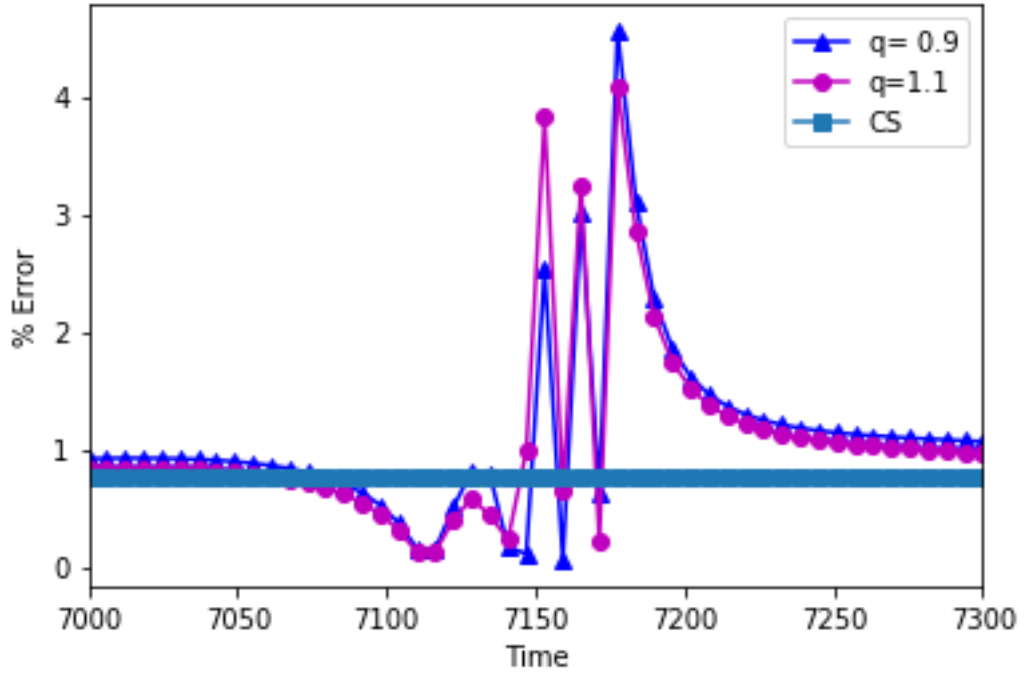
FIG. 5.29: % error of CS reconstruction as compared to % error due to 10% deviation in the value of q

CloseCaustic	Average % Error	Avg Standard deviation of the % error
CS	0.76	0.00
s= 0.54	0.52	11.52
s= 0.66	10.47	40.02
q= 0.9	1.11	0.80
q= 1.1	1.07	0.82

Table 5.20: Errors for close caustic topographies model for CS reconstruction, and for microlensing light curve generated due to 10% variation in s and q

112
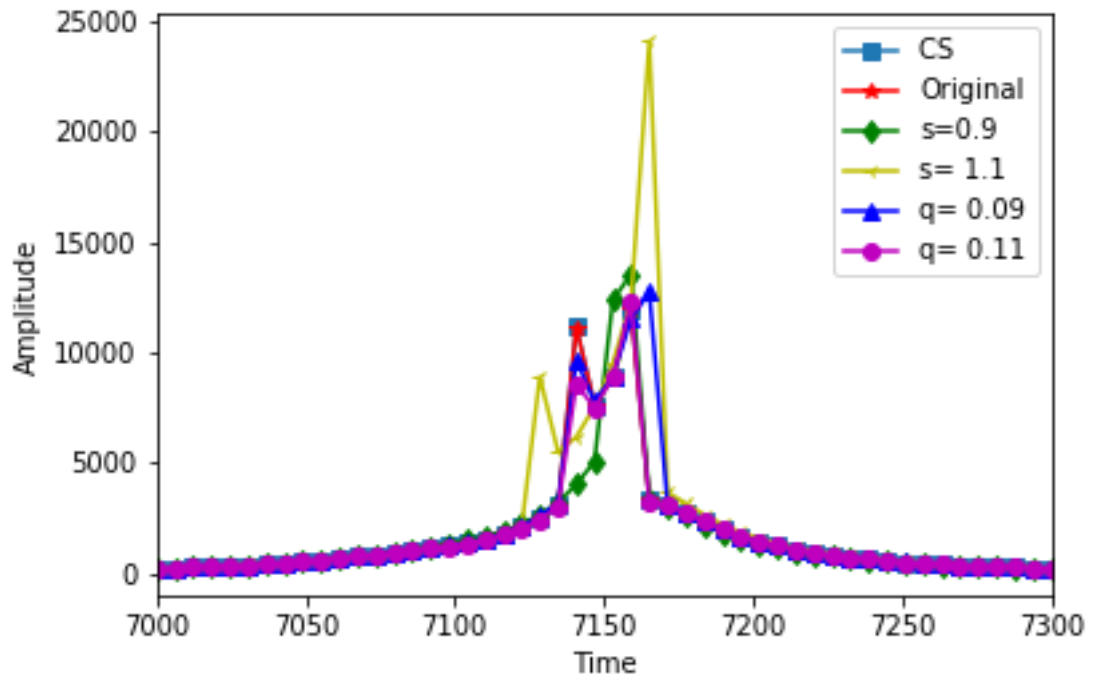
FIG. 5.30: Intermediate caustic microlensing curve with s = 1 and q = 0.1, shown along with the CS reconstruction, as well as the microlensing curve generated using s= 0.9, 1.1 and q = 0.09, 0.11

113
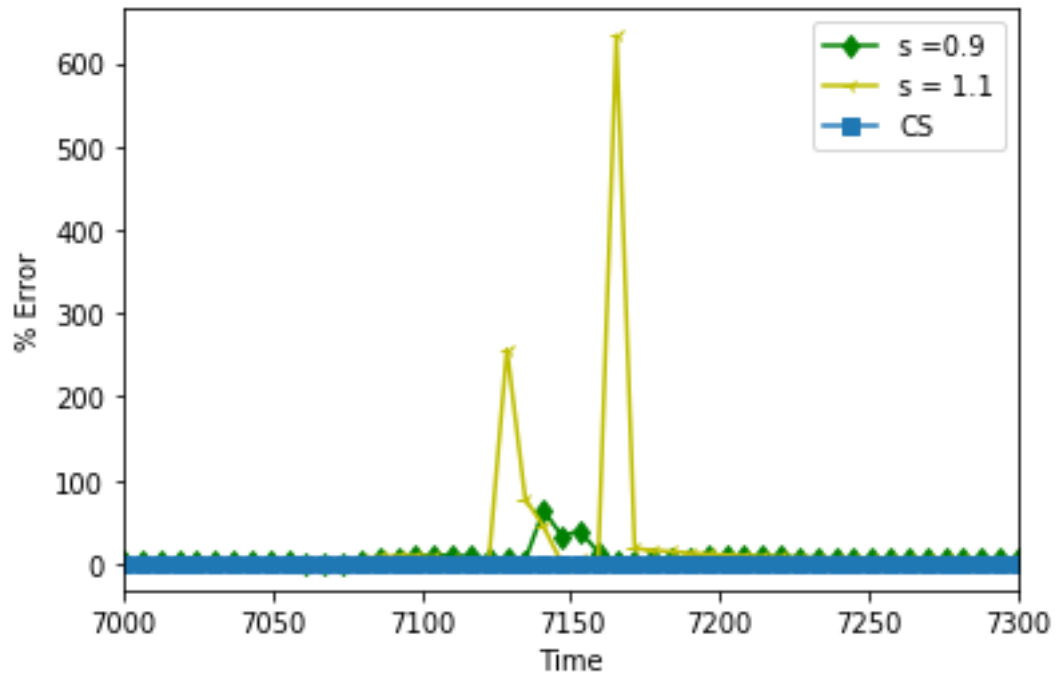
FIG. 5.31: % error of CS reconstruction as compared to % error due to 10% deviation in the value of s for the given (Figure 5.30) intermediate caustic binary lensing light curve reconstruction
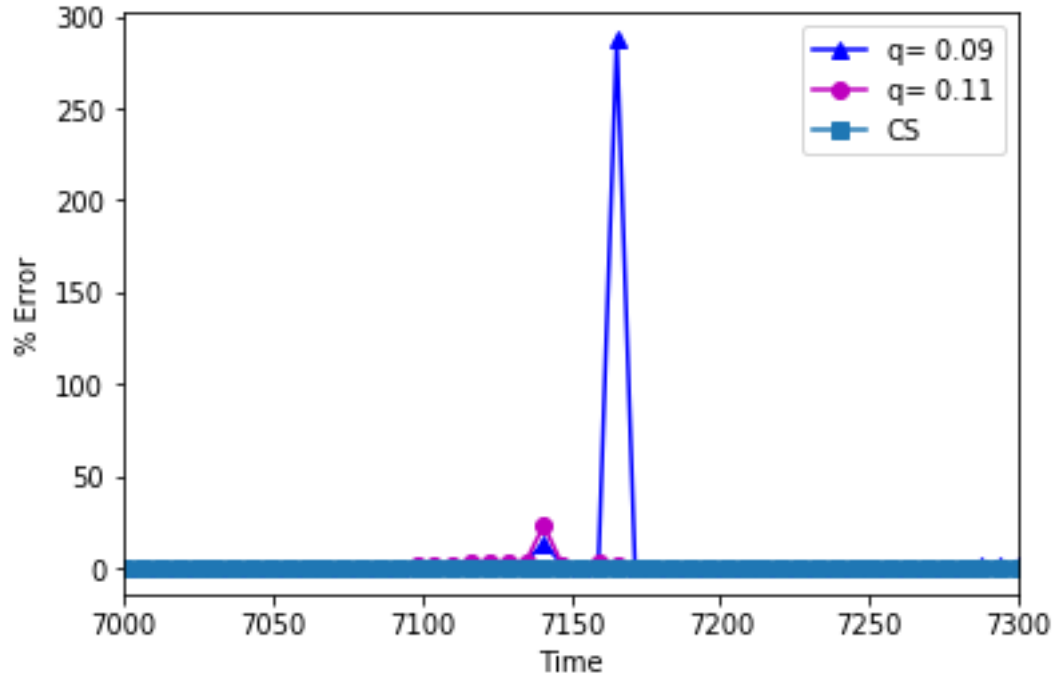
FIG. 5.32: % error of CS reconstruction as compared to % error due to 10% deviation in the value of q for the given (Figure 5.30) intermediate caustic binary lensing light curve reconstruction

Intermediate Caustic	Average % Error	Avg Standard deviation of the % error
CS	0.61	0.00
s= 0.9	7.74	10.45
s= 1.1	25.86	94.24
q= 0.09	6.76	40.14
q= 0.11	1.13	3.23

Table 5.21: Errors for intermediate caustic topographies model for CS reconstruction, and for microlensing light curve generated due to 10% variation in s and q
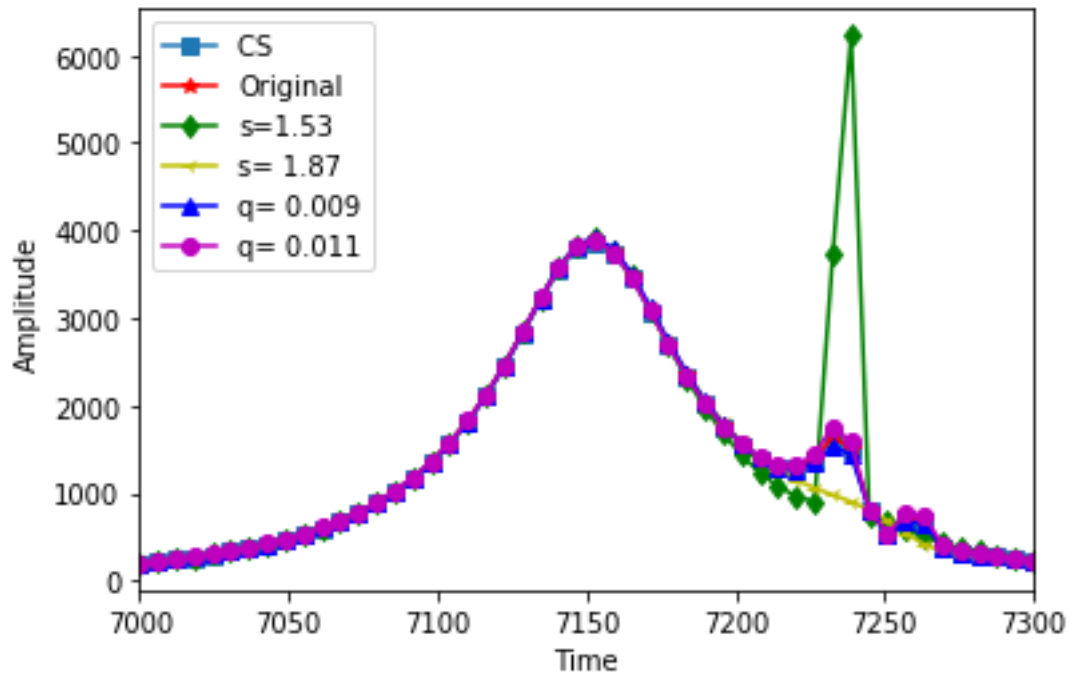
FIG. 5.33: Wide caustic microlensing curve with s = 1.7 and q = 0.01, shown along with the CS reconstruction, as well as the microlensing curve generated using s= 1.53, 1.87 and q = 0.009, 0.011

116
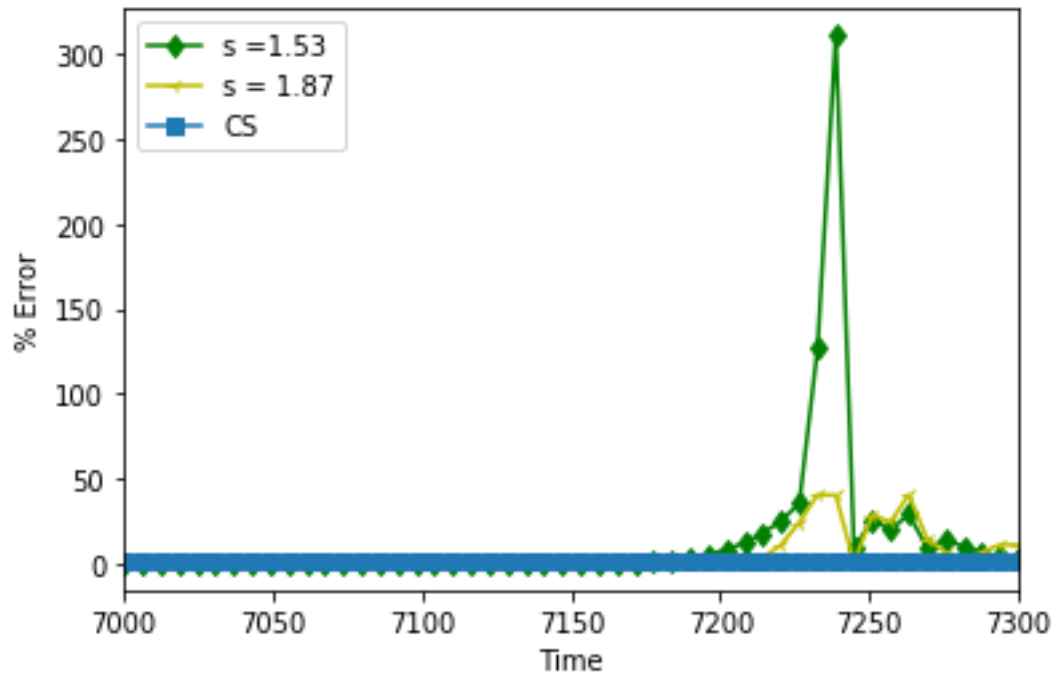
FIG. 5.34: % error of CS reconstruction as compared to % error due to 10% deviation in the value of s for the given (Figure 5.33) wide caustic binary lensing light curve reconstruction
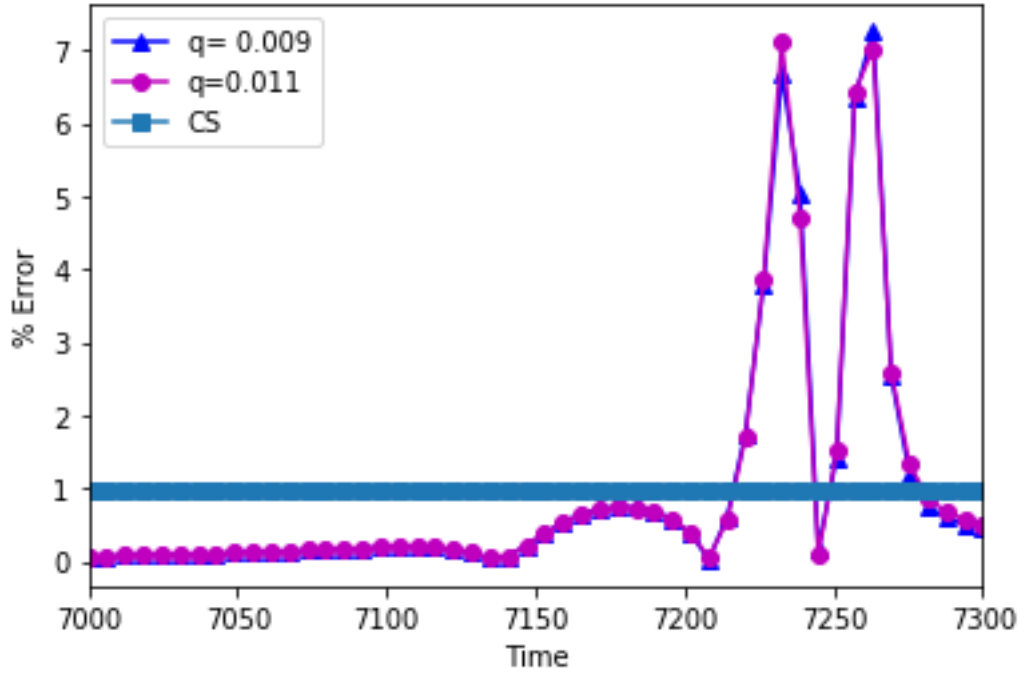
FIG. 5.35: % error of CS reconstruction as compared to % error due to 10% deviation in the value of q for the given (Figure 5.33) wide caustic binary lensing light curve reconstruction

Wide Caustic	Average % Error	Avg Standard deviation of the % error
CS	0.97	0.00
s= 1.53	13.64	46.57
s= 1.87	5.54	11.02
q= 0.009	0.96	1.73
q= 0.011	0.97	1.74

Table 5.22: Errors for wide caustic topographies model for CS reconstruction, and for microlensing light curve generated due to 10% variation in s and q

Our simulations show that we can attain error less than 1% using 25% of the Nyquist rate measurements. In addition, the error obtained through CS reconstruction, will be well within 10% deviation in verified microlensing parameters of θ_E, s and q.

5.6 Conclusions

Using this technique we give limitations on the sensitivity of detection of planetary perturbations given our CS parameters. We show examples of the effects of error tolerance on the science parameters that are of importance in the microlensing curves. For both single and binary microlensed events, we provide examples of the changes in the microlensing parameters due to minimal error tolerance. This gives a bound for analyzing the effects of compressive sensing for the application of gravitational microlensing. These are simulated theoretical error bounds for given sensitivities-the sensitivity of the detectors and technology currently used may not be sensitive to such δ changes in the science parameters. For single lensed microlesning events, we showed the CS reconstruction error as compared to error from $\pm\ 10\%$ in θ_E. Our results show that CS is sensitive to changes in u_0 and not to changes in t_0, as t_0 causes merely a shift in data, while u_0 causes a change in magnification value.Through our analysis for microlensing parameter fitting, we show that CS is most sensitive to F_s and F_b. For binary lensed microlensing events, we show CS reconstruction error as compared to error within $\pm\ 10\%$ of the mass ratio and the separation between the two lenses. Our work shows that we can reconstruct microlensing light curves using 25% of the required Nyquist rate measurements with error less than 1%. In terms of microlensing sensitivity, we show that this error is within the bounds of 10% of θ_E for single microlensed events and within 10% of q and s for binary microlensed

events. In this work we only focus on bounds determined by our simulated models using microlensing theory and disregard detector optics effects. In cases where less sensitivity is affordable, fewer measurements can be used to further save on-board resources. Vice Versa, if more sensitivity to perturbations is required the number of measurements can be increased. This technique works with high accuracy, with less than 1% error for crowded stellar fields with the same PSFs for a reference and observed image.

CS DETECTION OF MICROLENSING PARALLAX

In gravitational lensing, the surface brightness, which is the flux per area, is conserved. The total flux increases or decreases, since the area increases or decreases. In microlensing, distinct images, due to the gravitational effects of the lensing system, are not seen, but rather, magnification or demagnification of the source star is observed; the images are not resolved. Since the Jacobian matrix gives the amount of change in the source star flux in each direction, the transformation of the original source to the stretched source can be mapped by the Jacobian. The absolute value of the inverse of determinant gives the amount of magnification.

Einstein's ring forms when there is an exact alignment of the source, lens and observer and is an important parameter for the basis of gravitational microlensing equations. Einstein's ring radius, θ_E, can be defined by equation 9.34.

$$\theta_E = \sqrt{\frac{4GMD_{LS}}{c^2 D_L D_S}} \tag{6.1}$$

where M is the total mass of the lensing system, D_{LS} is the distance from the lens to the source, D_L is the distance from the observer to the lensing system, and

D_S is the distance from the observer to the source (Seager 2010).

From the formalization from (Gould 2020), rewriting this in terms of relative lens-source parallax, π_{rel}, where $\pi_{rel} = \dfrac{AU D_{LS}}{D_s D_L}$, we get

$$\theta_E = \sqrt{kM\pi_{rel}} \tag{6.2}$$

Here $k = \dfrac{4G}{c^2 AU}$ and AU is 1 astronomical unit or 1.5×10^8 km.

If we define microlensing parallax in terms of the relative lens-source parallax, we obtain $\pi_E = \dfrac{\pi_{rel}}{\theta_E}$ (Yee 2015), (Bachelet, Hinse, & Street 2018),

$$M = \dfrac{\theta_E^2}{k\pi_{rel}} \tag{6.3}$$

$$= \dfrac{\theta_E}{k\pi_E} \tag{6.4}$$

The amplification of a single lensed microlensing event light curve with time dependency is given by equation 7.24 (Seager 2010)

$$A(t) = \dfrac{u_0^2 + \left(\dfrac{t - t_0}{t_E}\right)^2 + 2}{\left[u_0^2 + \left(\dfrac{t - t_0}{t_E}^2\right)\right]^{1/2} \left[u_0^2 + \left(\dfrac{t - t_0}{t_E}\right)^2 + 4\right]^{1/2}} \tag{6.5}$$

The flux at each time sample, t is given by equation 6.6 (Seager 2010).

$$F(t) = F_s A(t) + F_b \tag{6.6}$$

Thus, from a photometric curve, for a single microlensing event, we can obtain the parameters: t_0, t_E, u_0, F_s and F_b from a microlensing photometric curve. All of

the parameters are defined in table 6.1.

Parameter	Definition
t_0	Time of peak magnification
t_E	Einstein ring crossing time: $\dfrac{\theta_E}{\mu_{rel}}$
μ_0	Impact parameter in units of θ_E
F_s	Microlensing source star flux
F_b	Microlensing source star blended flux

Table 6.1: Microlensing Parameter Definitions

In table 6.1, μ_{rel} is the relative lens-source proper motion. Here, obtaining the lens mass remains unresolved, as we have two unknown parameters: θ_E and π_{rel}. In order to break the degeneracy to obtain specific microlensing parameters, measuring the parallax, π_E, offers once such solution(Lee 2017) (Smith, Mao, & Paczyński 2003). If we obtain u_0, we can solve for M, given π_E. According to (Bachelet, Hinse, & Street 2018), microlensing parallax can be measured in three ways:

1. Motion of the Earth around the sun causing an annual parallax

2. Two or more space based observatories, separated by a significant baseline

3. Terrestrial parallax measured using a ground and space based observatory

In our work, we focus on a constellation of a space based observatory to create simultaneous parallax measurements.

We can define the parallel and perpendicular shifts due to a microlensing parallax as in (Bachelet, Hinse, & Street 2018) (Gould 2020). Let us assume **o** as the

vector for the motion of the observatory. In a telescope constellation, from (Bachelet, Hinse, & Street 2018), $\mathbf{o} = <o_1, o_2>$, where:

$$o_1 = \epsilon_{\parallel} cos\Omega \tag{6.7}$$

and

$$o_2 = \epsilon_{\parallel} sin\lambda sin\Omega \tag{6.8}$$

Here $\epsilon = \dfrac{R}{AU}$ and we use $\lambda = \dfrac{\pi}{6}$ in our simulations.

The parallax vector $\pi_E = (\pi_E cos\theta, \pi_E sin\theta)$, where θ is the lens source trajectory angle.

To obtain the shifts due to parallax, we get:

$$\delta_\tau = \pi_E \cdot \mathbf{o} \tag{6.9}$$

$$= \pi_E cos\theta \epsilon_{\parallel} cos\Omega + \pi_E sin\theta \epsilon_{\parallel} sin\lambda sin\Omega \tag{6.10}$$

$$\delta_\beta = \pi_E \times \mathbf{o} \tag{6.11}$$

$$= \pi_E cos\theta \epsilon_{\parallel} sin\lambda sin\Omega - \pi_E sin\theta \epsilon_{\parallel} cos\Omega \tag{6.12}$$

where $\Omega = \dfrac{2\pi}{P}(t - t_0) + \Phi$, P is the orbital period and Φ is the orbital phase relative to t_0 (Bachelet, Hinse, & Street 2018). We use $\theta = \dfrac{\pi}{4}$ in our modelling. From equation 7.24, we can write

$$u(t) = \left[u_0^2 + \tau^2 \right]^{1/2} \tag{6.13}$$

where $\tau = \left(\dfrac{t - t_0}{t_E} \right)$

We can define $\tilde{u}(t)$ as the microlensing equations due to parallax (Bachelet, Hinse, & Street 2018):

$$\tilde{u}(t) = \sqrt{(u_0 + \delta_\beta)^2 + (\tau + \delta_\tau)^2} \tag{6.14}$$

In this manner, we can define the new amplification equation as

$$\tilde{A}(t) = \frac{\tilde{u}(t)^2 + 2}{\tilde{u}(t)\sqrt{\tilde{u}(t)^2 + 4}} \tag{6.15}$$

Thus, from a photometric curve with a microlens parallax, we can obtain $u_0 + \delta_\beta$ and $\tau + \delta_\tau$.

6.1 Simulation Setup

In this section we discuss the microlensing parameters and the CS parameters used for our simulation modelling.

6.1.1 Parallax Measurement Setup

In this section, we show effectiveness of CS over a range of δ_τ and δ_β as described in equations. We vary Φ, the space-flight instrument orbital phase to span over a range of values of δ_τ and δ_β. Our microlensing parallax, π_E is given by equation 6.19. From (Bachelet, Hinse, & Street 2018), we make the same assumptions of the source being located in the galactic bulge at 4kpc and the lens at 8kpc with a relative lens-source speed of 200km/sec to obtain the value of π_E.

Hence, in a simple case, with origin as the center of the satellite trajectories, we

can write

$$\delta_\tau = \pi_E \epsilon_\| cos\Omega \tag{6.16}$$

$$\delta_\beta = \pi_E \epsilon_\perp sin\Omega \tag{6.17}$$

To generate our parallax measurements, we make the assumptions as in (Bachelet, Hinse, & Street 2018):

1. Source is in the galactic bulge: $D_s = 8$ kpc

2. $D_L = 4$ kpc

3. $\mu_{rel} = 200\dfrac{Km}{s}$

We can write $t_E\mu_{rel} = \theta_E$ (Gould 2000) (Yan & Zhu 2022).

$$\pi_E = \frac{AU(D_{LS})}{t_E\mu_{rel}D_LD_S} \tag{6.18}$$

$$= \frac{AU(0.000624s)}{t_E} \tag{6.19}$$

We can use equation 6.10 and equation 6.12 with the given value for π_E in equation 6.19. Our simulations vary the value of R and Φ to determine the effect of CS reconstruction on photometric curves with a microlensing parallax. We use R values as shown in Table 6.2.

R	t_E	Cadence	Observation time
7000 km	1 day	48 minutes	1 day
42000 Km	1 day	48 minutes	1 day
1 AU	1 day	5.02 days	150.5 days

Table 6.2: Simulation setup parameters

The different R values approximately correspond to the type of orbit the constellation could be in: low earth orbit, geosynchronous orbit, and solar orbit, respectively (Bachelet, Hinse, & Street 2018). We use 8 equally space Φ values. Hence, our results could show the effect for any constellation spaced at the given Φ values: $\frac{\pi}{8}, \frac{\pi}{4}, \frac{3\pi}{8}, \frac{\pi}{2}, \frac{5\pi}{8}, \frac{3\pi}{4}, \frac{7\pi}{8}, \pi$

A t_E value of 1 day depicts photometric curves due to free floating planets.

6.1.2 Compressive Sensing Setup

For CS application, we a generate a crowded star field with Airy PSF with PSF radius ranging from (1,5) pixel units. For $n \times n$ image, we generate $0.75 \times n \times n$ star sources. The flux of the star sources range from 50 to 5000 units. In our simulations we use $m = 0.25 \times n$, where m is the number of CS measurements obtained. A Bernoulli measurement matrix is used, which is varied during each Monte Carlo simulation. For a given R and Ω, we run 100 Monte Carlo simulations at each time sample, t. For CS reconstruction, we use the greedy algorithm, orthogonal matching pursuit, as its computational time is relatively less than optimization algorithms.

6.2 Results

In our first set of simulations for $R = 7000\text{km}$, we get the different parallax light curves for each varying Φ as shown in Figure 6.1, with the legend shown in Figure 6.2. The photometric curve without parallax, labeled as Original, is also shown for comparison. We perform 100 Monte Carlo simulations for each time sample. The average CS reconstruction error is shown in Table 6.3. For each R value, we show % error in peak magnification value between each parallax photometric curve as well as the difference in time shift for the peak magnification.
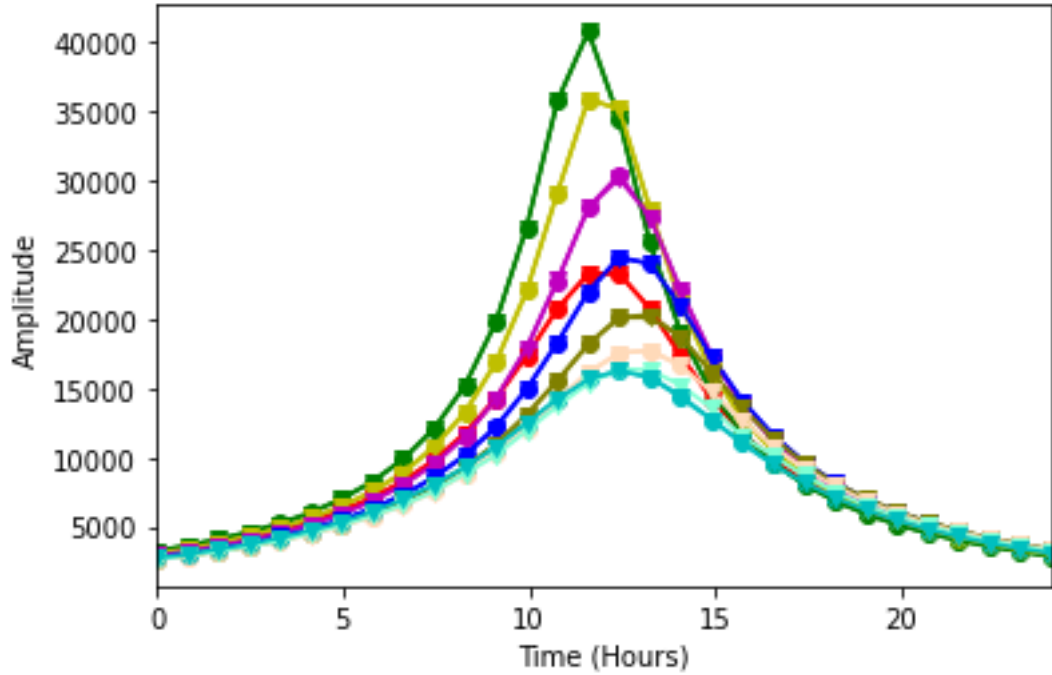
FIG. 6.1: Photometric curves generated by different parallax values, shown with its corresponding CS reconstructed curve for R = 7000 Km

128

- Original
- $\Phi = 0$
- $\Phi = \frac{\pi}{8}$
- $\Phi = \frac{\pi}{4}$
- $\Phi = \frac{3\pi}{8}$
- $\Phi = \frac{\pi}{2}$
- $\Phi = \frac{5\pi}{8}$
- $\Phi = \frac{3\pi}{4}$
- $\Phi = \frac{7\pi}{8}$
- CS reconstructed
- CS $\Phi = 0$
- CS $\Phi = \frac{\pi}{8}$
- CS $\Phi = \frac{\pi}{4}$
- CS $\Phi = \frac{3\pi}{8}$
- CS $\Phi = \frac{\pi}{2}$
- CS $\Phi = \frac{5\pi}{8}$
- CS $\Phi = \frac{3\pi}{4}$
- CS $\Phi = \frac{7\pi}{8}$
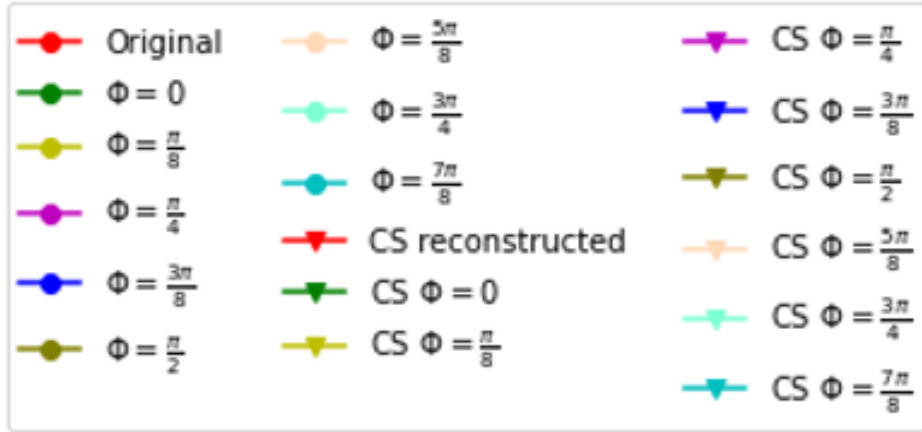
FIG. 6.2: Legend for Figure 6.1

Φ	0	$\frac{\pi}{8}$	$\frac{\pi}{4}$	$\frac{3\pi}{8}$	$\frac{\pi}{2}$	$\frac{5\pi}{8}$	$\frac{3\pi}{4}$	$\frac{7\pi}{8}$
Avg % Err	0.175	0.230	0.088	0.109	0.163	0.161	0.240	0.098
Avg % Err at peak	0.075	0.06	**1.07**	0.068	**1.09**	0.076	0.081	0.073
Std dev. % Err at peak	0.057	0.064	**9.94**	0.056	**9.94**	0.086	0.070	0.068

Table 6.3: % Error for CS reconstruction for each Φ for R = 7000 km. The second row shows average % error over all time samples, the third row shows average % error at peak magnification and the last rows shows the standard deviation of the % error at peak magnification

	0	$\dfrac{\pi}{8}$	$\dfrac{\pi}{4}$	$\dfrac{3\pi}{8}$	$\dfrac{\pi}{2}$	$\dfrac{5\pi}{8}$	$\dfrac{3\pi}{4}$	$\dfrac{7\pi}{8}$
0	-	12.0	25.3	40.0	50.2	56.5	59.8	60.1
$\dfrac{\pi}{8}$	13.6	-	15.2	31.8	43.4	50.6	54.4	54.7
$\dfrac{\pi}{4}$	33.9	17.9	-	19.6	33.3	41.7	46.2	46.6
$\dfrac{3\pi}{8}$	66.7	46.7	24.5	-	16.9	27.5	33.1	33.5
$\dfrac{\pi}{2}$	101	76.6	49.8	20.4	-	12.7	19.4	20.0
$\dfrac{5\pi}{8}$	130	102	71.6	37.9	14.5	-	**_7.72_**	**_8.34_**
$\dfrac{3\pi}{4}$	149	119	85.9	49.4	24.1	**_8.36_**	-	**_0.674_**
$\dfrac{7\pi}{8}$	151	121	87.2	50.4	24.9	9.10	**_0.679_**	-

Table 6.4: % error at peak magnification over 100 Monte carlo simulations, between microlening photometric curve with Φ shown in the first row, compared to the photometric curve with Φ in the first column. Error values for R = 7000 km. Values in bold underline show where % error between the two curves is less than 10%.

	0	$\dfrac{\pi}{8}$	$\dfrac{\pi}{4}$	$\dfrac{3\pi}{8}$	$\dfrac{\pi}{2}$	$\dfrac{5\pi}{8}$	$\dfrac{3\pi}{4}$	$\dfrac{7\pi}{8}$
0	-	0	0.828	0.828	1.66	1.66	0.828	0.828
$\dfrac{\pi}{8}$	0	-	0.828	0.828	1.66	1.66	0.828	0.828
$\dfrac{\pi}{4}$	0.828	0.828	-	0	0.828	0.828	0.	0
$\dfrac{3\pi}{8}$	0.828	0.828	0	-	0.828	0.828	0	0
$\dfrac{\pi}{2}$	1.66	1.66	0.828	0.828	-	0	0.828	0.828
$\dfrac{5\pi}{8}$	1.66	1.66	0.828	0.828	0	-	0.828	0.828
$\dfrac{3\pi}{4}$	0.828	0.828	0	0	0.828	0.828	-	0
$\dfrac{7\pi}{8}$	0.828	0.828	0	0	0.828	0.828	0	-

Table 6.5: Time difference in **Hours** at peak magnification between microlening photometric curve with Φ shown in the first row, compared to the photometric curve with Φ in the first column. R = 7000 Km.

In the next set of simulations, we use R = 42000Km. We show the microlensing parallax curves and the photometric curve without microlensing parallax, shown as Original, in Figure 6.3, with the figure legend shown in Figure 6.4. The corresponding errors due to CS reconstruction are shown in Table 6.6.
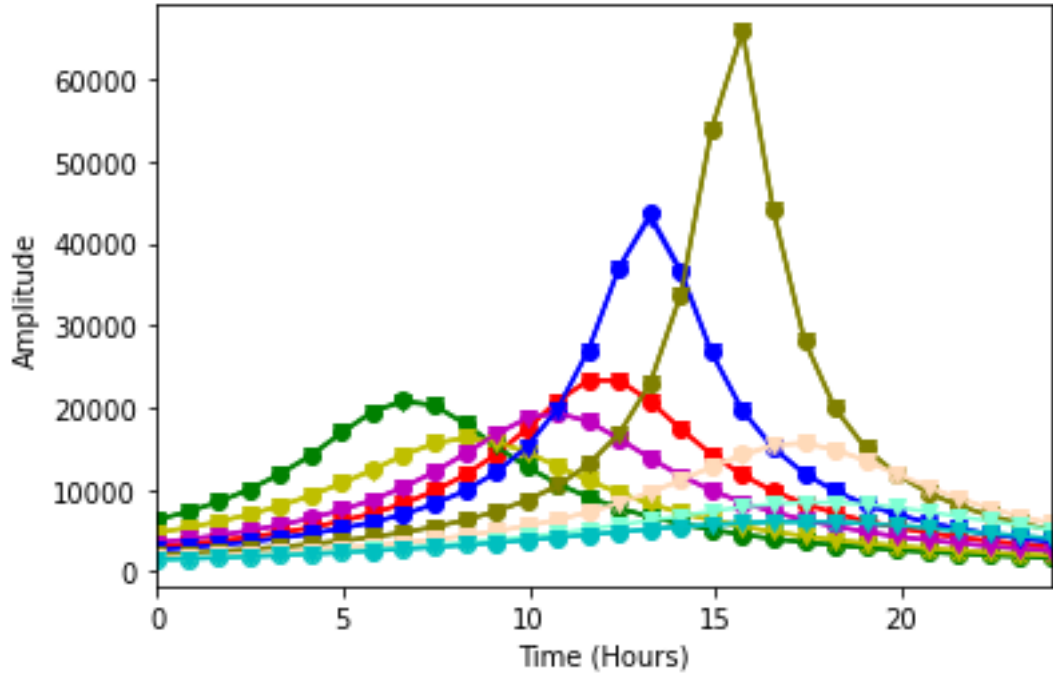
FIG. 6.3: Photometric curves generated by different parallax values, shown with its corresponding CS reconstructed curve for R = 42000 km. The original photometric curve without any microlensing effects is shown in red for comparison.
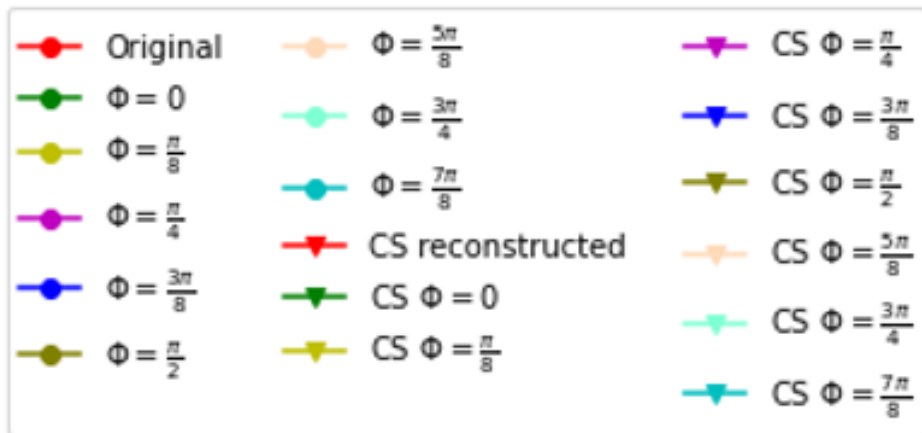
FIG. 6.4: Legend for Figure 6.3

Φ	0	$\dfrac{\pi}{8}$	$\dfrac{\pi}{4}$	$\dfrac{3\pi}{8}$	$\dfrac{\pi}{2}$	$\dfrac{5\pi}{8}$	$\dfrac{3\pi}{4}$	$\dfrac{7\pi}{8}$
Avg % Err	0.108	0.110	0.182	0.110	0.191	0.208	0.173	0.201
Avg % Err at peak	**1.07**	0.059	0.091	**1.07**	0.086	0.063	0.062	0.071
Std dev. % Err at peak	**9.94**	0.041	0.205	**9.94**	0.094	0.049	0.062	0.057

Table 6.6: % Error for CS reconstruction for each Φ for R = 42000 km. The second row shows average % error over all time samples, the third row shows average % error at t_0 and the last rows shows the standard deviation of the % error at t_0.

	0	$\dfrac{\pi}{8}$	$\dfrac{\pi}{4}$	$\dfrac{3\pi}{8}$	$\dfrac{\pi}{2}$	$\dfrac{5\pi}{8}$	$\dfrac{3\pi}{4}$	$\dfrac{7\pi}{8}$
0	-	22.1	7.50	109	215	25.1	59.7	70.9
$\dfrac{\pi}{8}$	28.3	-	18.7	168	305	**3.85**	48.3	62.6
$\dfrac{\pi}{4}$	8.11	15.8	-	126	241	19.0	56.5	68.5
$\dfrac{3\pi}{8}$	52.1	62.7	55.7	-	51.0	64.1	80.7	86.1
$\dfrac{\pi}{2}$	68.3	75.3	70.7	33.8	-	76.2	87.2	90.8
$\dfrac{5\pi}{8}$	33.5	**4.00**	23.5	179	321	-	46.2	61.1
$\dfrac{3\pi}{4}$	148	93.4	130	418	682	86.0	-	27.7
$\dfrac{7\pi}{8}$	243	168	218	617	982	157	38.3	-

Table 6.7: **% error** at peak magnification between microlening photometric curve with Φ shown in the first row, compared to the photometric curve with Φ in the first column. Error values for R = 42000 Km. Values in bold underline show where % error between the two curves is less than 10%.

	0	$\dfrac{\pi}{8}$	$\dfrac{\pi}{4}$	$\dfrac{3\pi}{8}$	$\dfrac{\pi}{2}$	$\dfrac{5\pi}{8}$	$\dfrac{3\pi}{4}$	$\dfrac{7\pi}{8}$
0	-	1.66	4.14	6.62	9.10	10.8	10.8	10.8
$\dfrac{\pi}{8}$	1.66	-	2.48	4.97	7.45	9.10	9.10	9.10
$\dfrac{\pi}{4}$	4.14	2.48	-	2.48	4.97	6.62	6.62	6.62
$\dfrac{3\pi}{8}$	6.62	4.97	2.48	-	2.48	4.14	4.14	4.14
$\dfrac{\pi}{2}$	9.10	7.45	4.97	2.48	-	1.66	1.66	1.66
$\dfrac{5\pi}{8}$	10.8	9.10	6.62	4.14	1.66	-	0	0
$\dfrac{3\pi}{4}$	10.8	9.10	6.62	4.14	1.66	0	-	0
$\dfrac{7\pi}{8}$	10.8	9.10	6.62	4.14	1.66	0	0	-

Table 6.8: Time difference in **Hours** at peak magnification between microlening photometric curve with Φ shown in the first row, compared to the photometric curve with Φ in the first column. Error values for R = 42000 Km.

Figure 6.5 shows the microlensing parallax curves for R = 1 AU. In this figure, we do not show the microlensing curve without parallax (Original curve in Figure 6.1 and 6.3) for comparison as the Δ in u_0 and t_0 are significantly high and will not be clearly readable with the given sampling cadence and observation window. Figure 6.6 is the corresponding legend. In table 6.9, we show the % error due to CS reconstruction in the photometric curves.
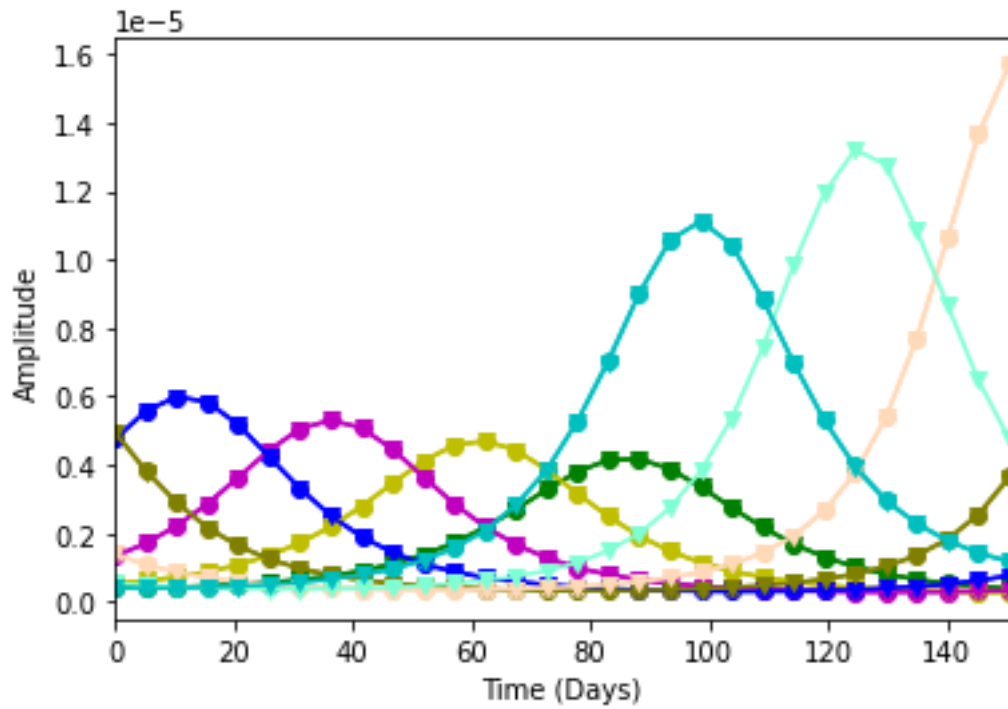
FIG. 6.5: Photometric curves generated by different parallax values, shown with its corresponding CS reconstructed curve for R = 1 AU. The magnification is signficantly lower because the differenced image is recoonstruced using our CS technique and the Δ in both u_0 and t_0 are significantly high.
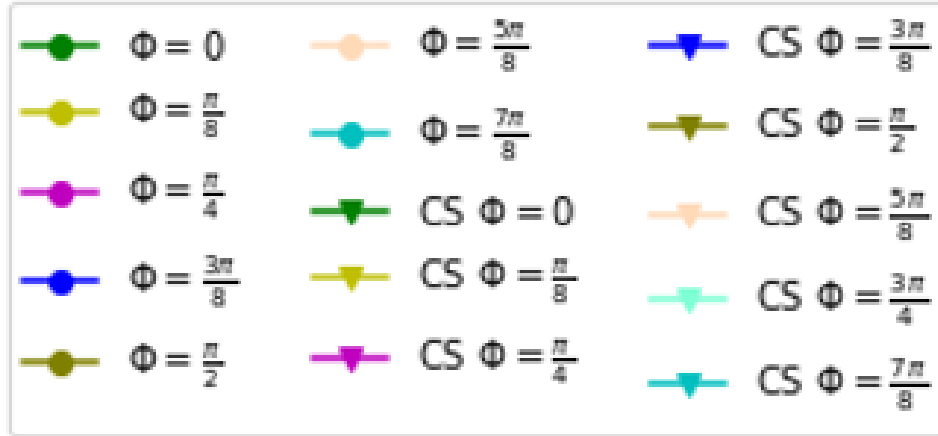
FIG. 6.6: Legend for Figure 6.5

Φ	0	$\dfrac{\pi}{8}$	$\dfrac{\pi}{4}$	$\dfrac{3\pi}{8}$	$\dfrac{\pi}{2}$	$\dfrac{5\pi}{8}$	$\dfrac{3\pi}{4}$	$\dfrac{7\pi}{8}$
Avg % Err	0.437	0.441	0.633	0.743	0.621	0.348	0.616	0.582
Avg % Err at peak	0.186	0.192	0.192	0.194	0.183	0.119	0.106	0.117
Std dev. % Err at peak	0.146	0.190	0.178	0.183	0.137	0.287	0.092	0.083

Table 6.9: % Error for CS reconstruction for each Φ for R =1 AU. The second row shows average % error over all time samples, the third row shows average % error at the peak of each curve and the last rows shows the standard deviation of the % error at the peak.

	0	$\dfrac{\pi}{8}$	$\dfrac{\pi}{4}$	$\dfrac{3\pi}{8}$	$\dfrac{\pi}{2}$	$\dfrac{5\pi}{8}$	$\dfrac{3\pi}{4}$	$\dfrac{7\pi}{8}$
0	-	12.7	27.2	43.7	18.7	276	217	167
$\dfrac{\pi}{8}$	11.3	-	12.8	27.5	**<u>5.34</u>**	234	181	137
$\dfrac{\pi}{4}$	21.4	11.4	-	13.0	**<u>6.65</u>**	196	149	110
$\dfrac{3\pi}{8}$	30.4	21.5	11.5	-	17.4	162	121	85.6
$\dfrac{\pi}{2}$	15.8	**<u>5.07</u>**	**<u>7.12</u>**	21.0	-	217	167	125
$\dfrac{5\pi}{8}$	73.4	70.0	66.2	61.8	68.4	-	15.7	29.1
$\dfrac{3\pi}{4}$	68.5	64.4	59.9	54.7	62.5	18.6	-	15.9
$\dfrac{7\pi}{8}$	62.5	57.7	52.3	46.1	55.5	41.0	18.9	-

Table 6.10: % error at peak between microlening photometric curve with Φ shown in the first row, compared to the photometric curve with Φ in the first column. Error values for R = 1 AU. Values in bold underline show where % error between the two curves is less than 5%.

	0	$\dfrac{\pi}{8}$	$\dfrac{\pi}{4}$	$\dfrac{3\pi}{8}$	$\dfrac{\pi}{2}$	$\dfrac{5\pi}{8}$	$\dfrac{3\pi}{4}$	$\dfrac{7\pi}{8}$
0	-	25.9	51.9	77.8	88.2	62.3	36.3	10.4
$\dfrac{\pi}{8}$	25.9	-	25.9	51.9	62.3	88.2	62.3	36.3
$\dfrac{\pi}{4}$	51.9	25.9	-	25.9	36.3	114	88.2	62.3
$\dfrac{3\pi}{8}$	77.8	51.9	25.9	-	10.4	140	114	88.2
$\dfrac{\pi}{2}$	88.2	62.3	36.3	10.4	-	151	125	98.6
$\dfrac{5\pi}{8}$	62.3	88.2	114	140	151	-	25.9	51.9
$\dfrac{3\pi}{4}$	36.3	62.3	88.2	114	125	25.9	-	25.9
$\dfrac{7\pi}{8}$	10.4	36.3	62.3	88.2	98.6	51.9	25.9	-

Table 6.11: Time difference in **Days** at peak between microlening photometric curve with Φ shown in the first row, compared to the photometric curve with Φ in the first column. Error values for R = 1 AU. Values in bold underline show where % error between the two curves is less than 5%.

Average CS reconstruction % error over all samples for the photometric curve with no microlensing parallax was 0.175% and the average % error at t_0 was 0.100%. Microlensing parallax provides a Δu_0, which shows the change in magnification amplitude, as well as a Δt_0, which shows a change in t_0 location. The higher the R value, the greater the Δ as evident in Tables 6.4, 6.5, 6.7, 6.8, 6.10, and 6.11. Our results show that there is no significant error for microlensing parallax event using CS techniques. For all the photometric curves the average error is less than 0.5% for all CS reconstructed curves and less than 1.1% at peak magnification time.
From our simulations, we note that the parallax curves get more distinguished for higher R values, that is, the time separation and amplitude separation between the

photometric curves is higher. From our simulations we show that the error due to CS reconstruction is less than the error between any two microlens parallax curves. However, we can use Tables 6.4, 6.7 and 6.10 as a basis to determine the optimal orbital phases to choose for satellite placement. Although CS reconstruction results show average error within the % error for the two curves, a better placement, if using less than 8 satellites, would be to choose orbital phases which have a greater microlensing detectability.

6.3 Conclusions

Our CS simulation results show error less than 0.5% over all time samples and average error less than 1.1% at t_0, while using 25% of traditional detector measurements for microlensing parallax light curves with a range of Φ from $[0, \dfrac{7\pi}{8}]$. Although different microlensing parallax at the three orbital radii generated different photometric curves with significant difference in flux magnitude, CS worked well for all the cases. The CS error at peak magnification for R = 7000 km, 42000 km and 1 AU, at each Φ value is less than the error between the parallax curve generated with that particular Φ value and any other parallax curve generated using the Φ value ranges. This shows that CS reconstruction should not cause any significant errors in detection of a microlensing parallax curve for any given Φ value. Using CS, we can significantly reduce on the data storage volume, as well as data downlink bandwidth-both of which can be a limitation for SmallSat type instruments. CS shows potential for implementation in a SmallSat constellation for detecting microlensing parallax events.

NOISE ANALYSIS FOR CS

RECONSTRUCTION

In this work we analyze the effect of noise on the detection of these events using Compressive Sensing (CS). We show numerical results on the impact of source and measurement noise on the reconstruction of transient photometric curves, generated due to gravitational microlensing events. In our work, we define source noise as background noise, or any inherent noise present in the sampling region of interest. For our models, measurement noise is defined as the noise present during data acquisition. These results can be generalized for any transient photometric CS measurements with source noise and CS data acquisition measurement noise. Our results show that the CS measurement matrix properties have an effect on CS reconstruction in the presence of source noise and measurement noise. We provide potential solutions for improving the performance by tuning some of the properties of the measurement matrices. For source noise applications, we show choosing a matrix with low mutual coherence and variance can lower the amount of error caused due to CS reconstruction. Similarly, for measurement noise addition, we show by choosing a lower expected value of the Binomial measurement matrix, we can lower the amount of error due to CS reconstruction.

7.0.1   Noise in Compressive Sensing Measurements

For our simulation modelling purposes we use architecture shown in Figure 4.5. We assume optimal differencing results, typically provided with both reference and observed images having the same detector response. The result of differencing can then be used to only detect a change in magnitude corresponding to a microlensing event. We can write the differenced image in that case as

$$x_{diff} = x_r - x_o \tag{7.1}$$

The differenced image consists of relevant information needed to reconstruct a transient photometric curve. From the architecture in Figure 4, we obtain

$$y_{diff} = y_r - y_o \tag{7.2}$$
$$= Ax_r - Ax_o \tag{7.3}$$
$$= A(x_r - x_o) \tag{7.4}$$
$$= A(x_\text{diff}) \tag{7.5}$$

Differencing the images makes them sparse with non-zero pixel coefficients for only the star sources experiencing magnification. Adding noise leads to less sparse images, which can hinder performance of CS reconstruction algorithms. Further details on the type of noise used in our work is discussed in section 7.1.

For 2D images, we apply CS in the following manner.

1. Generate a spatial sky image of size $n \times n$ using uniform random distribution, in the range of 50 and 5000 pixel value. The radius of these star sources are

generated using an airy point spread function with aperture radius between 1 and 5 pixel units, uniform randomly chosen.

2. Magnification for the source star experiencing a single lensed microlensing event is determined by the microlensing equations (Seager 2010). The center pixel value, $P[x_0, x_1]$, at any time, t, is given by

$$\mathrm{Amp}[x_0, x_1] = M(t) \times P[x_0, x_1] \qquad (7.6)$$

Where *Amp* is the amplification value, P is the pixel value from step 1, and M(t) is the magnification value at time, t.

3. If adding background noise, generate a noise image of the same size, n x n. Add this image to the image generated in step 1.

4. Generate a CS based projection matrix of size $m \times n$, where $m = q\% \times n$. In our simulations, we use $q = 25$

5. Create CS based measurements by

$$y_o = Ax_o + n_t \qquad (7.7)$$

where x_o is the observed spatial region, y_o is the CS measurements acquired from applying CS on x_o and n_t is the total measurements noise added.

6. Create CS based measurements from a reference image, x_r and the same measurement matrix, A:

$$y_r = Ax_r \qquad (7.8)$$

142

7. Obtain the difference, $y_{\text{diff}} = y_o - y_r$

8. Reconstruct x_{diff} using CS reconstruction algorithms, given y_{diff} and A.

7.1 Noise in Compressive Sensing Measurements

In this section, we discuss two types of noise: source noise and measurement noise.

7.1.1 Source Noise

This noise is associated with the sampling star field itself. The star sources can be contaminated with flux from surrounding stars. In addition, other sky background noise can leak into the source star flux measurement. For our analysis, we will assume the source noise is of Gaussian distribution. We can characterize it by

$$y = A(x + n_b) \tag{7.9}$$

where n_b is Gaussian noise. In this case, noise gets folded into the measurement matrix, A (Arias-Castro & Eldar 2011). Incorporating this for differenced images, as stated in equation (7.5),

$$y_{\text{diff}} = A(x_o + n_b) - A(x_r) \tag{7.10}$$

$$= A(x_{\text{diff}} + n_b) \tag{7.11}$$

$$= A(x_{\text{diff}}) + A(n_b) \tag{7.12}$$

where $x_{\text{diff}} = x_o - x_r$

7.1.2   Measurement noise

Measurement noise is associated with the data acquisition process at the detector front end. For measurement noise, we model photocurrent shot noise using Poisson distribution, as well as thermal noise using Gaussian distribution. This modelling can be generalized to any type of noise which either requires applying Poisson noise or additive Gaussian noise to the data measurements.

Shot Noise   Shot noise is associated with the implicit arrival of electrons at the detector. This noise is applied to the detector measurements (Jauregui-Sánchez *et al.* 2018), (Hasinoff 2014). For equation purposes, we write this as additive noise to Ax. However, for practical purposes, shot noise is applied to Ax, as it is dependent on the signal and thus, cannot be added independently to the measurements.

$$y = Ax + n_s \tag{7.13}$$

Thermal noise   This noise is produced by the random motion of electrons in the detector (Jauregui-Sánchez *et al.* 2018), (Zmuidzinas 2003). We can model this by stationary Gaussian random noise.

$$y = Ax + n_t \tag{7.14}$$

7.1.3   Total Noise in detectors

Since random, uncorrelated noise adds quadratically, total detector noise, n_{st} is given by

$$n_{st} = \sqrt{n_s^2 + n_t^2} \tag{7.15}$$

where n_s is shot noise and n_t is thermal noise. Incorporating all the noise sources, CS can be modelled as

$$y = A(x + n_b) + n_{st} \tag{7.16}$$

Total noise is

$$N = An_b + n_{st} \tag{7.17}$$

In our simulations, we model each of the noise sources separately to understand the effects relevant to each noise source.

7.2 Noise effects on compressive sensing

In this section, we discuss theoretical implications of noise on CS reconstruction. For source noise, we generate Gaussian random noise. By varying standard deviation of the Gaussian kernel, we can obtain noise with different Signal-Noise-Ratios (SNR). We define SNR as

$$SNR = 10 \log_{10} \left(\frac{\sum_i x_{oi}}{n \times n} - \frac{\sum_i x_{oni}}{n \times n} \right) \tag{7.18}$$

where x_o is the observed image, and x_{on} is the noisy observed image.

Since A and n_b are independent random variables, the expected value of the noise is

$$E[N] = E[A]E[n_b] + E[n_s] + E[n_t] \tag{7.19}$$

Given n_b has a Gaussian distribution with mean 0, expected value of $E[A]E[n_b] = 0$. If we assume thermal noise to be normally distributed as well, $E[n_t] = 0$. Hence $E[N] = E[n_s]$ in those circumstances. For all independent noise sources, variance is

given by

$$Var[N] = Var[A]Var[n_b] + Var[n_s] + Var[n_t] \qquad (7.20)$$

In our work we propose to construct A such that it has a low variance. We compare results with a Binomial distribution as well as Gaussian distribution.

In this section, we also describe mutual coherence of a matrix and its relation to CS reconstruction. Hence, the variance of the noise as well as mutual coherence, μ, of A will factor in the reconstruction accuracy using CS methods.

7.2.1   Mutual Coherence of a matrix

From (Eldar & Kutyniok 2012), we can incorporate the following equations for CS analysis. First, we define $\mu(A)$ as given in (Eldar & Kutyniok 2012):

$$\mu(A) = \max_{1 \leq i < j} \frac{|<a_i, a_j>|}{||a_i||_2 ||a_j||_2} \qquad (7.21)$$

where A is the measurement matrix and a represents a column of A.

Given A, the sparsity of the signal, or the number of non-zero elements, k, in a signal is given by equation 7.22 (Eldar & Kutyniok 2012).

$$k < \frac{1}{2}\left(1 + \frac{1}{\mu(A)}\right) \qquad (7.22)$$

Hence, we want $\mu(A)$ to be as low as possible, in order to increase the bound for k. This will ensure a higher accuracy in CS reconstruction with a higher sparsity tolerance in signals.

7.3 Numerical Results

To analyze the effect on single lensed microlensing events in crowded star fields, we generate dense stellar fields with Airy spread point sources. For a 128×128 pixel image, we generate star sources equal to 75% of the total number of pixels Each star is chosen to have a Airy disk radius between 1 and 5 in pixel units and amplitude ranging from 50 to 5000 units. The values are chosen randomly from a uniform random distribution. For an image of size $n \times n$, where $n = 128$, we use $m = 0.25 \times n$. From equation 2.2, y is of size $m \times n$. For transient events, as portrayed by our modelling using single lens gravitational microlensing, we want to reconstruct the time domain signal, representing the pixels experiencing a transient event. For CS, sparsity is essential, hence, in our simulations we apply CS on differenced images, which are sparse. We difference the crowded star fields with a reference image. For understanding the effect of noise, the crowded stellar images have noise added. Thus, when differenced, noise as well as the microelensed star should be evident in the residual. For ideal comparison, we simulate detector point spread function (PSF) to be the same for the observed and reference image. Noise is the only addition in the observed image. Hence, in the differenced image, the characteristics of the noise are preserved. In our simulations we use Orthogonal Matching Pursuit (OMP) to reconstruct CS measurements. Convex optimization algorithms provide better accuracy in reconstruction (Pope 2009) than greedy algorithms. However, greedy algorithms are computationally less complex and can have faster run times. Due to the latter advantage, we use greedy algorithms to run 100 Monte Carlo simulations for each set of parameters.

Percent error as described in equation 7.23 is used as a metric to quantify the accuracy in reconstruction of the image.

$$\frac{|f'_{\text{diff}} - f_{\text{diff}}|}{f_{\text{diff}}} \times 100\% \tag{7.23}$$

where f'_{diff} and f_{diff} are the total fluxes within the 3-pixel radius of the source positions of the reconstructed and original differenced images, respectively. The error at the source star is of critical importance as the photometric light curve is generated based on the magnification of the source star of interest.

Gravitational Microlensing Setup   For all our simulations, we use a gravitational microlensing curve generated by a single lens. The amplification over time due to a single microlensing event is generated by the equation given in (Seager 2010).

$$A(t) = \frac{u_0^2 + \left(\dfrac{t - t_0}{t_E}\right)^2 + 2}{\left[\mu_0^2 + \left(\dfrac{t - t_0}{t_E}^2\right)\right]^{1/2} \left[\mu_0^2 + \left(\dfrac{t - t_0}{t_E}\right)^2 + 4\right]^{1/2}} \tag{7.24}$$

Here, t is the time sample, u_0 is the impact parameter, t_0 is the peak magnification time, and t_E is the Einstein ring radius crossing time. In our simulations we use $\mu_0 = 0.1$ and $\mu_0 = 0.01$ to vary the amplitude of the photometric curve, in order to understand the effect of noise with the different magnifications. We use $t_0 = 15$ and $t_E = 30$. Figure 7.1 shows sample magnification curves with $\mu_0 = 0.1$ and $\mu_0 = 0.01$. The lower μ_0 value provides a higher magnification of the light curve.
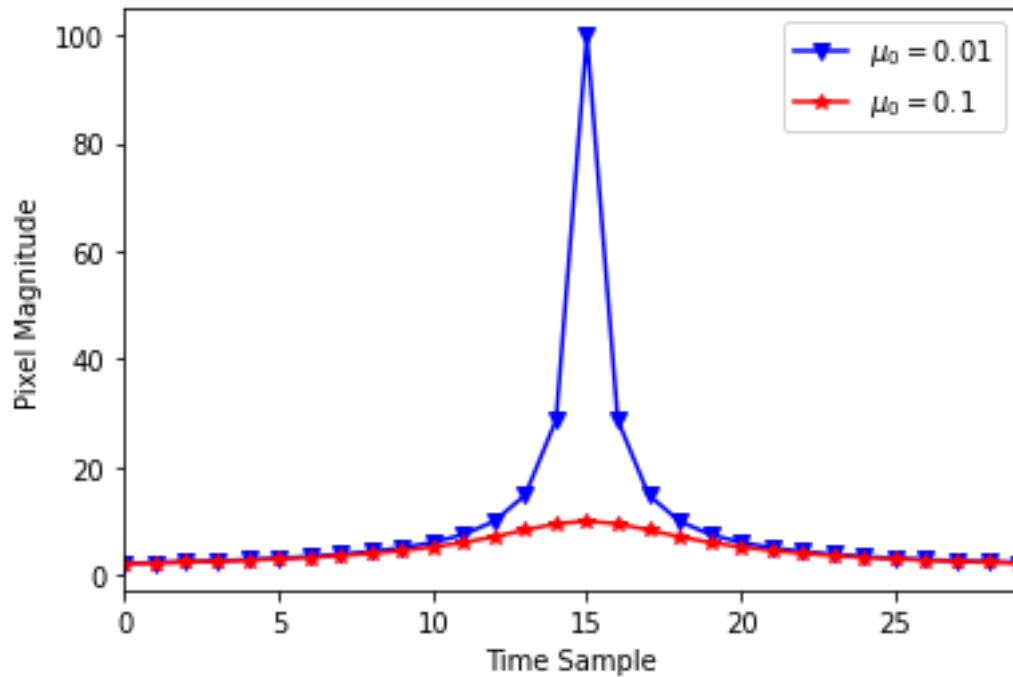
FIG. 7.1: Magnification curve for $\mu_0 = 0.1$ and $\mu_0 = 0.01$

In practical applications where the samples are not exactly zero, we can distinguish sparse signals as signals whose coefficients decay at a high rate. In figures 7.2 and 7.3, We show the rate of decay of the coefficients for $\mu_0 = 0.1$ and $\mu_0 = 0.01$.
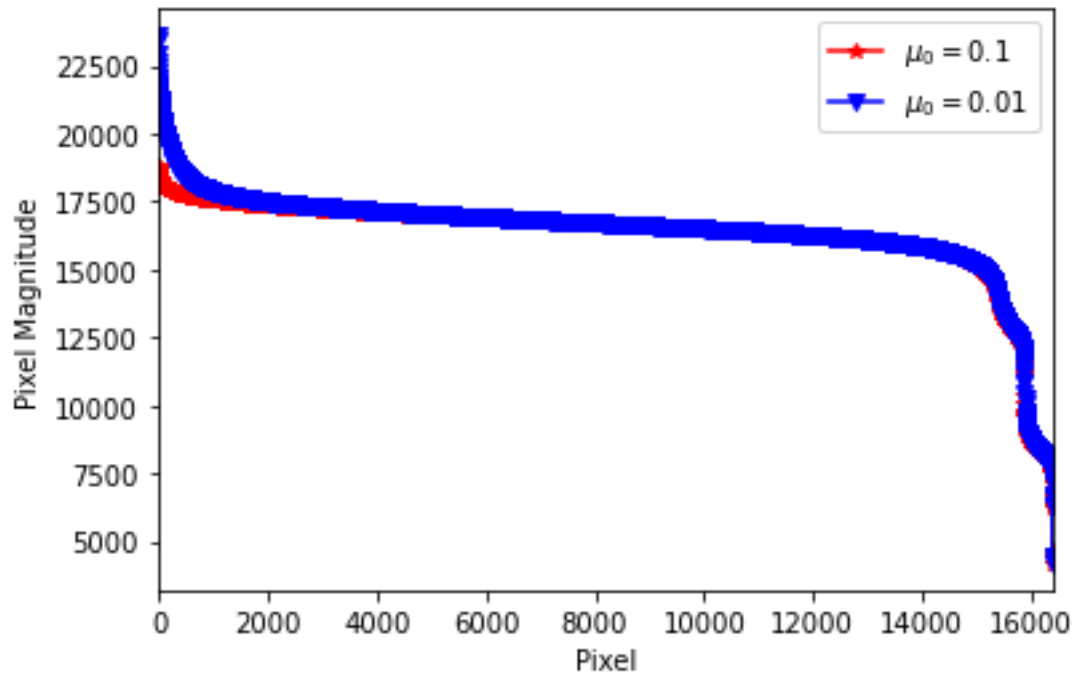
FIG. 7.2: Rate of decay of coefficients for $\mu_0 = 0.1$ and $\mu_0 = 0.01$
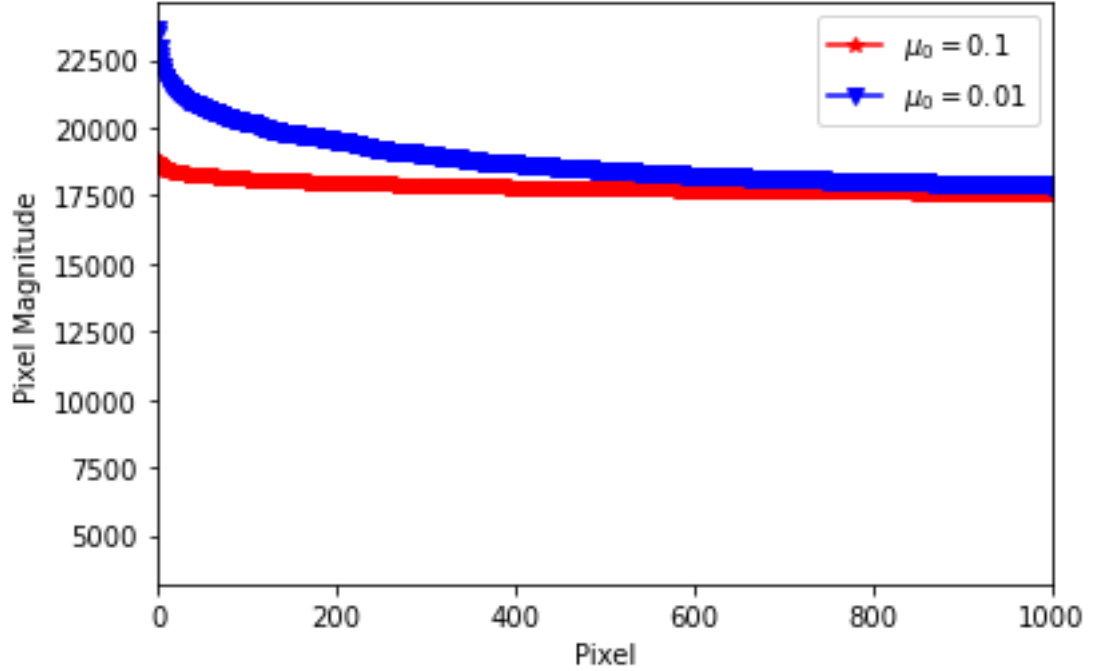
FIG. 7.3: Rate of decay of coefficients, zoomed in towards the higher magnification coefficients to view the difference between $\mu_0 = 0.1$ and $\mu_0 = 0.01$

Hence, it is evident that photometric curves with $\mu_0 = 0.01$ has a higher rate of decay as compared to photometric curves with $\mu_0 = 0.1$. Hence for CS, sparser signals should have better reconstruction accuracy.

CS Analysis with Source Noise This set of simulations vary the amount of source noise, n_b, added to the observed image for a single lens microlensing event with $\mu_0 = 0.1$ and $\mu_0 = 0.01$. Simulations are performed using the model described in equation 7.9.

To characterize source noise or background noise, we use Gaussian noise, with mean 0 and varying standard deviation. By varying the standard deviation of the added Gaussian noise, we obtain the different SNRs for the observed image and noisy

observed image. Figure 7.4 shows CS reconstruction error with different amounts of added source noise to the observed image. Binomial measurement matrix with 25% CS measurements is used for this simulation.
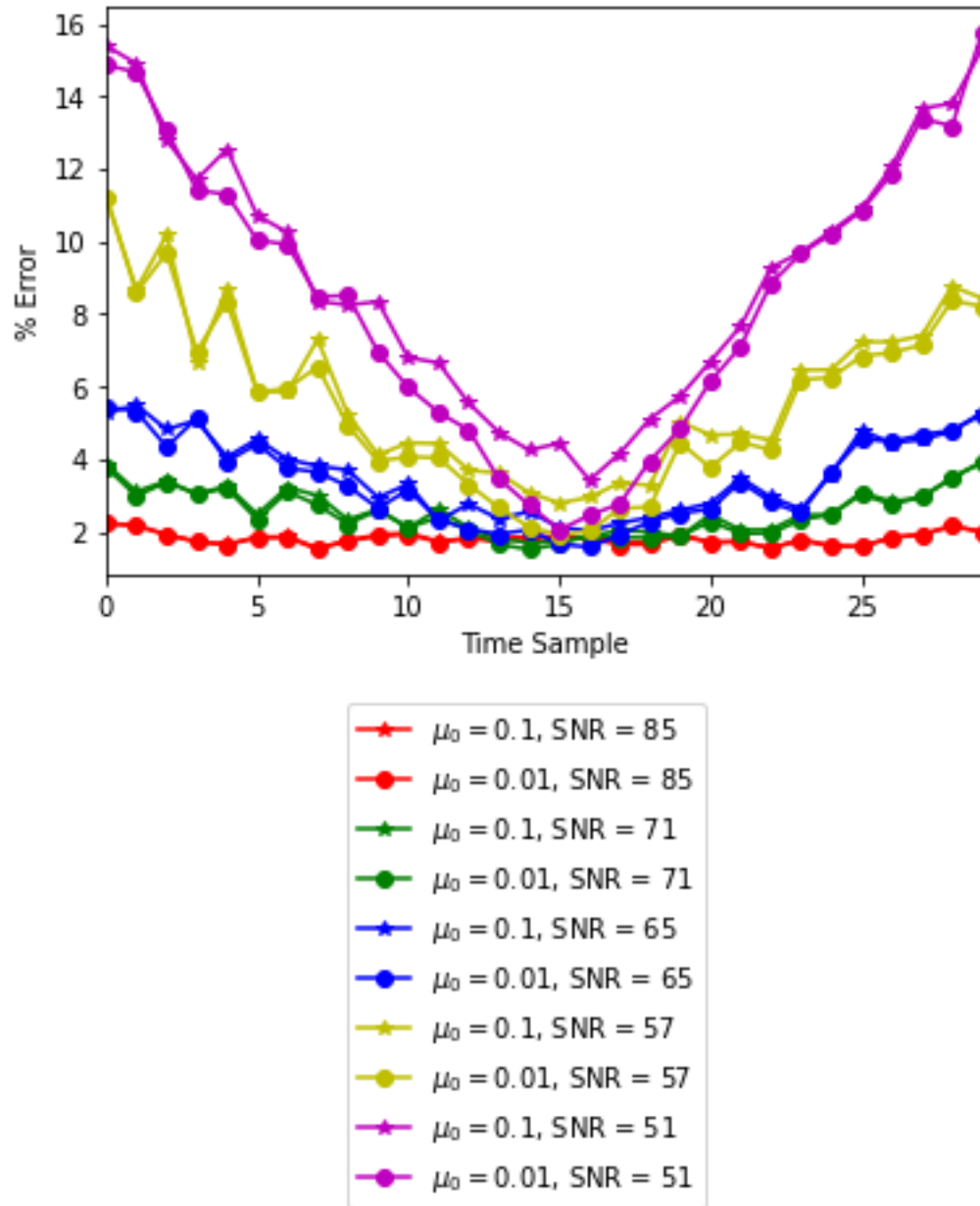
FIG. 7.4: % error for an image with added Gaussian source noise for a single lensed microlensing event with $\mu_0 = 0.1$ and $\mu_0 = 0.01$ for varying levels of Gaussian noise addition to the spatial region of interest.

In Figure 7.4, we can note that % error is the lowest when the magnification peaks

at t_0, as shown in Figure 7.1. We also see the effect of the different levels of noise on the % error. Figure 7.5 shows the comparison between $\mu_0 = 0.1$ and $\mu_0 = 0.01$. As the SNR decreases, the % error difference between the two μ_0 also increases. High magnification events, where μ_0 is lower, sparisty is higher. Thus, % error is lower in those circumstances, as noted in figure 7.5. From Figure 7.4 and Figure 7.5, it is evident that for low SNR images, CS reconstruction works better when the impact factor, $\mu_0 = 0.01$ as opposed to when $\mu_0 = 0.1$. A summarizing result from this figure is that CS works well for high magnification images, even with addition of noise, following the need for sparsity in signals for accurate CS reconstruction.
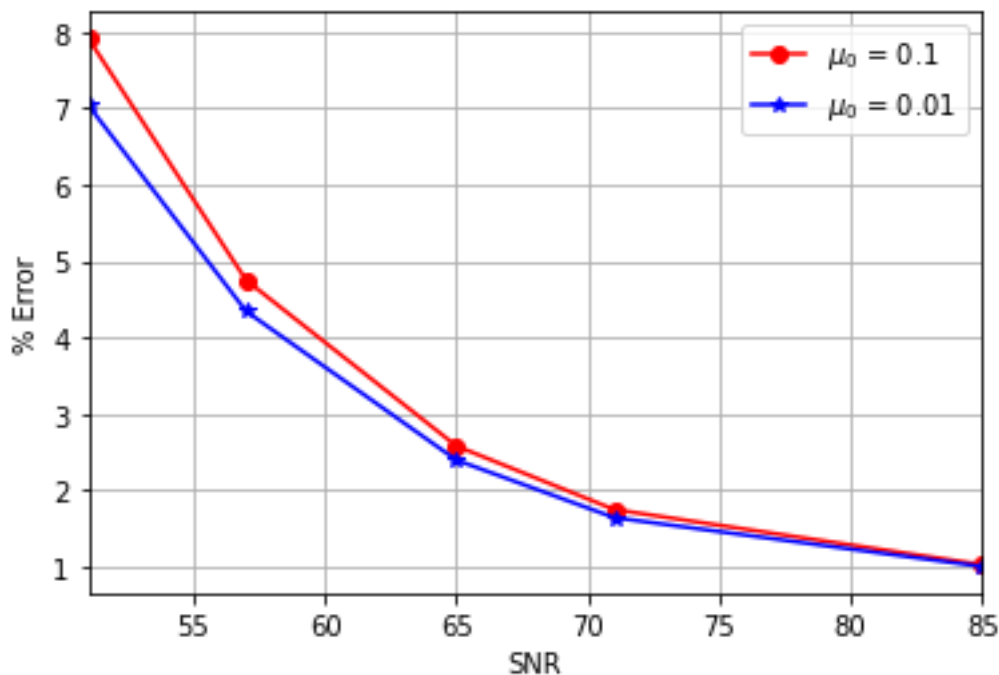
FIG. 7.5: Average % error for an image with added Gaussian source noise for a single lensed microlensing event with $\mu_0 = 0.1$ and $\mu_0 = 0.01$

For source noise, as shown in equation 7.9, both x and n_b are impacted by the

measurement matrix A. Hence, tuning A would not affect the noise alone. The SNR would remain constant, even if the variance of A is changed. In this section we show the effect of choosing A on CS reconstruction. We show the % error as a function of SNR. From equation 7.20, we get total noise variance for added Gaussian source noise with noise variance, σ_n^2, as shown in Table 7.1.

Measurement Matrix, A	Total Noise Variance	Average $\mu(A)$
Gaussian with $\sigma^2 = 0.25$	$0.25{\times}\sigma_n^2$	0.616
Binomial with $\sigma^2 = 0.25$	$0.25{\times}\sigma_n^2$	0.841

Table 7.1: Total noise variance and mutual coherence of A, $\mu(A)$, with the given properties of A
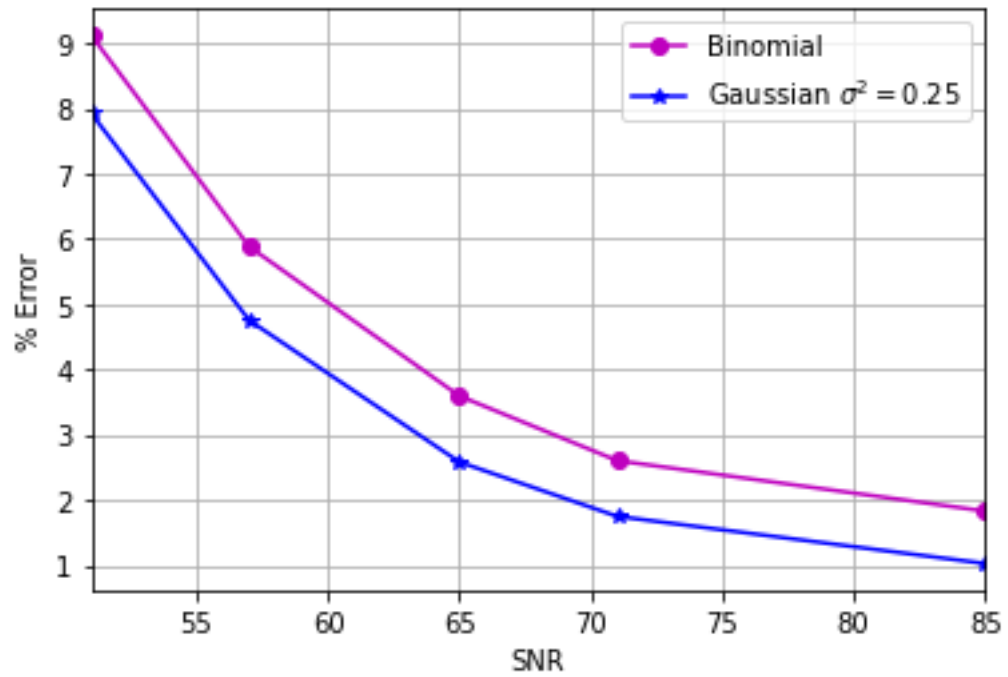
FIG. 7.6: % error for an image with added Gaussian source noise for a single lensed microlensing event with $\mu_0 = 0.1$. Binomial and Gaussian measurement matricies, with the given variance, are used for comparison.
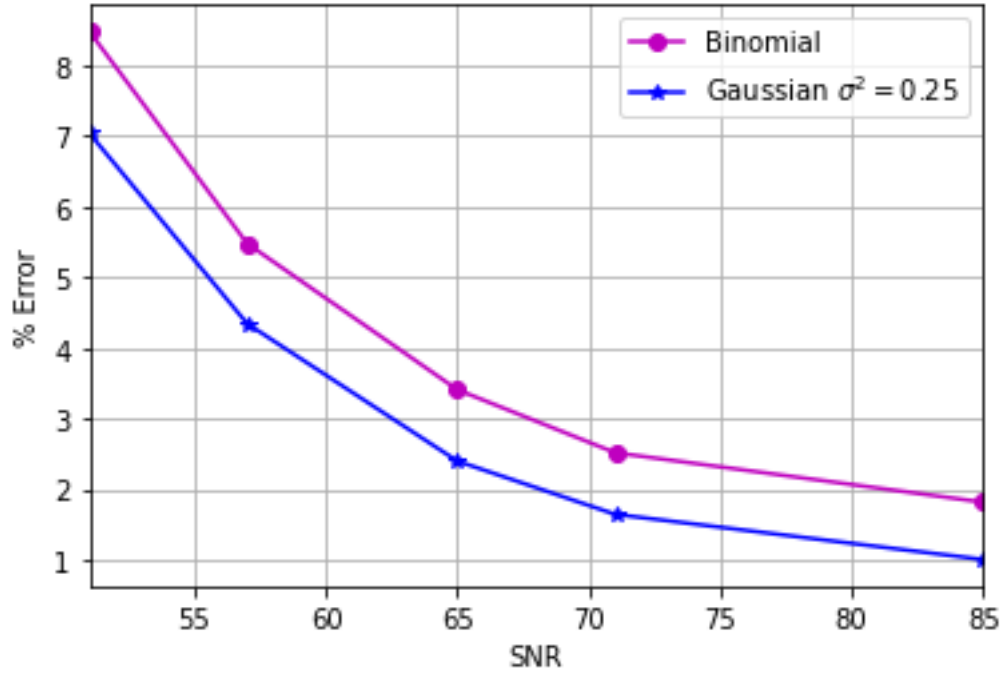
FIG. 7.7: % error for an image with added Gaussian source noise for a single lensed microlensing event with $\mu_0 = 0.01$. Binomial and Gaussian measurement matricies, with the given variance, are used for comparison.

From figure 7.6 and figure 7.7, we note that CS reconstruction is better with lower mutual coherence measurement matrices. By adding source noise, we are making the images less sparse, thus, Gaussian measurement matrix, which has lower mutual coherence works better. In the case of source noise, variance of A does not affect CS reconstruction. Changing the variance of A is equivalent to scaling the y measurements. A matrix folds into x as well as n_b, thereby retaining the same SNR level, and thus in turn, should have no effect on CS reconstruction.

7.3.1 CS with added measurement noise

For our numerical analysis, we use addition of shot noise, as well as thermal noise. Typically shot noise is of Poisson distribution. Poisson noise is applied and cannot be added, as it is signal dependent. Hence, for each element in y, Poisson noise is applied by generating a Poisson distribution with $\lambda =$ the value of that specific element in y. Here λ is the expected value of the Poisson distribution. We apply Poisson noise to different simulated star fields, over 100 simulations, and obtain the average % error over all the Monte Carlo simulations. We use A as a Binomial random matrix. The expected value of the product of the two independent probability distributions are given by

$$E[\lambda] = E[y] = E[A]E[x] \tag{7.25}$$

$$= p\left(\frac{1}{2}(x_h - x_l)\right) \tag{7.26}$$

where λ is the expected value and variance of the Poisson distribution for each element in y, p is the expected value of the Binomial distribution in A with the number of trials $= 1$. Hence, $E[\lambda]$ refers to the expected value of the variance of the Poisson distribution over all samples of y. In order to reduce the Poisson noise variance, p can be tuned. However, CS reconstruction depends on $\mu(A)$, as well. Table 7.2 shows noise variance and mutual coherence of A for the binomial distributions with $p = 0.5$ and $p = 0.25$. Both the distributions have similar $\mu(A)$ values.

Measurement Matrix, A	Expected value of total noise variance	Average $\mu(A)$
Binomial with $p = 0.5$	$0.5E[x]$	0.841
Binomial with $p = 0.25$	$0.25E[x]$	0.789

Table 7.2: Total noise variance and mutual coherence for A with the given properties of a binomial distribution

Shot noise is applied using Poisson distribution to y_o. We apply Poisson noise with $\lambda = y_{oi}$, where i represents the i_{th} element in y_o. If the microlensing star pixel flux is lower than the other pixel star fluxes in the images, then the addition of Poisson noise to y_o can significantly degrade the CS reconstruction of x_o. Figure 7.8 show the effect of tuning p on CS reconstruction.
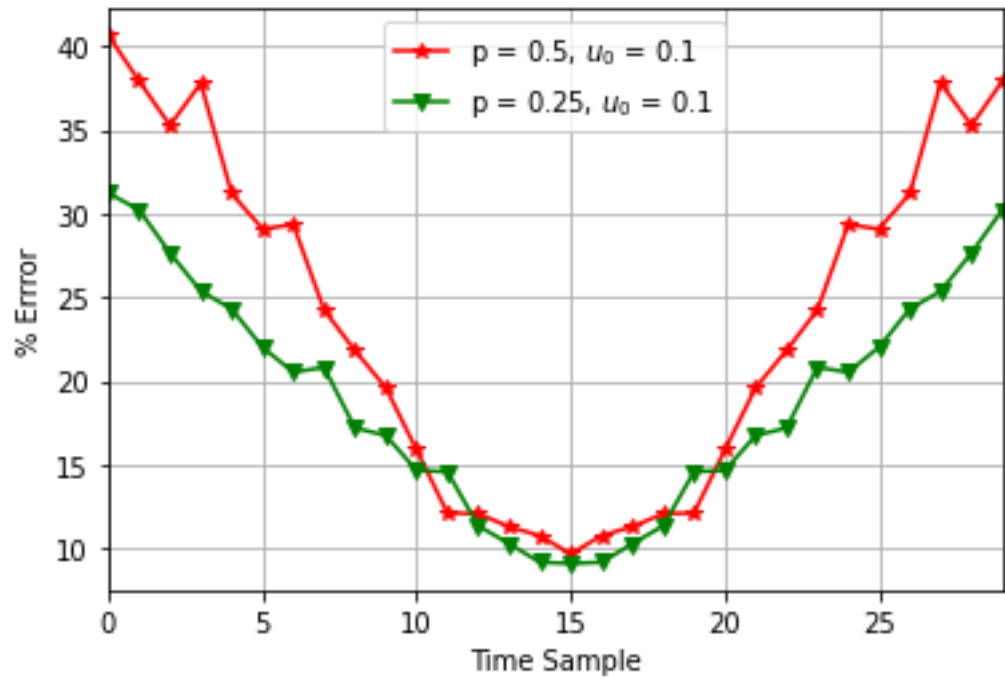
FIG. 7.8: Average % error for an image with applied Poisson noise to CS measurements for a single lensed microlensing event with $u_0 = 0.1$ using Binomial measurement matrix with $p = 0.5$ and $p = 0.25$
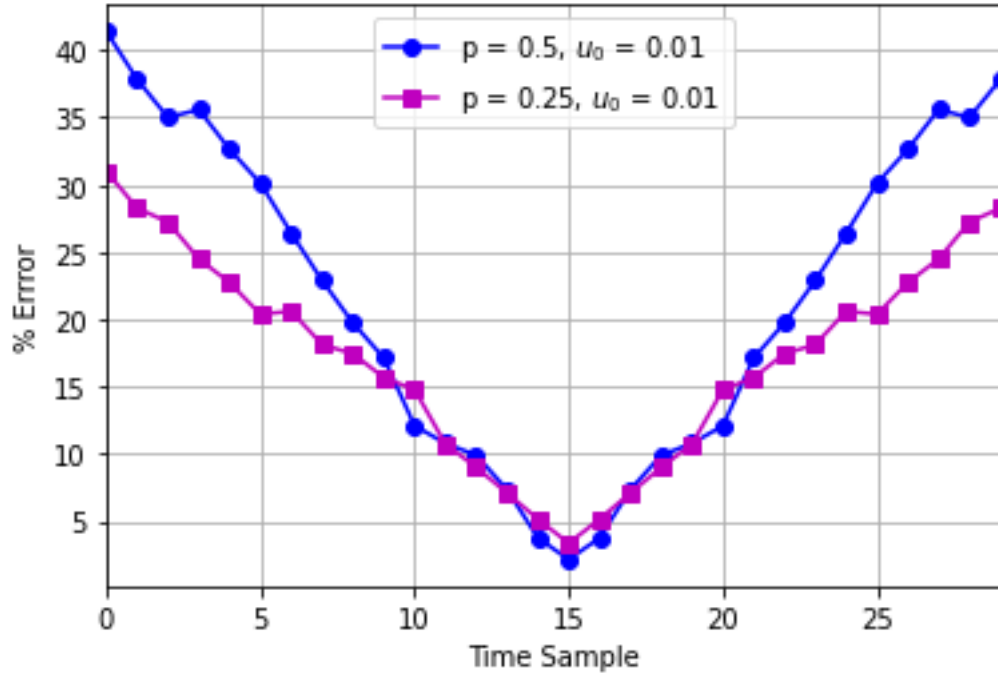
FIG. 7.9: Average % error for an image with applied Poisson noise to CS measurements for a single lensed microlensing event with $u_0 = 0.01$ using Binomial measurement matrix with $p = 0.5$ and $p = 0.25$

Figure 7.8 show that for high magnification pixels in the time-series light curve (as shown in Figure 7.1), Poisson noise error is lowest at those time samples, as compared to the low magnification time samples. Also, we show that by decreasing p of the Binomial matrix, A, we can decrease the noise error by an average of 4.6% over all time samples for $\mu_0 = 0.1$ and 4.27% for $\mu_0 = 0.01$.

In the next simulation, we apply thermal noise to the CS measurements by adding Gaussian noise. Figure 7.10 shows different amounts of Gaussian noise added to the CS measurements, as measured by the SNR of y_o. We also compare it with applied Poisson noise.
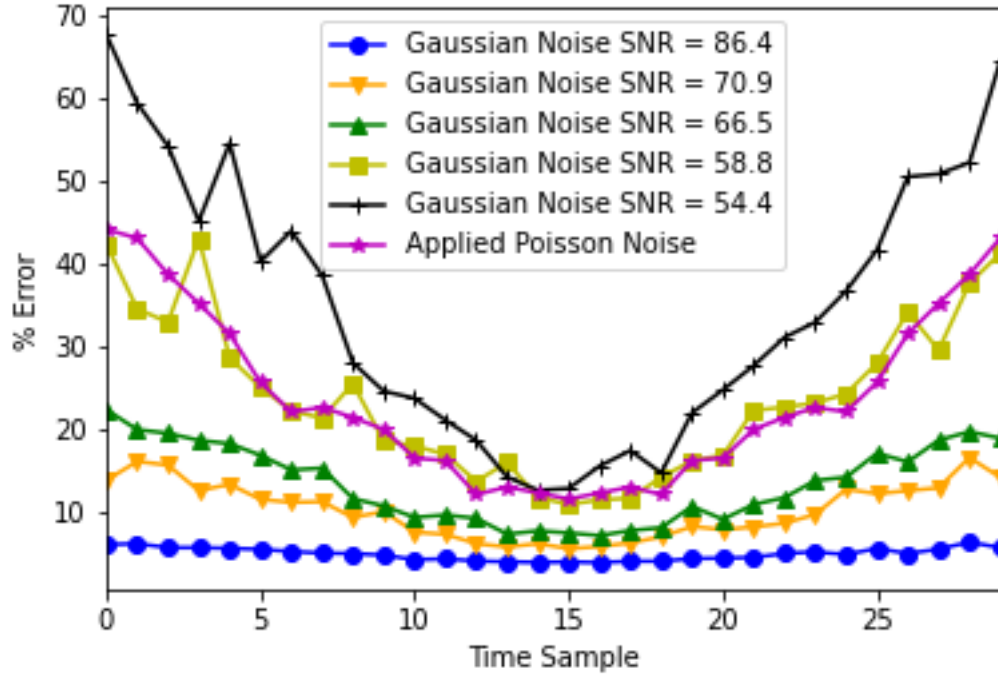
FIG. 7.10: % error for an image with applied Poisson noise to CS measurements as compared to addition of Gaussian noise to the CS measurements for a single lensed microlensing event with $\mu_0 = 0.01$, using Binomial measurement matrix, $p = 0.5$, $\sigma^2 = 0.25$.

Applying Poisson noise to CS measurements acquired from a differenced image of simulated crowded stellar field is roughly equivalent to adding Gaussian noise of SNR 58.8, given our model parameters in Section 7.3. From Figure 7.10, it is evident that CS measurement noise is higher for high SNR, low magnification pixels. As compared to Figure 7.5, CS measurements noise has a greater impact on CS reconstruction than CS source noise with similar SNR. However, for CS source noise, SNR is calculated using the observed image, x_o, and the noisy image, x_{on}, while for CS measurements, SNR is calculated using the acquired CS measurements from the observed image, y_o, and the noisy CS measurements from the observed image, y_{on}.

7.4 Conclusion

In our previous studies on application of compressive sensing to gravitational microlensing, we show that CS is able to reconstruct the light curve without compromising on science parameters of interest. However, our study did not incorporate the effect of noise. In this study, we show the effect of source noise as well as measurement noise. For source noise, we note that total noise variance is dependent on the measurement matrix. Our analytical results show that the variance of measurement matrix does not have an impact in the presence of source noise as the measurement matrix gets folded into the signal as well as noise. We compared Binomial measurement matrix with Gaussian measurement matrix. Binomial measurement matrix has a higher mutual coherence as compared to a Gaussian measurement matrix, as also shown through numerical simulations. Through our simulations, we can conclude that matrices with lower mutual coherence, provide better CS results. For the measurement noise analysis, we applied Poisson noise to depict shot noise, and Gaussian noise to depict thermal noise. As Poisson noise is dependent on the signal itself, we note that for high magnification events, where the flux of the microlensing source star pixels are comparatively higher, Poisson noise during CS measurements acquisition can lead to a lower % error. Also, we show through our analytical and numerical results, by reducing the value of p, where p represents the expected value of the Binomial distribution of A, we can achieve lower noise variance, thereby decreasing the average % error in CS reconstruction. Furthermore, our anlaysis of thermal noise addition shows the effects of CS reconstruction on the various amount of Gaussian noise added. As we decrease the SNR of the added Gaussian noise, the % error increases at a higher rate for the time samples with the lower magnification values.

COMPRESSIVE SENSING FOR SPACE FLIGHT INSTRUMENT CONSTELLATION

In this section, we describe implications of CS on space-flight instruments in a constellation.

8.1 State-of-the-Art Space Flight Instrumentation

The front-end-electronics for acquiring photometric measurements will be completely transformed to a novel data acquisition approach, resulting in fewer data samples, eventually putting the image reconstruction load onto computational imaging. Current detectors for imaging photometric events are comprised of Charge Couple Device (CCD) cameras. For space observatories, we discuss the latest transient photometric survey telescopes- Transiting Exoplanet Survey Satellite (TESS) and Nancy Grace Roman Space Telescope. TESS: There are four CCD cameras on TESS with a combined field-of-view of 24x96 degrees, making up one observation sector. There are such 13 sectors being observed serially. Each CCD has a 2048 x 2048 pixel detector array, with the four CCDs having an effective 4096 x 4096 pixel detector array, with less than 10 e- read noise. The cadence is about 30 minutes. In order to store such high volume data, a 192 gigabyte solid state recorder (SSR) is used. The data is

downlinked every 13.7 days. The data downlink per month is 8.5TB. Nancy Grace Roman Space Telescope: The wide field instrument is a 300Mega Pixel camera viewing. The instrument will be using H4RG detectors with 0.11 arcsec pixel scale. Data will be downlink at a rate of 290 Mbps with a total volume of 11 Tbits/day. A full frame readout will take 2.78 seconds with an effective field of view of 0.281 deg^2.

Key differences in the optical setup and read-out of traditional detectors and CS based detectors include:

Traditional Detectors	CS Detector
CCD Detectors	Typically designed with spatial light modulators and photodiode
Pixel by pixel readout of the image	Total power reflected from the matrix projected onto the image is measured
Digitization of each pixel readout	Digitization of the total power read

Both TESS and Nancy Grace Roman Space Telescope obtain large volumes of data, which requires a large on-board storage capacity, in addition to larger data bandwidth for data transmission. Through our simulation results we show that we can potentially reduce data volume to 25% of that required by traditional detectors. This detector is targeted for SmallSat type instruments. Hence, given the data and optics volume, we will determine the feasibility of using them on SmallSat type missions.

8.1.1 Parallax Measurements

The current state-of-art for microlensing parallax consists of large space observatories, like Nancy Grace Roman Space Telescope detecting an event, then alerting

a microlensing event, which is then followed up by a ground observatory. Use of large observatories is very costly. A CS based instrument can detect a microlensing event and capture the complete set. If a parallax measurement is needed, a ground based observatory may be alerted. However, replacing a large observatory with a smaller instrument which acquires the same resolution science will be a game-changer, causing significant reduction in costs and resources.

8.2   CS Detector Architecture

There are numerous options for implementing a CS based detector system as discussed in (Wakin *et al.* 2006), (Guzzi *et al.* 2019), (Zamkotsian, Lanzoni, & Tangen 2019). Spatial light modulators are used to implement measurement matrices. Previous work by (Xiao *et al.* 2012) show a CS implementation using coded aperture masks. In the literature from (Zhang *et al.* 2019), (Kuusela 2019) and (Huang *et al.* 2013), they implemented a single pixel camera using liquid crystal displays (LCD). Their work shows that lensless single pixel cameras can be implemented using LCD as their coded apertures.

In our analysis, we focus on using a DMD array for the CS projection. A CS architecture using a DMD array can have a frame rate of 32KHz with 2048x1080 pixels (Guzzi *et al.* 2019). In our simulations, we show the effectiveness with 0.25% of n. Let's assume $n = 2048 \times 1040$ pixels. We would need 550800 measurements. With the frame rate, this gives us 17.2 seconds to obtain one CS image, in addition to the needed exposure time. A typical microlensing event can last for 30 days. In (Mróz *et al.* 2020), they discovered the shortest time scale microlensing event, where t_e ≈ 41.5 minutes. Using Nyquist rate for this short time scale, we would expect to sample at least $\dfrac{t_e}{2}$ ≈ 20.75 seconds. Detection efficiency will not only depend on the

166

cadence of the system, but also on the flux magnification and Field-of-view (FOV). The larger the FOV, the greater the chances of detection of a microlensing event. A CS detector system would be beneficial for use on small satellites, where data storage and downlink can be limiting factors. Using a CS detector system on a constellation of satellites, we can detect microlensing parallax, as shown in Figure 8.1. In our simulations, we assume the number of satellites in the constellation to be $[0, n_{sat}]$, where the maximum number is $n_{sat} = 8$.
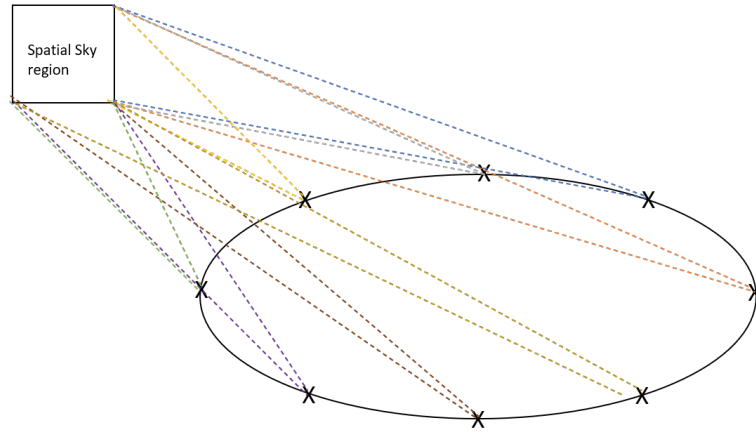
FIG. 8.1: A diagram of satellite constellations observing the same spatial region in order to capture a microlensing parallax of any microlensing events occuring the given field-of-view. X represents a satellite with a CS detector system.

A detector concept for placing a telescope on a Small Satellite can be based off of ASTERIA (Arcsecond Space Telescope Enabling Research in Astrophysics) (Krishnamurthy *et al.* 2021). ASTERIA is a 6U CubeSat with a telescope aperture of 6.7cm with a CMOS detector of 2592×2192 pixels. For a CS system our optics would include a telescope, micro-mirror arrays or any spatial light modulators, as well

as a photodiode to acquire the sum total of the reflected light from the micro-mirrors, as shown in Figure 8.2.
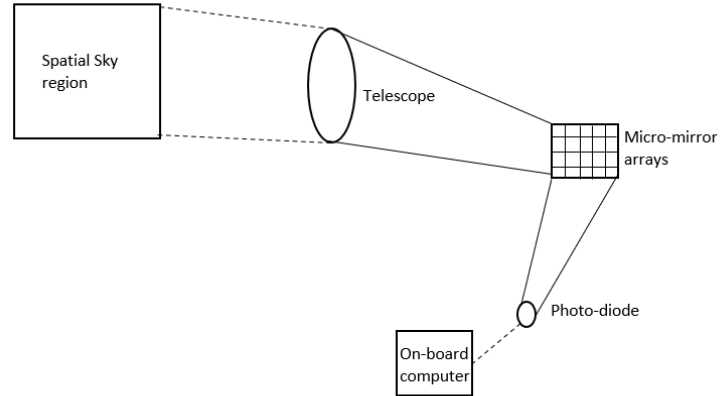
FIG. 8.2: A potential CS implementation of the detector system using a telescope to acquire the light from the spatial region, a set of micro-mirror arrays to reflect light using CS projection methods, and a photodiode to capture a single measurement of the total reflected light.

8.3 Detector Implementation

We briefly discuss implementation techniques to complete the architecture section. However, the implementation analysis is beyond the scope of this thesis and is discussed here only for complete understanding of the architectures and to validate feasibility of the path forward. One potential implementation of a Compressive Sensing based detector is a single pixel camera. A single pixel camera obtains a collective sum of photons, representing one compressive sensing measurement. The signal of interest is manipulated using a measurement matrix. Our previous work included developing a single pixel camera for capturing images, which used a digital micro-mirror

device (DMD) for the measurement matrix. Using this technique we can use random numbers of binary values, where one value represents the micro-mirror to be open and the other represents the micro-mirror to be close. Digital micro-mirrors are a type of spatial light omdulators which can be used to capture CS based images. Spatial light modulators are used to implement measurement matrices. Marcia discusses use of coded apertures and superimposing images to capture a video frame in (Marcia, Harmany, & Willett 2009). Uniformly redundant arrays have been used for aperture coding in optics (Fenimore & Cannon 1978). HxRG are Teledyne detectors which have been used for various space missions including OSIRIS-X, EUCLID, and JWST. They cover visible and infrared range, with the latest generation, H4RG, containing 4K by 4K pixels. They allow programmable windows to determine which areas of the detector need to be read out. Using such windows a CS measurement matrix projection scheme could be implemented.

8.4   Data Volume and Resources

In this section, we perform a comparison analysis of using traditional detectors versus CS based detectors.

1. Data volume storage

   Using a $n \times n$ image, with a 14-bit ADC resolution, we would expect the total data volume to be:

Traditional Detector	CS detector
14 bits $\times\ n \times n$	14 bits $\times\ m \times n$

   where m are the number of CS measurements and m is $<< n$. We would

make the assumption that the photodetector is not saturated with the ADC bit resolution needed to sample. Without data compression, we will need to transfer $14n^2$ bits/ FOV using a traditional detector. Using CS approach for 25% measurements, we can will need to transmit $14 \times 0.25 \times n \times n = 3.5n^2$ bits/ FOV.

2. Computational resources

   On-board computation will consist of programming the spatial modulator and storing the $m \times n$ size acquired data for each $n \times n$ spatial image. To compare this with a traditional detector system, we would require computational resources for compressing data on-board, in order to be accommodated in the data down-link bandwidth.

	Traditional Detector	CS detector
1	Data acquisition (ADC) interface	Data acquisition (ADC) interface
2	Data storage module	Data storage module
3	Data compression	Spatial modulation implementation
4	Data packetization and transmission	Data packetization and transmission

Table 8.1: FPGA modules comparison for traditional detector and CS based detector

In terms of on-board Field Programmable Gate Array (FPGA) resources for each of the modules listed in table 8.1, we would expect similar amount of logic gates, except for item 3. There are different methods for implementing data compression, including compression algorithms and pixel averaging (Anuradha & Bhuvaneswari 2016), (Dua, Kumar, & Singh 2020). For CS detectors, spatial modulation implementation will depend on the spatial modulator used. In

addition, we would require either storage or generation and transmission of the spatial modulation matrix (CS measurement matrix) on-board. The on-board storage needed for traditional detectors would be significantly higher than storage needed for CS architecture modules.

3. Optics

A traditional detector consists of a telescope and a detector, typically a CCD camera. In the case for CS, we would need a telescope, as well as lenses to focus the light on a spatial modulator device, such as DMD array, followed by a photodetector. However, lensless cameras for CS applications have been implemented (Zhang *et al.* 2019), (Kuusela 2019) and (Huang *et al.* 2013) and would need to be studied for a SmallSat type instrument. The optical path required to implement the detector system will be further studied in future work.

Chapter 9

CONCLUSIONS AND FUTURE WORK

In this chapter we will summarize the conclusions of each chapter as well as provide a detailed path forward for the completion of this thesis.

We performed an in-depth study on the effects of CS on transient photometric measurements, specifically light curves generated due to gravitational microlensing. In an ideal case, with only one source star pixel present in a differenced image, we show that we can obtain average error over all time samples with less than 0.0033% error using only 4% of Nyquist rate measurements. This shows CS can significantly reduce the number of data needed to be acquired, when the image is very sparse.

For detector read-outs with a very clean PSF of both observed and reference image, we can reconstruct the images within 2% accuracy using only 10% measurements. As the PSF of the reference and observed image are close in the width of the Airy shaped function, we note that the average % error decreases significantly.

Using CS techniques we give limitations on the sensitivity of detection of planetary perturbations given our CS parameters. Through our analysis for microlensing parameter fitting, we show that CS is most sensitive to F_s and F_b. Our work shows that we can reconstruct microlensing light curves using 25% of the required Nyquist rate measurements with error less than 1%. In terms of microlensing sensitivity, we

show that this error is within the bounds of 10% of θ_E for single microlensed events and within 10% of q and s for binary microlensed events.

In addition, we simulated microlensing parallax curves with different orbital phases using CS techniques. Our CS simulation results show error less than 0.5% over all time samples and average error less than 1.1% at t_0, while using 25% of traditional detector measurements for microlensing parallax light curves with a range of Φ from $\left[0, \dfrac{7\pi}{8}\right]$. Our results show that CS reconstruction should not cause any significant errors in detection of a microlensing parallax curve for any given orbital phase, Φ, value simulated. CS shows potential for implementation in a SmallSat constellation for detecting microlensing parallax events.

In this study, we show the effect of source noise as well as measurement noise. For source noise, if we use a measurement matrix with lower mutual coherence, we can attain better CS reconstruction in the presence of source noise for less sparse events. This result can also be generalized for any microlensing event with less sparse signals. For measurement noise added during data acquisition, we show that, when using a binomial measurement matrix, we can increase CS reconstruction accuracy by decreasing the expected value of the binomial distribution.

Our thesis work shows an optimistic path forward for applying compressive sensing for gravitational microlensing events. Our results show the error due to CS does not cause any significant errors in obtaining the science parameters of interest for a gravitational microlensing event. There is a trade-off between the number of measurements needed and the obtained CS reconstruction resolution error. Our work emphasizes that CS technology is especially essential for space flight instruments

using small satellites, where on-board resources are limited, which in turn hinders science resolution. CS provides a solution for retaining good science resolution, while reducing on-board resources. Our path forward would include architecting a design for implementation on a space flight instrument. This will include studying detectors suitable for building a CS based system on a small satellite.

APPENDIX A

9.1 Lensing Equations

In this section we derive the gravitational lensing equations.

9.1.1 Deflection angle due to a concentrated mass

Light deflects due to the gravitational effects of a lensing star (or planet). In this section, we show the derivation of the deflection angle of a light ray due to the gravitational effects of a point source with mass M.

In order to derive deflection angle, we can start with the force exerted on the photon due to the concentrated mass body. A pictorial representation is shown in Figure 9.1.
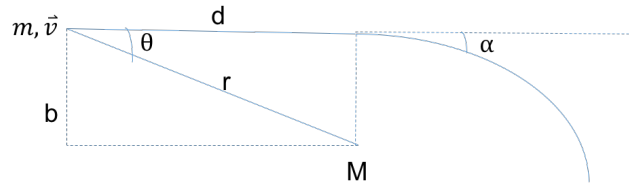
FIG. 9.1: Deflection of light due to the gravitational effects of a concentrated mass

To derive the force, we begin with Newton's second law of motion, equation 9.1, where m is the mass of the light photon and a is the acceleration of the photon.

$$F = ma \tag{9.1}$$

We need to derive the force perpendicular to the path of motion of the light

particle.

$$F_\perp = m\frac{dv_\perp}{dt} \tag{9.2}$$

$$v_\perp = \frac{1}{m}\int_{-\infty}^{\infty} F_\perp dt \tag{9.3}$$

$$\tag{9.4}$$

Since, $\sin\theta = \dfrac{b}{r}$,

$$F_\perp = F\sin\theta \tag{9.5}$$

$$= F\frac{b}{r} \tag{9.6}$$

Newton's law of gravity states,

$$F = \frac{GMm}{r^2} \tag{9.7}$$

$$F_\perp = \frac{GMmb}{r^3} \tag{9.8}$$

Einstein's equivalence principle states that the laws of nature are the same in uniform static graviational field and an accelerated frame of reference. Hence, equation 9.1 and equation 9.7 can be used equivalently. We can thus plus in equation 9.8 into equation 9.4. This gives us equation 9.9

$$v_\perp = \frac{1}{m}\int_{-\infty}^{\infty} \frac{GMmb}{r^3}dt \tag{9.9}$$

Due to the symmetry of $\sin\theta$, the limits of equation 9.9 can be rewritten as

$$v_\perp = \frac{2}{m} \int_0^\infty \frac{GMmb}{r^3} dt \tag{9.10}$$

$$v = \frac{ds}{dt} dt = \frac{ds}{v} \tag{9.11}$$

Plugging this into equation 9.12,

$$v_\perp = \frac{2}{m} \int_0^\infty \frac{GMmb}{r^3} \left(\frac{ds}{v}\right) \tag{9.12}$$

From Figure 9.1, $r = \sqrt{d^2 + b^2}$. Using this, equation 9.12 can be further simplified as follows:

$$v_\perp = \frac{2}{m} \int_0^\infty \frac{GMmb}{(d^2 + b^2)^{3/2}} \left(\frac{ds}{v}\right) \tag{9.13}$$

$$= \frac{2GM}{v} \int_0^\infty \frac{\frac{ds}{b}}{((d^2 + b^2) + 1)^{3/2}} \tag{9.14}$$

$$\tag{9.15}$$

Define, $s = \dfrac{d}{b}$

$$v_\perp = \frac{2GM}{vb} \int_0^\infty \frac{dx}{(x^2 + 1)^{3/2}} \tag{9.16}$$

$$\tag{9.17}$$

Solving the integral in equation 9.15,

$$v_\perp = \frac{2GM}{vb} \tag{9.18}$$

Deflection angle, α is related to $v_\perp$ and v by

$$\sin \alpha = \frac{v_\perp}{v} \tag{9.19}$$

$$\tag{9.20}$$

By small angle approximation, we get

$$\alpha = \frac{v_\perp}{v} \tag{9.21}$$

$$= \frac{2GM}{v^2b} \tag{9.22}$$

As this is a light corpuscle, v can be replaced with c. General relativity states that the deflection angle is twice as large due to the curvature in space-time dimension. Hence,

$$\alpha = \frac{4GM}{c^2b} \tag{9.23}$$

$$\tag{9.24}$$

9.1.2   Lensing Equations Derivation

To begin with, Figure 9.2 shows the geometry of a typical gravitational lensing system.
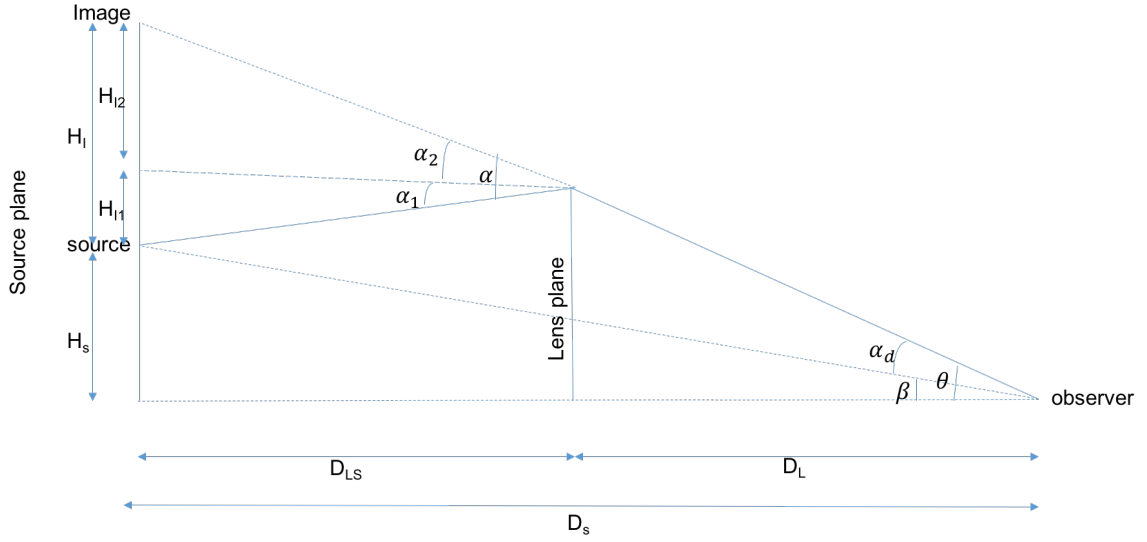
FIG. 9.2: Gravitational lensing system

Gravitational lensing happens due to a concentrated mass on the lensing plane deflecting the path of the light rays coming from the source to the observer. In this representation, trigonometry and small-angle approximations can be used to solve for the various angles and lengths. The angular distance from the observer to the source is given by equation 9.25

$$\beta = \frac{H_S}{D_S} \tag{9.25}$$

The angular distance from observer to the projected image due to gravitational lensing is given bye equation 9.26

$$\theta = \frac{(H_I + H_S)}{D_S} \tag{9.26}$$

In the geometric depiction of the triangle with α, consider a bisector bisecting through α into two angles, α_1 and α_2. Using the geometry and small-angle approxi-

179

mation, $\alpha_1 = \dfrac{H_{I1}}{D_{LS}}$ and $\alpha_2 = \dfrac{H_{I2}}{D_{LS}}$. Given $\alpha = \alpha_1 + \alpha_2$, $\alpha = \dfrac{H_{I1} + H_{I2}}{D_{LS}}$ and given $H_I = H_{I1} + H_{I2}$, equation 9.27 can be derived.

$$\alpha = \frac{H_I}{D_{LS}} \tag{9.27}$$

From equation 9.26, 9.25, and 9.27, we obtain:

$$\theta D_S = \alpha D_{LS} + \beta D_S \tag{9.28}$$

Reducing equation 9.28, the lensing equation can be derived, where $\alpha_d = \alpha \dfrac{D_{LS}}{D_S}$

$$\beta = \theta - \alpha_d(\theta) \tag{9.29}$$

Applying equation 9.24 to figure 9.2, we obtain:

$$\alpha(\theta) = \frac{4GM}{c^2 \theta D_L} \tag{9.30}$$

From equation 9.24, b is the distance from the the light ray to the concentrated mass, and thus, can be replaced with θD_L. Deflection angle, α, now becomes a function of θ. Hence α_d can now be rewritten as:

$$\alpha_d(\theta) = \frac{4GM}{c^2 \theta D_L} \frac{D_{LS}}{D_S} \tag{9.31}$$

$$= \frac{4GM\theta}{c^2 \theta^2 D_L} \frac{D_{LS}}{D_S} \tag{9.32}$$

Let us consider a point source multiple mass systems with positions not corresponding to the origin as assumed in the previous derivations.

$$\alpha_d(\theta) = \frac{4GD_{LS}}{c^2 D_L D_S} \sum_{i=0}^{N} m_i \frac{\theta - \theta_i}{|\theta - \theta_i|^2} \tag{9.33}$$

Einstein's ring radius, θ_E, is commonly used to normalize all angles.

$$\theta_E = \sqrt{\frac{4GMD_{LS}}{c^2 D_L D_S}} \tag{9.34}$$

Let $\mathbf{u} = (u_1, u_2)$ and $\mathbf{y} = (y_1, y_2)$, where $\mathbf{u} = \frac{\beta}{\theta_E}$ and $\mathbf{y} = \frac{\theta}{\theta_E}$. For complex coordinates of source and image positions, let $\zeta = u_1 + iu_2$, and $z = y_1 + iy_2$.

$$\zeta = z - \sum_{i}^{N} \frac{\frac{m_i}{M}}{\overline{z} - \overline{z_i}} \tag{9.35}$$

If $\epsilon_i = \frac{m_i}{M}$, then we obtain:

$$\zeta = z - \sum_{i}^{N} \frac{\epsilon_i}{\overline{z} - \overline{z_i}} \tag{9.36}$$

ζ corresponds to the position of the source, while z corresponds to the position of the image. By solving for z, we can find the image positions corresponding to that source image. This results in a complex polynomial of order $N^2 + 1$. This problem can be solved analytically for values of N < 2.

9.1.3   Amplification

Amplification can be measured by how much the source image is "stretched" on the image plane.

$$Amplification = \frac{ImageArea}{SourceArea}$$

We are transforming the coordinates from the source plane to the image plane to determine the amount of "stretching". The inverse of Jacobian, $\mathbf{J}$, is used to determine the amount of stretching. The Jacobian is the determinant of the Jacobian matrix, which is given by 9.1.3. The Jacobian matrix is given by the matrix below.

$$\frac{d(u_1, u_2)}{d(y_1, y_2)} = \begin{bmatrix} \dfrac{du_1}{dy_1} & \dfrac{du_2}{dy_1} \\ \dfrac{du_2}{dy_1} & \dfrac{du_2}{dy_2} \end{bmatrix}$$

Replacing $\mathbf{u}$ and $\mathbf{y}$ with ζ and z, and applying to 9.29, we get,

$$det\mathbf{J} = 1 - \frac{\partial \zeta}{\partial \bar{z}} \frac{\partial \bar{\zeta}}{\partial z}$$

(9.37)

$$\frac{\partial \zeta}{\partial \bar{z}} \frac{\partial \bar{\zeta}}{\partial z} = \left| \frac{\partial \zeta}{\partial \bar{z}} \right|^2$$

Hence, equation 9.1.3 can be simplifed to

$$1 - \left| \frac{\partial \zeta}{\partial \bar{z}} \right|^2$$

Amplification is given by 9.1.3 at each image position $z = z_j$.

$$A_j = \frac{1}{det\mathbf{J}} \tag{9.38}$$

Total amplification is given by $A = \sum_j |A|_j$ From 9.1.3, we can say that at source positions, z_j, when det $\mathbf{J} = 0$, amplification is infinite. when

$$\left| \frac{\partial \zeta}{\partial \bar{z}} \right|^2 = 1$$

In polar coordinates, the image positions are given by

$$\frac{\partial \zeta}{\partial \bar{z}} = e^{i\phi} \tag{9.39}$$

Here, ϕ can range from 0 to 2π. Critical curves are the positions on the image plane where the amplification goes to infinity. These critical curves can be mapped onto the source plane as caustic curves.

9.1.4   Single Lens Events

Single lens events can be analyzed during perfect and imperfect alignment. The lensing equation can be written as

$$\beta = \theta - \frac{\theta_E^2}{\theta} \tag{9.40}$$

For perfect alignment when $\beta = 0$, $\theta = \theta_E$. In this case, the image falls on Einstein's ring. For a single, lens equation, the image positions y as a function of source positions, u, can be derived from equation 9.28. Assuming point mass and using the origin for the position of the lens, 9.28 reduces to

$$u = y - \frac{1}{y} \tag{9.41}$$

In the case of imperfect alignment, When $\beta \neq 0$, the image positions, y, are the solutions to this equation 9.1.4.

183

$$uy = y^2 - 1 \tag{9.42}$$

$$y^2 - uy - 1 = 0 \tag{9.43}$$

Solving this quadratic equation for complex values, we get

$$y = \frac{u}{2} \pm \frac{\sqrt{u^2 + 4}}{2} \tag{9.44}$$

For single lens events, we can use real coordinates, x and y, to determine the amplification, which is solely the ratio of the image are to the source area.

$$A_\pm = \frac{y_\pm}{u} \frac{dy_\pm}{du} \tag{9.45}$$

For image, y_+, the magnification, A_+ is given by

$$\frac{dy_+}{du} = \frac{1}{2} + \frac{u}{2\sqrt{u^2 + 4}} \tag{9.46}$$

$$\frac{y_+}{u} = \frac{1}{2} + \frac{\sqrt{u^2 + 4}}{2u} \tag{9.47}$$

Thus,

$$A_+ = \frac{1}{2} + \left(\frac{1}{2}\right) \frac{u^2 + 2}{u\sqrt{u^2 + 4}} \tag{9.48}$$

Similarly for A_-,

$$\frac{dy_-}{du} = \frac{1}{2} - \frac{u}{2\sqrt{u^2 + 4}} \tag{9.49}$$

since this image is on the other side of the lens:

$$-\left(\frac{y_-}{u}\right) = -\left(\frac{1}{2} - \frac{\sqrt{u^2 + 4}}{2u}\right) \tag{9.50}$$

$$= -\frac{1}{2} + \frac{\sqrt{u^2 + 4}}{2u} \tag{9.51}$$

$$A_- = -\frac{1}{2} + \left(\frac{1}{2}\right)\frac{u^2 + 2}{u\sqrt{u^2 + 4}} \tag{9.52}$$

Total amplification is given by

$$A = |A_+| + |A_-| \tag{9.53}$$

$$= \frac{u^2 + 2}{u\sqrt{u^2 + 4}} \tag{9.54}$$

As the lens and source are in relative motion, the amplification at a given time can be parameterized using Shapiro time delay, making the source take a slightly longer path due to gravitational microlensing effects. For a uniform, straight line motion, the relative lens-source motion is

$$u(t) = \left[u_0^2 + \left(\frac{t - t_0}{t_E}\right)\right]^{\frac{1}{2}} \tag{9.55}$$

- u_0 is the minimum separation between lens and source in terms of θ_E.

- t_0 is the peak magnifcation time, which corresponds to when $u = u_0$.

- $t_E = \dfrac{\theta_E}{\mu_{rel}}$, is the Einstein ring radius crossing time, where μ_{rel} is the motion of the source in relation to the lens

Combining equation 9.1.4 with equation 9.1.4, we get

$$A(t) = \frac{u_0^2 + \dfrac{(t - t_0)^2}{t_E} + 2}{\left[u_0^2 + \dfrac{(t - t_0)^2}{t_E} \right]^{1/2} \left[u_0^2 + \dfrac{(t - t_0)^2}{t_E} + 4 \right]^{1/2}} \tag{9.56}$$

Magnification of single lens events depends primarily on u_0.

9.1.5 Binary Lens Equations

For binary lensing with both point-mass lenses, equation 9.1.2 can be written as

$$\Psi = z - \frac{m_1}{\bar{z} - \bar{z}_1} - \frac{m_2}{\bar{z} - \bar{z}_2} \tag{9.57}$$

Taking the conjugate of 9.57,

$$\bar{\Psi} = \bar{z} - \frac{m_1}{z - z_1} - \frac{m_2}{z - z_2} \tag{9.58}$$

Solving for $\bar{z}$,

$$\bar{z} = \bar{\Psi} + \frac{m_1}{z - z_1} + \frac{m_2}{z - z_2} \tag{9.59}$$

186

Replacing $\bar{z}$ with 9.59, equation 9.57 can be rewritten as

$$\Psi = z - \frac{m_1}{\bar{\Psi} + \dfrac{m_1}{z - z_1} + \dfrac{m_2}{z - z_2} - \bar{z}_1} - \frac{m_2}{\bar{\Psi} + \dfrac{m_1}{z - z_1} + \dfrac{m_2}{z - z_2} - \bar{z}_2}$$

$$\Psi = z - \frac{m_1}{\dfrac{\bar{\Psi}(z - z_1)(z - z_2) + m_1(z - z_2) - m_2(z - z_1) - \bar{z}_1(z - z_1)(z - z_2)}{(z - z_1)(z - z_2)}}$$
$$- \frac{m_2}{\dfrac{\bar{\Psi}(z - z_1)(z - z_2) + m_1(z - z_2) - m_2(z - z_1) - \bar{z}_2(z - z_1)(z - z_2)}{(z - z_1)(z - z_2)}}$$

$$\Psi = z - \frac{m_1(z - z_1)(z - z_2)}{\bar{\Psi}(z - z_1)(z - z_2) + m_1(z - z_2) - m_2(z - z_1) - \bar{z}_1(z - z_1)(z - z_2)}$$
$$- \frac{m_2(z - z_1)(z - z_2)}{\bar{\Psi}(z - z_1)(z - z_2) + m_1(z - z_2) - m_2(z - z_1) - \bar{z}_2(z - z_1)(z - z_2)}$$

The numerator can be written as:

$$z\bigg(\bar{\Psi}(z - z_1)(z - z_2) + m_1(z - z_2) - m_2(z - z_1) - \bar{z}_1(z - z_1)(z - z_2)\bigg)$$

$$\bigg(\bar{\Psi}(z - z_1)(z - z_2) + m_1(z - z_2) - m_2(z - z_1) - \bar{z}_2(z - z_1)(z - z_2)\bigg)$$

$$- \bigg(m_1(z - z_1)(z - z_2)\bigg)\bigg(\bar{\Psi}(z - z_1)(z - z_2) + m_1(z - z_2) - m_2(z - z_1) - \bar{z}_2(z - z_1)(z - z_2)\bigg)$$

$$- \bigg(m_2(z - z_1)(z - z_2)\bigg)$$

$$\bigg(\bar{\Psi}(z - z_1)(z - z_2) + m_1(z - z_2) - m_2(z - z_1) - \bar{z}_1(z - z_1)(z - z_2)\bigg)$$

and denominator can be written as

$$\left(\bar{\Psi}(z - z_1)(z - z_2) + m_1(z - z_2) - m_2(z - z_1) - \bar{z}_2(z - z_1)(z - z_2) \right)$$

$$\left(\bar{\Psi}(z - z_1)(z - z_2) + m_1(z - z_2) - m_2(z - z_1) - \bar{z}_1(z - z_1)(z - z_2) \right)$$

From the numerator, we get a 5th degree polynomial. Hence, there are either 5 or 3 solutions to 9.58. Since this is a 5th order polynomial, there are no analytical solutions, and hence, must be solved numerically.

Similar to single lens equations, once the solutions have been found, the magnification can be derived using equation 9.1.3 and equation 9.1.3. In our work, the light curves generated due to binary lensed microlensing events are given by the contour integration (Bozza 2010c) method as implemented in (Bozza *et al.* 2018).

APPENDIX B

9.2 Point Spread Function

Impulse response, $h(t)$, is the response of the a δ function through the system.

$$x = \int_{-\infty}^{\infty} x(\tau)\delta(\tau - t)d\tau$$

$$y(t) = H(x(t)) \tag{9.60}$$

$$= H(\int_{-\infty}^{\infty} x(\tau)\delta(\tau - t)d\tau) \tag{9.61}$$

$$\tag{9.62}$$

Due to linearity,

$$y(t) = \int_{-\infty}^{\infty} x(\tau)H(\delta(\tau - t))d\tau \tag{9.63}$$

$$= \int_{-\infty}^{\infty} x(\tau)h(\tau - t)d\tau \tag{9.64}$$

$$\tag{9.65}$$

h(t) can be the PSF obtained from TinyTim's tool or it could be a synthetically generated PSF. In order to obtain the output image, the point source image is convolved with the generated PSF.

APPENDIX C

9.3 Gravitational Microlensing Amplification Derivation for γ change in θ_E

We start with the equation shown in Appendix B (9.40). To obtain the solutions, we re-write equation 9.40 as equation 9.75

$$\theta^2 - \beta\theta - \theta_E^2 = 0 \tag{9.66}$$

Using the quadratic formulate to solve for the roots, we get the following equation:

$$\theta_{\pm} = \frac{1}{2}\left(\beta \pm \sqrt{\beta^2 + 4\theta_E^2}\right) \tag{9.67}$$

Amplification in terms of the angles is given by equation 9.68.

$$A_{\pm} = \left|\frac{\theta_{\pm}}{\beta}\frac{d\theta_{\pm}}{d\beta}\right| \tag{9.68}$$

First, we find each component required for solving for A.

$$\frac{\theta_{\pm}}{\beta} = \frac{1}{2} \pm \frac{\sqrt{\beta^2 + 4\theta_E^2}}{2\beta} \tag{9.69}$$

$$\frac{d\theta_{\pm}}{d\beta} = \frac{1}{2} \pm \frac{\beta}{2\sqrt{\beta^2 + 4\theta_E^2}} \tag{9.70}$$

$$\left|\frac{\theta_+}{\beta}\frac{d\theta_+}{d\beta}\right| = \left(\frac{1}{2} + \frac{\sqrt{\beta^2 + 4\theta_E^2}}{2\beta}\right)\left(\frac{1}{2} + \frac{\beta}{2\sqrt{\beta^2 + 4\theta_E^2}}\right)$$

$$= \frac{1}{4} + \frac{\beta}{4\sqrt{\beta^2 + 4\theta_E^2}} + \frac{\sqrt{\beta^2 + 4\theta_E^2}}{4\beta} + \frac{1}{4}$$

$$= \frac{1}{2} + \frac{\beta^2 + 2\theta_E^2}{2\beta\sqrt{\beta^2 + 4\theta_E^2}}$$

For the negative solution, we obtain:

$$\left|\frac{\theta_-}{\beta}\frac{d\theta_-}{d\beta}\right| = \left(\frac{1}{2} - \frac{\sqrt{\beta^2 + 4\theta_E^2}}{2\beta}\right)\left(\frac{1}{2} - \frac{\beta}{2\sqrt{\beta^2 + 4\theta_E^2}}\right)$$

$$= \frac{1}{4} - \frac{\beta}{4\sqrt{\beta^2 + 4\theta_E^2}} - \frac{\sqrt{\beta^2 + 4\theta_E^2}}{4\beta} + \frac{1}{4}$$

$$= \frac{1}{2} - \frac{\beta^2 + 2\theta_E^2}{2\beta\sqrt{\beta^2 + 4\theta_E^2}}$$

Due to negative parity, A_- becomes:

$$-\frac{1}{2} + \frac{\beta^2 + 2\theta_E^2}{2\beta\sqrt{4\beta^2 + 4\theta_E^2}} \tag{9.71}$$

Hence,

$$A = \frac{1}{2} + \frac{\beta^2 + 2\theta_E^2}{2\beta\sqrt{\beta^2 + 4\theta_E^2}} - \frac{1}{2} + \frac{\beta^2 + 2\theta_E^2}{2\beta\sqrt{\beta^2 + 4\theta_E^2}} \tag{9.72}$$

$$= \frac{\beta^2 + 2\theta_E^2}{\beta\sqrt{\beta^2 + 4\theta_E^2}} \tag{9.73}$$

To simplify, we multiply the result for A by $\dfrac{\theta_E^2}{\theta_E^2}$ to obtain

$$A = \frac{\left(\dfrac{\beta}{\theta_E}\right)^2 + 2}{\dfrac{\beta}{\theta_E^2}\sqrt{\beta^2 + 4\theta_E^2}}$$

$$= \frac{\left(\dfrac{\beta}{\theta_E}\right)^2 + 2}{\dfrac{\beta}{\theta_E}\sqrt{\left(\dfrac{\beta}{\theta_E}\right)^2 + 4}}$$

Let $u = \dfrac{\beta}{\theta_E}$ as consistent with the previous definition.

$$A = \frac{u^2 + 2}{u\sqrt{u^2 + 4}} \tag{9.74}$$

To calculate error sensitivity for γ change in θ_E, we can derive the following to obtain $\tilde{A}$.

We start with the lensing equation using $\gamma\theta_E$

$$\theta^2 - \beta\theta - \gamma^2\theta_E^2 = 0 \tag{9.75}$$

Using the quadratic formulate to solve for the roots, we get the following equation:

$$\theta_\pm = \frac{1}{2}\left(\beta \pm \sqrt{\beta^2 + 4\gamma^2\theta_E^2}\right) \tag{9.76}$$

Similarly, we obtain:

$$\frac{\theta_\pm}{\beta} = \frac{1}{2} \pm \frac{\sqrt{\beta^2 + 4\gamma^2\theta_E^2}}{2\beta} \tag{9.77}$$

$$\frac{d\theta_\pm}{d\beta} = \frac{1}{2} \pm \frac{\beta}{2\sqrt{\beta^2 + 4\gamma^2\theta_E^2}} \tag{9.78}$$

We do similar derivation to obtain A_+ and A_-:

$$\left|\frac{\theta_+}{\beta}\frac{d\theta_+}{d\beta}\right| = \left(\frac{1}{2} + \frac{\sqrt{\beta^2 + 4\gamma^2\theta_E^2}}{2\beta}\right)\left(\frac{1}{2} + \frac{\beta}{2\sqrt{\beta^2 + 4\gamma^2\theta_E^2}}\right)$$

$$= \frac{1}{4} + \frac{\beta}{4\sqrt{\beta^2 + 4\gamma^2\theta_E^2}} + \frac{\sqrt{\beta^2 + 4\gamma^2\theta_E^2}}{4\beta} + \frac{1}{4}$$

$$= \frac{1}{2} + \frac{\beta^2 + 2\gamma^2\theta_E^2}{2\beta\sqrt{\beta^2 + 4\gamma^2\theta_E^2}}$$

For the negative solution, we obtain:

$$\left|\frac{\theta_-}{\beta}\frac{d\theta_-}{d\beta}\right| = \left(\frac{1}{2} - \frac{\sqrt{\beta^2 + 4\gamma^2\theta_E^2}}{2\beta}\right)\left(\frac{1}{2} - \frac{\beta}{2\sqrt{\beta^2 + 4\gamma^2\theta_E^2}}\right)$$

$$= \frac{1}{4} - \frac{\beta}{4\sqrt{\beta^2 + 4\gamma^2\theta_E^2}} - \frac{\sqrt{\beta^2 + 4\ \gamma^2\theta_E^2}}{4\beta} + \frac{1}{4}$$

$$= \frac{1}{2} - \frac{\beta^2 + 2\gamma^2\theta_E^2}{2\beta\sqrt{\beta^2 + 4\gamma^2\theta_E^2}}$$

Due to negative parity, $\tilde{A}_-$ becomes:

$$-\frac{1}{2} + \frac{\beta^2 + 2\gamma^2\theta_E^2}{2\beta\sqrt{4\beta^2 + 4\gamma^2\theta_E^2}} \tag{9.79}$$

Summing both $\tilde{A}_+$ and $\tilde{A}_-$, we get $\tilde{A}$ as

$$\tilde{A} = \frac{1}{2} + \frac{\beta^2 + 2\gamma^2\theta_E^2}{2\beta\sqrt{\beta^2 + 4\gamma^2\theta_E^2}} - \frac{1}{2} + \frac{\beta^2 + 2\gamma^2\theta_E^2}{2\beta\sqrt{\beta^2 + 4\gamma^2\theta_E^2}}$$

$$= \frac{\beta^2 + 2\gamma^2\theta_E^2}{\beta\sqrt{\beta^2 + 4\gamma^2\theta_E^2}}$$

Here, we assume the same scaling factor to define u, in order to correctly compare the change in magnification for θ_E and $\gamma\theta_E$.

$$\tilde{A} = \frac{u^2 + 2\gamma^2}{u\sqrt{u^2 + 4\gamma^2}} \tag{9.80}$$

194

REFERENCES

[1] Alard, C., and Lupton, R. H. 1998. A method for optimal image subtraction. *The Astrophysical Journal* 503(1):325.

[2] Albrow, M.; Horne, K.; Bramich, D.; Fouqué, P.; Miller, V.; Beaulieu, J.-P.; Coutures, C.; Menzies, J.; Williams, A.; Batista, V.; et al. 2009. Difference imaging photometry of blended gravitational microlensing events with a numerical kernel. *Monthly Notices of the Royal Astronomical Society* 397(4):2099–2105.

[3] Anuradha, D., and Bhuvaneswari, S. 2016. A detailed review on the prominent compression methods used for reducing the data volume of big data. *Annals of Data Science* 3(1):47–62.

[4] Arias-Castro, E., and Eldar, Y. C. 2011. Noise folding in compressed sensing. *IEEE Signal Processing Letters* 18(8):478–481.

[5] Bachelet, E.; Hinse, T.; and Street, R. 2018. Measuring the microlensing parallax from various space observatories. *The Astronomical Journal* 155(5):191.

[6] Beckouche, S.; Starck, J.-L.; and Fadili, J. 2013. Astronomical image denoising using dictionary learning. *Astronomy & Astrophysics* 556:A132.

[7] Bertsekas, D. P., and Scientific, A. 2015. *Convex optimization algorithms*. Athena Scientific Belmont.

[8] Bobin, J.; Starck, J.-L.; and Ottensamer, R. 2008. Compressed sensing in astronomy. *IEEE Journal of Selected Topics in Signal Processing* 2(5):718–726.

[9] Boyd, S., and Vandenberghe, L. 2004. *Convex optimization.* Cambridge university press.

[10] Bozza, V.; Bachelet, E.; Bartolić, F.; Hoag, A. R.; Heintz, T. M.; and Hundertmark, M. 2018. VBBinaryLensing: a public package for microlensing light-curve computation. *Monthly Notices of the Royal Astronomical Society* 479(4):5157–5167.

[11] Bozza, V. 2010a. Microlensing with an advanced contour integration algorithm: Green's theorem to third order, error control, optimal sampling and limb darkening. *Monthly Notices of the Royal Astronomical Society* 408(4):2188–2200.

[12] Bozza, V. 2010b. Microlensing with an advanced contour integration algorithm: Green's theorem to third order, error control, optimal sampling and limb darkening. *Monthly Notices of the Royal Astronomical Society* 408(4):2188–2200.

[13] Bozza, V. 2010c. Microlensing with an advanced contour integration algorithm: Green's theorem to third order, error control, optimal sampling and limb darkening. *Monthly Notices of the Royal Astronomical Society* 408(4):2188–2200.

[14] Bramich, D. 2008. A new algorithm for difference image analysis. *Monthly Notices of the Royal Astronomical Society: Letters* 386(1):L77–L81.

[15] Cai, T. T., and Wang, L. 2011. Orthogonal matching pursuit for sparse signal recovery with noise. *IEEE Transactions on Information theory* 57(7):4680–4688.

[16] Candes, E., and Romberg, J. 2007. Sparsity and incoherence in compressive sampling. *Inverse problems* 23(3):969.

[17] Candès, E. J., and Wakin, M. B. 2008. An introduction to compressive sampling. *IEEE signal processing magazine* 25(2):21–30.

[18] Candes, E. J.; Eldar, Y. C.; Needell, D.; and Randall, P. 2011. Compressed sensing with coherent and redundant dictionaries. *Applied and Computational Harmonic Analysis* 31(1):59–73.

[19] Diamond, S., and Boyd, S. 2016. CVXPY: A Python-embedded modeling language for convex optimization. *Journal of Machine Learning Research* 17(83):1–5.

[20] Dua, Y.; Kumar, V.; and Singh, R. S. 2020. Comprehensive review of hyperspectral image compression algorithms. *Optical Engineering* 59(9):090902.

[21] Duarte-Carvajalino, J. M., and Sapiro, G. 2009. Learning to sense sparse signals: Simultaneous sensing matrix and sparsifying dictionary optimization. *IEEE Transactions on Image Processing* 18(7):1395–1408.

[22] Elad, M. 2007. Optimized projections for compressed sensing. *IEEE Transactions on Signal Processing* 55(12):5695–5702.

[23] Eldar, Y. C., and Kutyniok, G. 2012. *Compressed sensing: theory and applications.* Cambridge University Press.

[24] Fenimore, E. E., and Cannon, T. 1978. Coded aperture imaging with uniformly redundant arrays. *Applied optics* 17(3):337–347.

[25] Gould, A. 2000. A natural formalism for microlensing. *The Astrophysical Journal* 542(2):785.

[26] Gould, A. 2020. Rigorous" rich argument" in microlensing parallax. *arXiv preprint arXiv:2002.00947.*

[27] Gray, R. M., et al. 2006. Toeplitz and circulant matrices: A review. *Foundations and Trends® in Communications and Information Theory* 2(3):155–239.

[28] Guzzi, D.; Coluccia, G.; Labate, D.; Lastri, C.; Magli, E.; Nardino, V.; Palombi, L.; Pippi, I.; Coltuc, D.; Marchi, A. Z.; et al. 2019. Optical compressive sensing technologies for space applications: instrumental concepts and performance analysis. In *International Conference on Space Optics—ICSO 2018*, volume 11180, 111806B. International Society for Optics and Photonics.

[29] Hasinoff, S. W. 2014. Photon, poisson noise. In *Computer Vision.* Springer. 608–610.

[30] Huang, G.; Jiang, H.; Matthews, K.; and Wilford, P. 2013. Lensless imaging by compressive sensing. In *2013 IEEE International Conference on Image Processing*, 2101–2105. IEEE.

[31] Jauregui-Sánchez, Y.; Clemente, P.; Latorre-Carmona, P.; Tajahuerce, E.; and Lancis, J. 2018. Signal-to-noise ratio of single-pixel cameras based on photodiodes. *Applied Optics* 57(7):B67–B73.

[32] Korde-Patel, A.; Barry, R. K.; and Mohsenin, T. 2016a. Application of compressive sensing to gravitational microlensing data and implications for miniaturized space observatories. Technical report.

[33] Korde-Patel, A.; Barry, R. K.; and Mohsenin, T. 2016b. Application of compressive sensing to gravitational microlensing experiments. *Proceedings of the International Astronomical Union* 12(S325):67–70.

[34] Korde-Patel, A.; Barry, R. K.; and Mohsenin, T. 2020. Compressive sensing based data acquisition architecture for transient stellar events in crowded star fields. In *2020 IEEE International Instrumentation and Measurement Technology Conference (I2MTC)*, 1–6. IEEE.

[35] Korde-Patel, A.; Barry, R. K.; and Mohsenin, T. 2022. Application of compressive sensing for gravitational microlensing events. *Journal of Astronomical Telescopes, Instruments, and Systems* 8(1):018002.

[36] Krishnamurthy, A.; Knapp, M.; Günther, M. N.; Daylan, T.; Demory, B.-O.; Seager, S.; Bailey, V. P.; Smith, M. W.; Pong, C. M.; Hughes, K.; et al. 2021. Transit search for exoplanets around alpha centauri a and b with asteria. *The Astronomical Journal* 161(6):275.

[37] Kuusela, T. A. 2019. Single-pixel camera. *American Journal of Physics* 87(10):846–850.

[38] Lee, C.-H. 2017. Microlensing and its degeneracy breakers: Parallax, finite source, high-resolution imaging, and astrometry. *Universe* 3(3):53.

[39] Leonard, A.; Dupé, F.-X.; and Starck, J.-L. 2012. A compressed sensing approach to 3d weak lensing. *Astronomy & Astrophysics* 539:A85.

[40] Mairal, J.; Bach, F.; Ponce, J.; and Sapiro, G. 2009. Online dictionary learning for sparse coding. In *Proceedings of the 26th annual international conference on machine learning*, 689–696. ACM.

[41] Mansuripur, M. 1986. Distribution of light at and near the focus of high-numerical-aperture objectives. *JOSA A* 3(12):2086–2093.

[42] Marcia, R. F.; Harmany, Z. T.; and Willett, R. 2009. Compressive coded aperture imaging. In *Computational Imaging*, 72460.

[43] Mróz, P.; Poleski, R.; Gould, A.; Udalski, A.; Sumi, T.; Szymański, M. K.; Soszyński, I.; Pietrukowicz, P.; Kozłowski, S.; Skowron, J.; et al. 2020. A terrestrial-

mass rogue planet candidate detected in the shortest-timescale microlensing event. *The Astrophysical Journal Letters* 903(1):L11.

[44] Needell, D., and Vershynin, R. 2010. Signal recovery from incomplete and inaccurate measurements via regularized orthogonal matching pursuit. *IEEE Journal of selected topics in signal processing* 4(2):310–316.

[45] Needell, D.; Tropp, J.; and Vershynin, R. 2008. Greedy signal recovery review. In *Signals, Systems and Computers, 2008 42nd Asilomar Conference on*, 1048–1050. IEEE.

[46] Nguyen, T. L., and Shin, Y. 2013. Deterministic sensing matrices in compressive sensing: a survey. *The Scientific World Journal* 2013.

[47] O Donoghue, B.; Chu, E.; Parikh, N.; and Boyd, S. 2016. Conic optimization via operator splitting and homogeneous self-dual embedding. *Journal of Optimization Theory and Applications* 169(3):1042–1068.

[48] Pedregosa, F.; Varoquaux, G.; Gramfort, A.; Michel, V.; Thirion, B.; Grisel, O.; Blondel, M.; Prettenhofer, P.; Weiss, R.; Dubourg, V.; Vanderplas, J.; Passos, A.; Cournapeau, D.; Brucher, M.; Perrot, M.; and Duchesnay, E. 2011. Scikit-learn: Machine learning in Python. *Journal of Machine Learning Research* 12:2825–2830.

[49] Poleski, R., and Yee, J. C. 2019. Modeling microlensing events with mulensmodel. *Astronomy and computing* 26:35–49.

[50] Pope, G. 2009. *Compressive sensing: A summary of reconstruction algorithms*. Ph.D. Dissertation, ETH, Swiss Federal Institute of Technology Zurich, Department of Computer Science.

[51] Raffel, M.; Willert, C.; and Kompenhans, J. 1998. *Particle Image Velocimetry: A Practical Guide.* Engineering online library. Springer Berlin Heidelberg.

[52] Rebollo-Neira, L., and Bowley, J. 2013. Sparse representation of astronomical images. *JOSA A* 30(4):758–768.

[53] Seager. 2010. *Exoplanets.* The University of Arizona Press.

[54] Smith, M. C.; Mao, S.; and Paczyński, B. 2003. Acceleration and parallax effects in gravitational microlensing. *Monthly Notices of the Royal Astronomical Society* 339(4):925–936.

[55] Starck, J.-L.; Murtagh, F.; and Fadili, J. 2010a. *Sparse Image and Signal Processing: Wavelets, Curvelets, Morphological Diversity.* New York, NY, USA: Cambridge University Press.

[56] Starck, J.-L.; Murtagh, F.; and Fadili, J. M. 2010b. *Sparse image and signal processing: wavelets, curvelets, morphological diversity.* Cambridge university press.

[57] Tropp, J. A., and Gilbert, A. C. 2007. Signal recovery from random measurements via orthogonal matching pursuit. *IEEE Transactions on information theory* 53(12):4655–4666.

[58] Tropp, J. A. 2006. Random filters for compressive sampling. In *Information Sciences and Systems, 2006 40th Annual Conference on*, 216–217. IEEE.

[59] Tsapras, Y. 2018. Microlensing searches for exoplanets. *Geosciences* 8(10):365.

[60] Tschunko, H. F. 1974. Imaging performance of annular apertures. *Applied optics* 13(8):1820–1823.

[61] Wakin, M. B.; Laska, J. N.; Duarte, M. F.; Baron, D.; Sarvotham, S.; Takhar, D.; Kelly, K. F.; and Baraniuk, R. G. 2006. An architecture for compressive imaging. In *2006 international conference on image processing*, 1273–1276. IEEE.

[62] Wozniak, P. 2000. Difference image analysis of the ogle-ii bulge data. i. the method. *arXiv preprint astro-ph/0012143*.

[63] Xiao, L.-l.; Liu, K.; Han, D.-p.; and Liu, J.-y. 2012. A compressed sensing approach for enhancing infrared imaging resolution. *Optics & Laser Technology* 44(8):2354–2360.

[64] Yan, S., and Zhu, W. 2022. Measuring microlensing parallax via simultaneous observations from chinese space station telescope and roman telescope. *Research in Astronomy and Astrophysics* 22(2):025006.

[65] Yee, J. C. 2015. Lens masses and distances from microlens parallax and flux. *The Astrophysical Journal Letters* 814(1):L11.

[66] Zamkotsian, F.; Lanzoni, P.; and Tangen, K. 2019. Micromirror arrays for multi-object spectroscopy in space. In *International Conference on Space Optics—ICSO 2010*, volume 10565, 105655J. International Society for Optics and Photonics.

[67] Zhang, Z.; Su, Z.; Deng, Q.; Ye, J.; Peng, J.; and Zhong, J. 2019. Lensless single-pixel imaging by using lcd: application to small-size and multi-functional scanner. *Optics Express* 27(3):3731–3745.

[68] Zmuidzinas, J. 2003. Thermal noise and correlations in photon detection. *Applied optics* 42(25):4989–5008.